

UNIVERSITÉ DU QUÉBEC
INRS-ÉNERGIE, MATÉRIAUX ET TÉLÉCOMMUNICATIONS

Role of Atomic and Molecular Resonances in High-order Harmonic Generation from Laser-ablated Plumes

par
Muhammad Ashiq Fareed

Thèse présentée
pour l'obtention
du grade de PhilosophiæDoctor (Ph.D.)
en Sciences de l'Énergie et des Matériaux

Jury d'évaluation

Président du jury
et examinateur interne
Examinateur externes

Dr. François Légaré (INRS-EMT)

Dr. Thomas Brabec
University of Ottawa,
Ottawa, ON, Canada

Dr. Louis DiMauro
Ohio State University,
Columbus, OH, USA

Directeur de recherche

Dr. Tsuneyuki Ozaki (INRS-EMT)

May 2017

Abstract

High-order harmonic generation (HHG) process is explained with the so-called three-step model, where the valance electron is tunnel ionized, accelerates and photorecombines with the parent ion. In this model, it is assumed that electron's motion is not perturbed from the atomic and molecular resonances. However, several experiments have shown that in the HHG process, the electron quantum path is perturbed from the atomic and molecular resonances that change the high-order harmonic properties. As the natural resonances are of different types (*e.g.*, autoionizing, Giant resonance), their response for HHG is also observed differently. Several theoretical models have been proposed to explain the HHG mechanism from these resonances, but, in many cases of HHG from laser-ablated plumes (LAP), the information of the exact quantum path that the electron follows in the vicinity of these resonances was uncertain because of the lack of experimental proofs.

In this thesis, we use different elements containing different types of resonances and study their role in HHG. Tin, manganese and diatomic carbon are used as nonlinear media, as these elements contain strong resonance at different energies. The resonance of tin exists at energy ~ 26.35 eV, which appears from the autoionizing state (AIS) lying above the ionization threshold. Manganese contains an inner-shell giant resonance at energy ~ 51 eV that appears mainly from 3p-3d transitions. The resonance from diatomic carbon molecules could come from molecular dissociation, or involve an AIS or bound excited state.

In the first step, tin is used as a nonlinear medium for HHG to study electron interaction with the autoionizing $4d^{10}5s^25p$ state. This AIS perturbs the HHG process and increases the intensity of a single harmonic, called the resonant harmonic (RH), at energy ~ 26.35 eV. The RH intensity is observed to be about 20 times higher than the intensity of neighboring harmonics generated with the conventional three-step process, when driven with $0.8 \mu\text{m}$ lasers. The physics involved behind this RH generation was unknown. We investigate electron dynamics in the vicinity of AIS with tunable long-wavelength laser pulses and explain the exact mechanism involved in RH generation. Further, in past, it was assumed that during RH generation, the continuum electron is perturbed by the AIS only. However, we have found for the first time that when continuum

electron accelerates in the vicinity of the AIS, this electron is actually perturbed from three states; the AIS and its two dressed states of Sn^+ lying at frequency $\pm 2\Omega$ (where Ω is the frequency of the driving laser). The perturbation from the dressed AIS appears in the form of two satellite harmonics generated at frequency $\pm 2\Omega$ around the RH. The contribution of dressed AIS in satellite harmonic generation is further confirmed by solving the time-dependent Schrödinger equation (TDSE).

In the second step, manganese is used as a nonlinear medium for HHG. It is well known that from manganese two high-order harmonic series are generated. The first high-order harmonic series consists of harmonics up to 48 eV. After that, the second harmonic series (SHS) starts around 51 eV and high-order harmonics up to very high energy (~ 156 eV) are generated, with driving laser of 0.8 μm wavelength. The physical phenomenon of this SHS generation was circumstantial and lacked experimental proof. We used different experimental schemes to investigate the physical phenomenon involved and found that the inner-shell 3p-3d transitions of Mn^+ contribute to SHS generation. These results provide the routes to use inner-shell electrons for HHG and generate harmonics up to very high energy, with elements having low ionization potential (*e.g.*, $I_{\text{p}}_{\text{Mn}^+}=15.64$ eV) and also to study the multi-electron dynamics in atomic media, as at least two electrons (inner-shell and valance electron) contribute in HHG.

Finally, we study high-order harmonics from laser-ablated graphite plume. We observed that intensity of carbon harmonics is surprisingly high, and that these harmonics contain a strong redshift. However, the physics behind these properties was unknown. In graphite ablation, different types of carbon species can be ablated with the laser-matter interaction, and because of this, the active species responsible for HHG from laser-ablated graphite plume was unsure. Therefore, first we used time-resolved plasma emission spectroscopy to check the species contributing to HHG. From the spectroscopic results, it is revealed that laser-ablated graphite plume contains an abundance of diatomic carbon molecules. The contribution of these diatomic molecules to HHG is studied by comparing the harmonic spectra with their photoionization cross-section (PICS). A good agreement is found between the PICS of C_2 with the high-order harmonic spectrum. The spectroscopic results confirm that in laser-ablated graphite plume, high-order harmonics are generated from C_2 , and harmonic yield is high because of the large PICS of C_2 in the XUV region.

For the redshift, recent theoretical models predict that this redshift could appear because of two reasons. It could be either due to the involvement of the resonant excited states or molecular dissociation might be involved in HHG. We perform different experiments and investigate the exact physical reason involved behind this redshift.

Contents

List of Figures	vii
List of Tables	ix
List of Abbreviations	x
Acknowledgement	xii
Chapter 1.....	1
Introduction.....	1
1.1 Motivation	1
1.2 Frequency Conversion	2
1.3 Laser ablation	3
1.4 High-order Harmonic Generation	5
1.4.1 Ionization	7
1.4.2 Propagation in the Continuum	8
1.4.3 Recombination	9
1.5 Propagation Effects.....	11
1.5.1 Propogation Length	11
1.5.2 Phase Mismatch Factors.....	12
1.5.3 Photon Flux.....	13
1.6 Role of Different Resonances in HHG	15
Chapter 2	19
Experimental Setup	19
2.1 Ti:sapphire Laser System.....	19
2.1.1 Pulse Compression	20
2.2 Optical Parametric Amplifier.....	21
2.2.1 Amplification Stage of OPA	22
2.2.2 Hollow-core Fiber Compression.....	23
2.3 High-order Harmonic Generation Setup.....	24
Chapter 3	26
Resonant Harmonic Generation from the Dressed Autoionizing States of Sn+	26

3.1 Introduction.....	26
3.2 High-order Harmonic Generation from Sn⁺	28
3.2.1 Resonant-Harmonic Response within the Driving Laser Bandwidth	30
3.3 Theoretical Calculations.....	33
3.4 Coherence	36
Chapter 4	40
Role of Inner-shell 3p-3d Resonances in High-order Harmonic Generation.....	40
4.1 Introduction.....	40
4.2 High-order Harmonic Generation from Manganese.....	43
4.2.1 High-order Harmonic Cutoff Scaling with the Ionization Potential.....	44
4.2.2 Role of Inner-shell Resonances in HHG	45
4.3 Harmonic Generation with Long-wavelength Driving Lasers	50
Chapter 5	54
Carbon Molecules for Intense High-order Harmonics from Laser-ablated Graphite Plume.....	54
5.1 High-order Harmonics from Laser-ablated Graphite Plume.....	54
5.2 Time Resolved Laser-induced Breakdown Spectroscopy	56
5.3 Comparison between the High-order Harmonic Spectrum and the Photo-ionization Cross-section	61
Chapter 6	66
Properties of High-order Harmonics Generated from Diatomic Carbon Molecules.....	66
6.1 Introduction.....	66
6.2 High-order Harmonics from Laser-ablated Graphite Plumes Containing Different Carbon Compositions	67
6.3 Wavelength Scaling of High-order Harmonics	69
6.4 Tunable Redshift.....	70
6.4.1 Role of Resonant-excited States.....	72
6.4.2 Redshift due to Molecular Dissociation	75
Chapter 7	78
Conclusions and Applications	78

List of Figures

Figure 1.1: Plasma evolution at different time scales of laser pulse interaction	4
Figure 1.2: Schematic illustration of high-order harmonic generation	5
Figure 1.3: A typical high-order harmonic spectrum	6
Figure 1.4: Trace of different electron trajectories at different phases	9
Figure 1.5: Kinetic energy of electron at different phase angles	10
Figure 1.6: Harmonic flux variation as a function of medium length	15
Figure 2.1: Schematic diagram of the laser system installed at ALLS	20
Figure 2.2: Schematic diagram of the double grating laser compressor	21
Figure 2.3: Configuration of the HE-TOPAS OPA installed at ALLS	22
Figure 2.4: Schematic diagram of the setup used to increase the energy of the OPA	22
Figure 2.5: Schematic illustration of the setup used for few-cycle laser pulses	23
Figure 2.6: Schematic diagram of the experimental setup used for HHG	24
Figure 3.1: High-order harmonic spectra of Sn^+ at 1.84 μm driving laser	28
Figure 3.2: The RH response at different driving laser wavelengths	30
Figure 3.3: High-order harmonic spectra of Sn^+ with 1.75 μm	31
Figure 3.4: Energy diagram of the dressed autoionizing state of Sn^+	33
Figure 3.5: The spectrum calculated via 3D TDSE	34
Figure 3.6: The gabor transforms showing the temporal envelopes of the emission	35
Figure 3.7: Random spectra showing collimated harmonic emission	37
Figure 4.1: Experimental photoabsorption spectra of 3d metals (Sc to Cu)	43
Figure 4.2: High-order harmonic spectrum from manganese	43

Figure 4.3: High-order harmonic cutoff scaling with the ionization potential	45
Figure 4.4: Photoabsorption spectra of Mn and Mn ⁺	46
Figure 4.5: Comparison of the photoionization cross-section of manganese with the HHG spectrum	48
Figure 4.6: High-order harmonic spectra from manganese plume	50
Figure 5.1: HHG spectra generated from laser-ablated In ⁺ , Mg and C ₂ plumes	55
Figure 5.2: The spectrum of graphite plasma emission	57
Figure 5.3: Variation of the Swan bands for t_{sa} of 30 to 90 ns	58
Figure 5.4: Variation of high-order harmonic yield	59
Figure 5.5: Spectrally integrated images of carbon plasma plume expansion	60
Figure 5.6: Comparison of the high-order harmonic spectra	62
Figure 6.1: HHG spectra generated from three laser-ablated graphite plumes	67
Figure 6.2: XRD pattern and SEM image of Graphite-91 target	68
Figure 6.3: High-order harmonic spectra generated from carbon molecules	69
Figure 6.4: High-order harmonic spectrum of C ₂ at 1.5 μm wavelength	71
Figure 6.5: Intensity variation of the high-order harmonic spectra	73

List of Tables

Table 4.1: Spectroscopic parameters of Mn ⁺ such as the energy, oscillator strength, line width and the lifetime of the 3p ⁵ 3d ⁶ 4s and 3p ⁵ 3d ⁵ 4s ² resonances	47
Table 5.1: The parameters, σ_i (Mb) and β (asymmetry parameter) used for the calculation of photoionization cross-section	62
Table 6.1: Laser parameters used for high-order harmonic generation from diatomic carbon molecules	74

List of Abbreviations

ADK	Amonosov, Delone, and Krainov
AIS	Autoionizing state
ALLS	Advanced laser light source
BS	Beam splitter
DM	Dichroic mirror
EDS	Energy dispersive X-ray spectroscopy
HCF	Hollow-core fiber
HFA	Hartee-Fock Approximation
HHG	High-order harmonic generation
IR	Infrared
LAP	Laser-ablated plume
LIBS	Laser-induced breakdown spectroscopy
MCP	Multi-channel plate
MP	Main pulse
MWP	Macroscopic wave packet
OPA	Optical parametric amplifier
PICS	Photoionization cross-section
PP	Prepulse
QRS	Quantitative rescattering
RH	Resonant harmonic
SEM	Scanning electron microscope
SFA	Strong field approximation
SHS	Second harmonic series

TDSE	Time-dependent Schrödinger equation
THz	Terahertz
TR-LIBS	Time-resolved laser-induced breakdown spectroscopy
WLC	White light continuum
XRD	X-ray diffraction
XUV	Extreme ultra-violet

Acknowledgement

I would like to thank my supervisor Prof. Tsuneyuki Ozaki for his constant support and guideline to achieve all the tasks that I have completed throughout my doctoral work. His excellent guidance, motivation and immense knowledge always inspired me. What I like the most is that he always has an easy solution of all complicated things, either related to experiment or general stuff. This work would not have taken its present shape without his help.

I would also like to thank Dr. Sudipta Mondal who helped me during initial period of my PhD. Besides him, I am thankful to Prof. François Légaré, Dr. Bruno Schmidt and Dr. Nicolas Thiré for providing me intense infrared laser source that did a magical job for me and I succeeded to obtain these wonderful results. I am also thankful to Prof. Andre D. Bandrauk, Dr. Vasily Strelkov and Dr. Xue-bin Bian for providing me useful information regarding to my experimental data.

Finally, I am very thankful to Antoine Laramée and Philippe Lassonde. They were always ready to help me during the critical moments of my experiments. I am also thankful to all the technicians working in the machine shop for solving my problems.

Chapter 1

Introduction

1.1 Motivation

The revolution of photonics started in 1960, when Maiman developed the first laser. This laser was capable of producing laser pulses of pulse duration around millisecond (10^{-3} sec), but with very low peak power. This laser source opened the path to study the fast dynamics lying within the millisecond time scale. Many researchers in the world immediately got involved in this field and laser technology advanced very rapidly. Just after one year, the discovery of Q-switching and mode-locking techniques helped to improve the pulse duration and the laser intensity. In 1985, we were able to generate femtosecond laser pulses [1], with peak intensity $\sim 10^{15} \text{ Wcm}^{-2}$. This short pulse duration enabled us to study ultrafast phenomena occurring at femtosecond time scale, for example, the rotational and vibrational motion of molecules [2].

The current trend is to capture and control even faster motion of particles occurring at attosecond [1,3] or even zeptosecond [4] time scale, for example to capture and control the ultrafast motion of electrons inside atoms [5,6], molecules [7], and solids [8]. In atomic media, e.g., for the hydrogen atom, the natural time scale of an electron revolving around the nucleus is about 157 attoseconds in order to complete one cycle around the nucleus. Therefore, we need laser pulses shorter than 157 *as* to capture this electron on its natural time scale.

In ultrafast theory, the shortest possible laser pulse duration is estimated from the bandwidth of the generated pulses [5]. According to this theory, the spectral bandwidth of linearly chirped Gaussian pulse can be estimated from the relation,

$$\Delta\epsilon = \frac{4\ln 2}{\tau} \sqrt{1 + \left(\frac{b}{a}\right)^2} \hbar \quad (1.1)$$

Here τ and a ($a=2\ln 2 (I/\tau^2)$) are the pulse duration and pulse width, and b is the chirp of the pulse. For a transformed limited Gaussian pulse, this equation can be written as,

$$\tau[as].\Delta\varepsilon[eV] = 1825 \quad (1.2)$$

Eq. 1.2 shows that in order to generate laser pulses with pulse duration ~ 157 as , laser pulses with a bandwidth larger than 11.6 eV are required. Usually, femtosecond laser pulses are generated within the visible or infrared (IR) region of the electromagnetic spectrum. For example, the typical bandwidth of the Ti: sapphire laser is within the range of about 600 nm to 1000 nm [5]. As laser pulses of bandwidth around 11.6 eV or beyond are required in order to control the electron motion in hydrogen atom, it is hard to generate such a broad-bandwidth in the visible or infrared region. Therefore, laser pulses beyond the limit of the visible or IR region are required. This broad-bandwidth can be achieved by generating pulses in the soft X-ray or X-ray region. This can be achieved by several techniques, for example, with stimulated emission from laser produced plasmas [9] and free electron lasers [10]. However, the major problem of both techniques is that the time period of the generated X-ray pulses is in the picosecond or femtosecond range. Another possibility is to use nonlinear frequency conversion of ultrashort laser pulses in the XUV range. The details of this method are described below.

1.2 Frequency Conversion

In laser-matter interaction, when laser pulses interact with the medium, the response of the medium is usually categorized into three categories, known as linear, non-linear and extremely non-linear. The type of the response mainly depends on the laser intensity. The linear response occurs when low-intensity laser pulses interact with the medium and linear polarization (P) is induced by the material. This linear polarization can be expressed as,

$$P = \varepsilon_0\chi E \quad (1.3)$$

In this equation, ε_0 and χ represent the permittivity and susceptibility of the medium and E is the electric field of the driving laser. At laser intensities lower than 10^{12} Wcm^{-2} , this polarization shows a nonlinear response that is expressed as,

$$P = \sum_n \epsilon_0 \chi^{(n)} E^{(n)} \quad (1.4)$$

In nonlinear laser-matter interaction, the higher orders of susceptibility, such as χ^2 and χ^3 are induced. The initial orders of this susceptibility are perturbed when laser pulses at intensity $< 10^{12} \text{ Wcm}^{-2}$ interact with the medium.

When driving laser intensity increases from 10^{12} Wcm^{-2} , higher orders of nonlinearities are induced. One such process is known as HHG. High-order harmonics are generated at laser intensities ranging from 10^{13} Wcm^{-2} to 10^{15} Wcm^{-2} . In HHG, the fundamental laser light, with a certain frequency (ω_L), is converted into a series of odd harmonics. These odd harmonics have a wavelength range where the intensities are similar (details given later), and thus this method is highly suitable to generate broad-bandwidth laser pulses required for attosecond or zeptosecond pulse generation. Complete details of HHG are given in section 1.3.

High-order harmonics are generated with different types of material, such as using gaseous medium [11], LAP [12] and solid surfaces [13]. We are using LAP for HHG. The advantages of this technique for HHG are; **(i)** Variety of materials can be used as the nonlinear medium, **(ii)** High conversion efficiency ($\sim 10^{-4}$), and **(iii)** Generation of intense, narrow bandwidth XUV harmonics (resonant harmonic; details are given in chapter 3) [14,15].

To study HHG from LAP, it is important to understand the plasma properties to better understand the dynamics of HHG. In the following section, the properties of the LAP, such as its ablation and evolution with time are described.

1.3 Laser ablation

In HHG from low-density plasma plumes, the nonlinear medium is ablated from a solid target. This is achieved by focusing laser pulses of $\sim 10^{10} \text{ Wcm}^{-2}$ intensity on solid targets. High-order harmonic properties, such as efficiency and divergence strictly depend on the plasma properties. Plasma plumes with moderate density and volume are desirable to generate high-order harmonics with good specifications [16,17]. Generally, plasma plumes are ablated with laser pulses with nanosecond to femtosecond pulse duration [18]. The heat dissipation and energy absorption of the solid target is different for these lasers, and plasma plumes with different properties are

ablated with different lasers. When nanosecond laser pulses are used for ablation, the sample heating, ionization and vaporization all occur during the laser pulse interaction because of large laser pulse duration. However, in the case of picosecond or femtosecond laser pulses, the ablation starts after the pulse heating and complete energy is used for the ablation only [19]. The time evolution of plasma with nanosecond and femtosecond laser pulses is shown in the following figure.

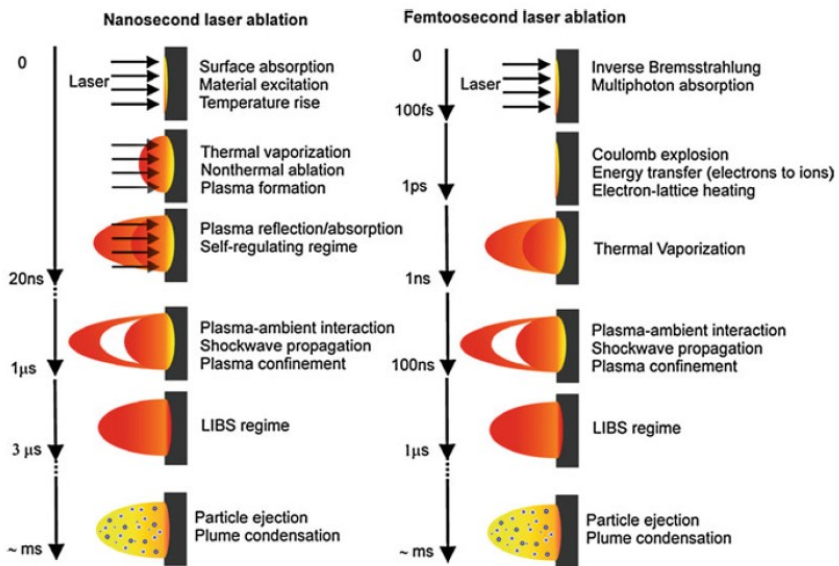


Figure 1.1: Plasma evolution at different time scales of laser pulse interaction [19].

We use picosecond laser pulses for the plume ablation and then laser-induced breakdown spectroscopy is usually used to study the plasma properties. First, the spatial and temporal properties of this plume are optimized for the efficient HHG and then the atomic/molecular density is controlled with the heating pulse intensity (details given below). It is observed that efficient harmonics are generated with laser intensity $\sim 10^{10} \text{ Wcm}^{-2}$ that is used to ablate few micrograms of material per pulse [20]. This low ablation of material from the target surface provides an opportunity to generate stable harmonics up to few minutes at same target position [21].

Plasma plumes with relatively low free carrier density are required for efficient HHG [16]. This is because high free carrier density will increase phase mismatch, thus reducing the high-order

harmonic efficiency. From **Fig. 1.1**, we can see that when heating pulse interact with the solid target, thermal evaporation starts after few nanoseconds of interaction, and then the plasma plume expands in the perpendicular direction. The lifetime of this plasma plume is usually from microseconds to milliseconds (**Fig. 1.1**). For harmonic generation, plasma is expanded for 30 ns to 100 ns and then an orthogonal laser pulse is introduced for HHG. This period is maintained to expand the plasma and cool it down so that the number of free carriers are reduced in the plasma.

The second important parameter for efficient HHG is the medium density. Efficient harmonics are generated when the density of the medium becomes moderate during plasma plume expansion. This parameter is usually controlled by changing the heating pulse intensity. For the laser parameters used for efficient HHG, the medium density is estimated to be from 10^{16} to 10^{17} cm^{-3} [22].

1.4 High-order Harmonic Generation

HHG is known as an extremely high nonlinear process that occurs when intense laser field ($\geq 10^{13} \text{ Wcm}^{-2}$) interact with an atom or molecule. This HHG process is usually explained with the quasi-classical three-step model [23]. According to this model, when ultrafast laser pulses interact with an electron, this electron is tunnel ionized from an atom. In the second step, this electron accelerates in the continuum by the applied laser field and then finally recombines with the parent ion by emitting a high-energy photon. The schematic illustration of this three-step process is shown in **Fig. 1.2** below.

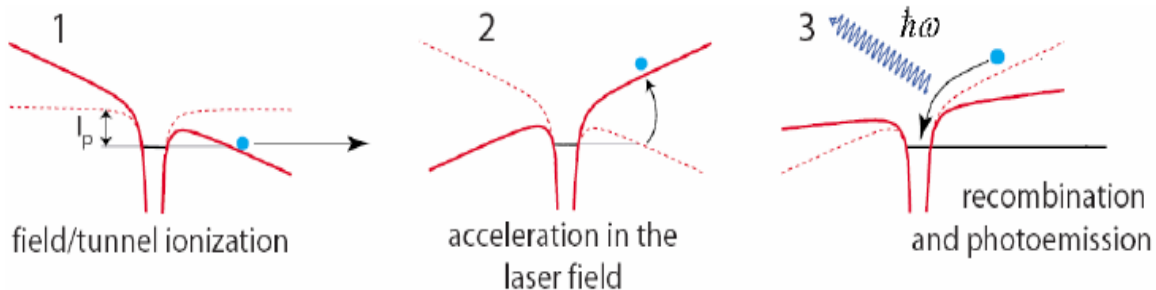


Figure 1.2: Schematic illustration of high-order harmonic generation. In the three-step model, an electron is ionized (via tunneling) from an atom (step 1). Then, this electron is accelerated by the applied laser field (step 2) and finally recombines to the atom by emitting an XUV photon (step 3) [24].

Several numerical methods based on the three-step process are used to model the high-order harmonic spectrum. The most popular methods are TDSE, strong field approximation (SFA), and quantitative rescattering (QRS) theory [23,25,26]. The typical high-order harmonic spectrum calculated with SFA model is given in the following figure.

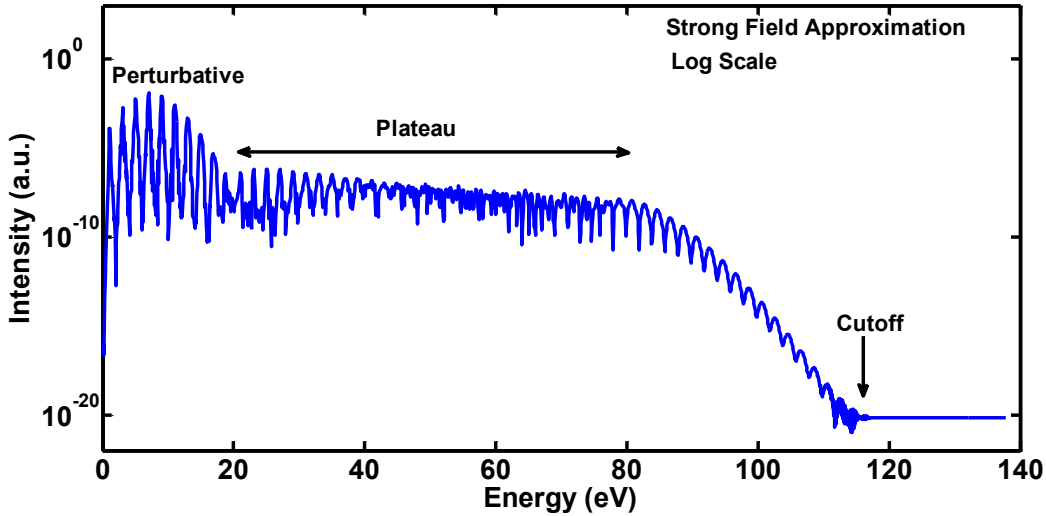


Figure 1.3: A typical high-order harmonic spectrum calculated with the strong field approximation.

This high-order harmonic spectrum is usually divided into three parts, known as the perturbative, plateau, and cutoff. The perturbative part of the harmonic spectrum consists of low-order harmonics, which are usually generated with low intensities ($\leq 10^{12} \text{ Wcm}^{-2}$). The plateau of the harmonic spectrum contains a series of harmonics with similar peak intensity. Finally, the cutoff of the harmonic spectrum represents the highest kinetic energy that the recombining electron gains during the three-step process. This cutoff energy is the sum of the maximum ponderomotive energy that electron gains in the continuum during acceleration and the ionization potential of the element (details are given in the next section).

Only odd harmonics of the fundamental frequency are generated because of the inversion symmetry in the conversion medium. However, this inversion symmetry can be broken by introducing an additional second harmonic laser pulse. Further details of these three steps, such as ionization, acceleration and recombination are described below.

1.4.1 Ionization

The first step of the three-step model is ionization. When high-intensity laser pulses interact with an atom, the atomic potential can be written as,

$$V = -\frac{e^2}{4\pi\epsilon_0 r} + e\vec{E}\vec{r} \quad (1.5)$$

At certain laser intensity, when the electric field strength becomes comparable to the interatomic field strength, the tunneling process occurs and the electron is ionized. The schematic diagram of this tunneling process is shown in **Fig. 1.2**.

High-order harmonic efficiency depends on the number of atoms participating in HHG. In 1965, Keldysh [27] introduces a model to calculate the ionization rate from a specific element. The rate equation that he introduced is given as,

$$W_keld = A\omega \frac{\sqrt{3\pi}}{4} \left(\frac{E_{ion}}{\hbar}\right) \left(\frac{E_{ion}}{\hbar\omega}\gamma\right)^{\frac{1}{2}} \exp\left\{-\frac{4}{3}\frac{E_{ion}}{\hbar\omega}\gamma\right\} \quad (1.6)$$

Here E_{ion} and ω are the ionization potential and frequency of the driving laser. The parameter γ is known as the Keldysh parameter and is given as,

$$\gamma = \left(\frac{E_{ion}}{2U_p}\right)^{\frac{1}{2}}$$

$$U_p = e^2 E^2 / (4m_e \omega_L^2)$$

Here, U_p is the ponderomotive energy of electron and γ is used to differentiate the process of tunneling ionization and the multi-photon ionization. The tunneling process occurs when $\gamma \ll 1$ [27].

In 1986, Amonosov, Delone, and Krainov [28] improved the accuracy of this method and introduced the ADK model. The ionization rate equation of this model is given as,

$$W_ADK = \omega_p |C_{n^*}|^2 \left(\frac{4\omega_p}{\omega_t}\right)^{2n^*-1} \exp\left\{-\frac{4\omega_p}{3\omega_t}\right\} \quad (1.7)$$

The parameters, $|C_{n^*}|^2$, ω_p , ω_t and n^* are given below,

$$\omega_p = \frac{E_{ion}}{\hbar}; \quad \omega_p = \frac{e|E(t)|}{\sqrt{2m_e E_{ion}}}; \quad n^* = Z \left(\frac{E_{ion}^H}{E_{ion}} \right)^{1/2}$$

$$|C_{n^*}|^2 = \frac{2^{2n^*}}{n^* \Gamma(n^* + 1) \Gamma(n^*)}$$

$$\Gamma(z) = \int_0^\infty e^{-t} t^{z-1} dt; \equiv \text{gamma function } (\Gamma(n) = (n-1)!)$$

Here Z is the net resulting charge of the atom and E_{ion}^H represents the ionization potential of the hydrogen atom.

Both models given in **Eq. 1.6** and **1.7** show that the ionization rate from the medium increases exponentially with the driving laser frequency and is wavelength independent. The ADK model gives more accurate values of ionization rate and is commonly used for the ionization rate calculation to model the high-order harmonic spectrum [23,25]. However, ADK model only holds when gamma goes to zero. Perelomov *et al.* introduced PPT model that include the Coulomb interaction at larger internuclear distances [29,30].

1.4.2 Propagation in the Continuum

The second step of the three-step model is the acceleration of the tunnel-ionized electron [23]. We use the classical picture to understand the motion of this electron in the driving laser field. When the driving laser field interacts with the electron, the velocity and the position of this free electron at an arbitrary phase ϕ can be written as,

$$v(\phi) = \dot{x}(\phi) = v_{osc}(\sin\phi - \sin\phi_0) \quad (1.8)$$

$$x(\phi) = \frac{v_{osc}}{\omega} \{ \cos\phi_0 - \cos\phi + (\phi_0 - \phi) \sin\phi_0 \} \quad (1.9)$$

Here $\phi = wt$, $\phi_0 = wt_i$ and v_{osc} is given as

$$v_{osc} = \frac{eE_0}{m\omega}; \quad \equiv \text{Maximum oscillation velocity of the electron}$$

If we consider an electron located at position $x=0$ and appear in the continuum at time zero with zero initial velocity, the trace of the electron trajectories at different phases can be calculated as,

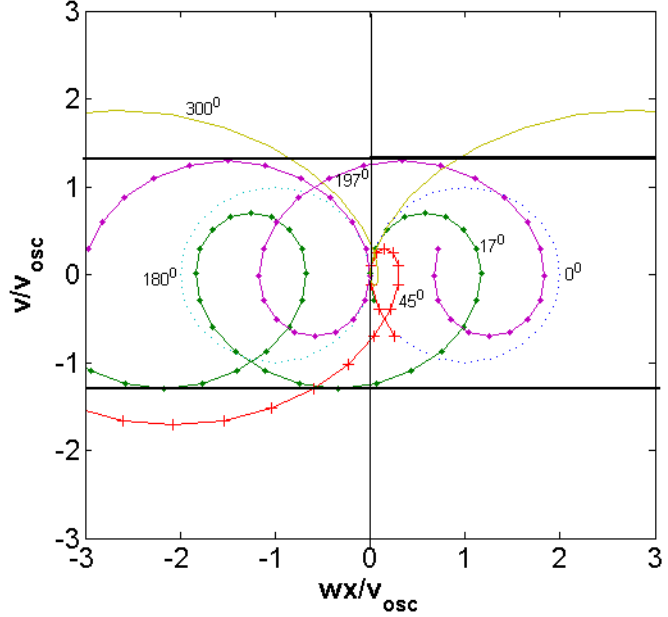


Figure 1.4: Trace of different electron trajectories at different phases in the position-velocity plane.

Fig. 1.4 shows the different trajectories of an electron at different phases of applied electric field. This figure shows that a few electron trajectories return back at position $x=0$ and electrons from these trajectories only participate in HHG. Most of the electrons are produced at unfavorable phases and never return back. This figure also indicates that the maximum kinetic energy is obtained at 17° , which gives the cutoff of the high-order harmonics. The kinetic energy that electron can experience in the continuum is given below,

$$U_p = e^2 E^2 / (4m_2 \omega_L^2) = 9.33 \times 10^{-14} I_L [\text{Wcm}^{-2}] \lambda_L^2 [\mu\text{m}] \quad (1.10)$$

1.4.3 Recombination

The final step of the three-step model is the recombination. When electron recombines with the parent ion, a high energy photon is emitted. The maximum energy of this electron can be estimated with the equation,

$$E_{max} = I_p + K_{max} \quad (1.11)$$

Here I_p is the ionization potential of the element and K_{max} represents the maximum kinetic energy that a recombining electron can experience in the continuum. The trend of the kinetic energy can be obtained by solving **Eq. 1.9** numerically at $x=0$, and calculating the kinetic energy for various laser field phases. The variation of kinetic energy at different phase angles is shown in **Fig. 1.5**. This figure shows that the maximum kinetic energy obtained at 17^0 is $3.17U_p$.

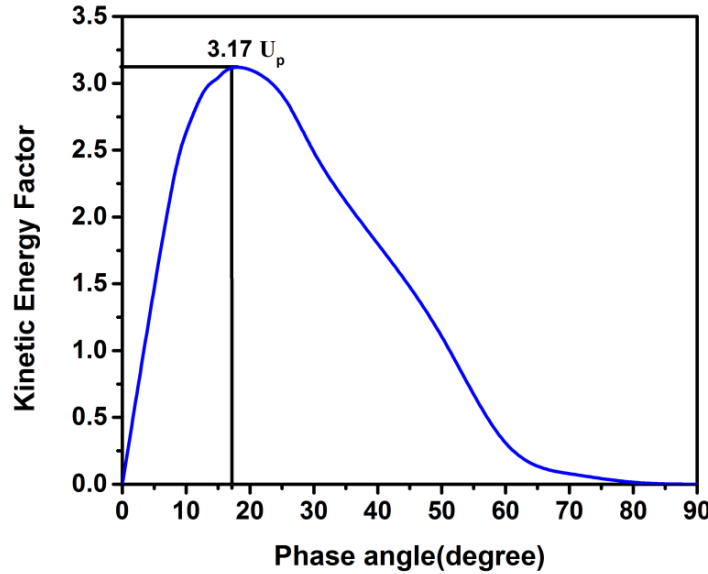


Figure 1.5: Kinetic energy of electron at different phase angles.

Therefore, **Eq. 1.11** can be written as,

$$E_{max} = I_p + 3.17U_p \quad (1.12)$$

This relation is known as the cutoff rule of the three-step model and gives the approximate value of harmonic cutoff that can be observed from a specific element.

This equation shows that the harmonic cutoff can be increased by increasing the ponderomotive energy of the electron that depends on the driving laser intensity and wavelength (**Eq. 1.10**). However, it is observed that the saturation intensity limits the high-order harmonic cutoff [1]. This is because the high laser intensities increase the number of free carriers in the plasma that introduce a phase mismatch in HHG. In the following section, we will see how this phase mismatch affects the HHG process.

1.5 Propagation Effects

The three-step model can only predict high-order harmonic cutoff, but this model cannot estimate the harmonic yield. High-order harmonic spectrum is generated due to the coherent sum of the radiated fields produced from a large number of atoms/molecules in the generation medium. Therefore, propagation effects are important to be considered to obtain the high-order harmonic strength [31]. In this section, we will study the properties of driving field when it propagates through the nonlinear medium for HHG and its limits for high-order harmonic efficiency.

1.5.1 Propagation Length

For coherent harmonic build up, the generated harmonics should propagate parallel to the driving laser field. When laser pulse propagates in the medium, there is a certain length over which both the laser field and the harmonic wave can remain in phase [32]. This length is called the coherence length and is given as,

$$L_{coh} = \frac{\pi}{\Delta k} \quad (1.13)$$

Here $\Delta k = qk_0 - k_q$ is the phase mismatch that depends on the wave vector of both driving laser field (k_0) and harmonic order (k_q ; q represent the harmonic order). This equation shows that coherence length depends on the phase matching conditions. Optimal phase matching is achieved when $\Delta k = 0$ condition is achieved. Usually, phase matching is improved by choosing appropriate laser conditions and geometry of the medium. Complete details of the parameters involved in phase matching are described in the next section.

The other limitation of this propagation effect is the limited absorption length of the medium. When harmonic photon energy exceeds the binding energies of the medium, the generated harmonics can be absorbed by the medium itself [32]. This absorption length is given as

$$L_{abs} = \frac{1}{\rho\sigma} \quad (1.14)$$

Here ρ is the medium density and σ represents the photoionization cross-section. This parameter limits the cutoff of the harmonics [32].

The phase mismatch factors that can occur during laser propagation in the medium are described in the following section.

1.5.2 Phase Mismatch Factors

In LAP, phase mismatch mainly comes from four factors [33] that are known as atomic dispersion (Δk_{atm}), plasma dispersion (Δk_{plasma}), Gouy phase shift (Δk_{Gouy}) and dynamical phase shift (Δk_{Dyn}).

Therefore, phase mismatch due to these factors can be written as,

$$\Delta k = \Delta k_{atm} + \Delta k_{plasma} + \Delta k_{Gouy} + \Delta k_{Dyn} \quad (1.15)$$

The phase mismatch due to the atomic dispersion is given as,

$$\Delta k_{atm} = \frac{q\omega_L}{c} (n_{Laser} - n_{Harmonic}) \quad (1.16)$$

Here, n_{Laser} and $n_{Harmonic}$ represents the refractive indices of the driving laser and q^{th} harmonic order. The refractive index for the driving laser field at frequency ω_L can be written as,

$$n_0(\omega) = 1 + (1 - \eta)N\pi c^3 \sum_k \frac{g_{2k}}{g_{1k}} \frac{A_k}{\omega_k^2(\omega_k^2 - \omega_L^2)}$$

Here, η , N , g_{2k}/g_{1k} , ω_k and A_k are the ionization fraction ($N_{electron}/N_{atomic}$; usually considered from 5 to 10%), atomic density, ratio of the statistical weights, transition frequencies and Einstein's coefficient respectively. The value of $n_{Harmonic}$ is usually assumed as one.

Using this relation of refractive index, Eq. 1.16 becomes,

$$\Delta k_{atm} = -(1 - \eta)N\pi c^2 q\omega_L \sum_k \frac{g_{2k}}{g_{1k}} \frac{A_k}{\omega_k^2 - \omega_L^2} \quad (1.17)$$

The phase mismatch due to the plasma dispersion is written as,

$$\Delta k_{plasma} = \frac{\eta Ne^2 q}{c\omega_L \epsilon_0 m} \quad (1.18)$$

This phase mismatch is introduced due to the production of free carriers in the medium. The third phase mismatch factor that could appear during HHG is the Gouy phase shift. When laser pulses are focused in the medium, the Gouy phase shift is introduced because of the phase change. For the Gaussian laser beam, Gouy phase at position z can be written as,

$$\varphi_{Gouy}(z) = \tan^{-1} \frac{d + L_{med} - z}{z_R}$$

Here d is the distance of the focus from the target position and $z_R (\pi\omega_L^2/\lambda)$ represents the Rayleigh length. The phase mismatch in the q^{th} harmonic, occurring due to Gouy phase can be written as,

$$\Delta k_{Gouy}(z) = \frac{q-1}{L_{med}} \left[\tan^{-1} \frac{d+L_{med}}{z_R} - \tan^{-1} \frac{d}{z_R} \right] \quad (1.19)$$

The final phase mismatch that could appear in HHG from LAP is the dynamical phase shift that comes from the laser intensity. This phase mismatch at focusing distance d is written as,

$$\Delta k_{Dyn} = -\frac{1}{L_{med}} C_{1,2} [I_L(d + L_{med}) - I_L(d)] \quad (1.20)$$

Here I_L represents the laser intensity and $C_{1,2}$ is a constant that depend on the trajectory of the harmonic (long and short trajectories) that electron follows for HHG (**Fig. 1.4**).

1.5.3 Photon Flux

For this limited propagation length and phase mismatch (discussed above), the photon flux that can build up during HHG can be estimated [32]. For a certain medium length (L_{med}), the field amplitude of the harmonic radiation can be written as,

$$E_q = \int_0^{L_{med}} N_0 d(q\omega_L) dz \quad (1.21)$$

Here $d(q\omega_L)$ represents the dipole moment for the q^{th} harmonic. This dipole moment can be calculated with the SFA model. Including phase mismatch factors and reabsorption limit (α) the **Eq. 1.21** can be written as,

$$E_q = \int_0^{L_{med}} N_0 d(q\omega_L) \exp(i\Delta kz) \exp[-\alpha(L_{med} - z)] dz \quad (1.22)$$

Here Δkz and $\exp[-\alpha(L_{med} - z)]$ are the phase mismatch and reabsorption terms of harmonics at position z . As we know from **Eq. 1.13** and **Eq. 1.14** that

$$L_{coh} = \frac{\pi}{\Delta k} \quad \text{and} \quad L_{abs} = \frac{1}{\rho\sigma} = \frac{1}{2\alpha}$$

Using these two equations and total phase mismatch Δk , given in **Eq. 1.15**, the equation of field amplitude becomes,

$$E_q = \int_0^{L_{med}} N_0 d(q\omega_L) \exp\left(\frac{i\pi z}{L_{coh}}\right) \exp\left[-\frac{L_{med} - z}{2L_{abs}}\right] dz$$

Or

$$\begin{aligned} E_q &= N_0 d(q\omega_L) \exp\left[-\frac{L_{med}}{2L_{abs}}\right] \int_0^{L_{med}} dz \exp\left(\frac{i\pi}{L_{coh}} + \frac{1}{2L_{abs}}\right) z \\ E_q &= N_0 d(q\omega_L) \exp\left[-\frac{L_{med}}{2L_{abs}}\right] \frac{\exp\left(\frac{i\pi}{L_{coh}} + \frac{1}{2L_{abs}}\right) L_{med} - 1}{\left(\frac{i\pi}{L_{coh}} + \frac{1}{2L_{abs}}\right)} \end{aligned} \quad (1.23)$$

For q^{th} harmonic, number of photons are given as,

$$N_q \propto |E_q|^2$$

Or

$$N_q \propto N_0^2 |d(q\omega_L)|^2 \frac{4(L_{abs}L_{coh})^2}{L_{coh}^2 + (2\pi L_{abs})^2} \times \left[1 + \exp\left(-\frac{L_{med}}{L_{abs}}\right) - 2\cos\left(-\frac{\pi L_{med}}{L_{coh}}\right) \exp\left(-\frac{L_{med}}{2L_{abs}}\right) \right] \quad (1.24)$$

This equation gives us the photon flux that can be produced from a specific element.

The evaluation of N_q as a function of medium length was calculated by Constant *et al.* [32], which is presented in the following figure. From this evaluation, Constant *et al.* found that the overall optimizing conditions in the absorption medium are,

$$L_{med} > 3L_{abs} \text{ and } L_{coh} > 5L_{abs}$$

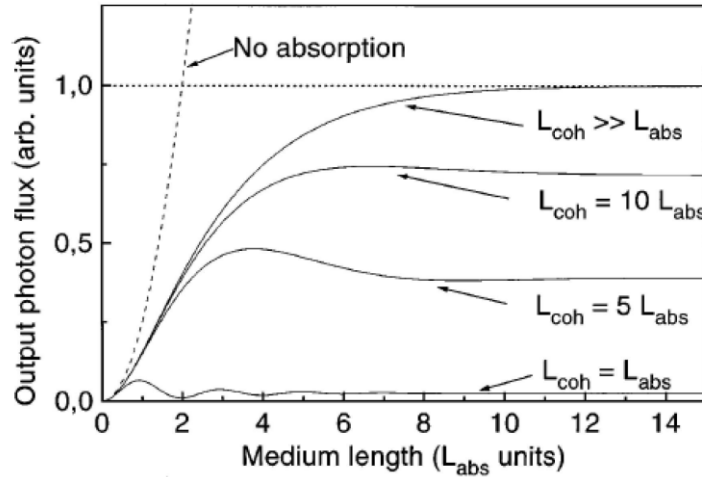


Figure 1.6: Harmonic flux variation as a function of medium length [32].

1.6 Role of Different Resonances in HHG

In the three-step model, it is assumed that only ground state electron participates in HHG, and the contribution from the inner shells and resonant-excited states are ignored. Contrary to that, several experimental results have been shown that the HHG process is perturbed from the atomic and molecular resonances. In laser-ablation technique of HHG, this was first observed by Ganeev *et al.* [34] in the harmonics from In^+ . He observed a dramatic change in a single harmonic intensity and attributed this change due to the involvement of AIS in HHG, lying above the ionization threshold. Later, the perturbation in HHG process has been observed in several media appearing from inner-shell [35], below ionization-threshold [36,37] and above ionization-threshold resonances [38].

The HHG mechanism from these resonances is different than the three-step process. In this thesis we have used different elements containing different types of resonances and studied that how these resonances contribute in HHG and the exact mechanism involved in resonant HHG is investigated.

References

- [1] P. Corkum and F. Krausz, Nat. Phys. **3**, 381 (2007).
- [2] A. H. Zewail, J. Phys. Chem. A **104**, 5660 (2000).
- [3] T. Popmintchev, M.-C. Chen, D. Popmintchev, P. Arpin, S. Brown, S. Alisauskas, G. Andriukaitis, T. Balciunas, O. D. Mücke, A. Pugzlys, A. Baltuska, B. Shim, S. E. Schrauth, A. Gaeta, C. Hernández-García, L. Plaja, A. Becker, A. Jaron-Becker, M. M. Murnane, and H. C. Kapteyn, Science **336**, 1287 (2012).
- [4] C. Hernandez-Garcia, J. A. Perez-Hernandez, T. Popmintchev, M. M. Murnane, H. C. Kapteyn, A. Jaron-Becker, A. Becker, and L. Plaja, Phys. Rev. Lett. **111**, 033002 (2013).
- [5] Z. Chang, Fundamentals of Attosecond Optics (CRC Press, 2011).
- [6] T. Popmintchev, M.-C. Chen, P. Arpin, M. M. Murnane, and H. C. Kapteyn, Nat. Photonics **4**, 822 (2010).
- [7] G. Sansone, F. Kelkensberg, J. F. Pérez-Torres, F. Morales, M. F. Kling, W. Siu, O. Ghafur, P. Johnsson, M. Swoboda, E. Benedetti, F. Ferrari, F. Lépine, J. L. Sanz-Vicario, S. Zherebtsov, I. Znakovskaya, A. L'Huillier, M. Y. Ivanov, M. Nisoli, F. Martín, and M. J. J. Vrakking, Nature **465**, 763 (2010).
- [8] M. Schultze, K. Ramasesha, C. D. Pemmaraju, S. A. Sato, D. Whitmore, A. Gandman, J. S. Prell, L. J. Borja, D. Prendergast, K. Yabana, D. M. Neumark, and S. R. Leone, Science **346**, 1348 (2014).
- [9] M. M. Murnane, H. C. Kapteyn, M. D. Rosen, and R. W. Falcone, Science **251**, 531 (1991).
- [10] V. Ayvazyan, N. Baboi, J. Bähr Eur. Phys. J. D **37**, 297 (2006).
- [11] S. Kazamias, D. Douillet, F. Weihe, C. Valentin, A. Rousse, S. Sebban, G. Grillon, F. Augé, D. Hulin, and P. Balcou, Phys. Rev. Lett. **90**, 193901 (2003).
- [12] R. A. Ganeev, J. Phys. B At. Mol. Opt. Phys. **40**, R213 (2007).
- [13] P. Norreys, M. Zepf, S. Moustaisis, A. Fews, J. Zhang, P. Lee, M. Bakarezos, C. Danson, A. Dyson, P. Gibbon, P. Loukakos, D. Neely, F. Walsh, J. Wark, and A. Dangor, Phys. Rev. Lett. **76**, 1832 (1996).
- [14] R. A. Ganeev, T. Witting, C. Hutchison, F. Frank, P. V. Redkin, W. A. Okell, D. Y. Lei, T. Roschuk, S. A. Maier, J. P. Marangos, and J. W. G. Tisch, Phys. Rev. A **85**, 015807 (2012).
- [15] R. A. Ganeev, High-Order Harmonic Generation in Laser Plasma Plumes (World Scientific, 2013).
- [16] M. A. Fareed, S. Mondal, Y. Pertot, and T. Ozaki, J. Phys. B. **49**, 035604 (2016).
- [17] R. A. Ganeev, L. B. Elouga Bom, and T. Ozaki, Phys. Plasmas **18**, 083101 (2011).
- [18] A. W. Mizolek, V. Palleschi, and I. Schechter, Laser-Induced Breakdown Spectroscopy (LIBS): Fundamentals and Applications (Cambridge, 2006).
- [19] Sergio Musazzi, Umberto Perini (eds), Laser -Induced Breakdown Spectroscopy: Theory and Applications (Springer Series in Optical Sciences, 2014).
- [20] S. Rajendiran, A. K. Rossall, A. Gibson, and E. Wagenaars, Surf. Coatings Technol. **260**, 417 (2014).
- [21] L. B. Elouga Bom, Y. Pertot, V. R. Bhardwaj, and T. Ozaki, Opt. Express **19**, 3077 (2011).
- [22] R. A. Ganeev, L. B. Elouga Bom, T. Ozaki, and P. V. Redkin, J. Opt. Soc. Am. B **24**, 2770 (2007).
- [23] P. Corkum, Phys. Rev. Lett. **71**, 1994 (1993).
- [24] C. Winterfeldt, C. Spielmann, and G. Gerber, Rev. Mod. Phys. **80**, 117 (2008).
- [25] M. Lewenstein, P. Balcou, M. Y. Ivanov, A. L'Huillier, and P. B. Corkum, Phys. Rev. A **49**, 2117 (1994).
- [26] A. T. Le, R. R. Lucchese, S. Tonzani, T. Morishita, and C. D. Lin, Phys. Rev. A. **80**, 013401 (2009).
- [27] L. V. Keldysh, J. Exp. Theor. Phys. **20**, 1307 (1965).
- [28] M. V. Ammosov, N. B. Delone, and V. P. Krainov, Sov. Phys. JETP **64**, 1191 (1986).
- [29] A. M. Perelemov V. S. Popov and M. V. Terent'ev, Soviet Phys. JETP, **23** 924 (1966).
- [30] A. M. Perelemov and V. S. Popov Soviet Phys.JETP, **25** 336 (1967).
- [31] C. Winterfeldt, C. Spielmann, and G. Gerber, Rev. Mod. Phys. **80**, 117 (2008).
- [32] E. Constant, D. Garzella, P. Breger, E. Mével, C. Dorrer, C. Le Blanc, F. Salin, and P. Agostini, Phys. Rev. Lett. **82**, 1668 (1999).

- [33] H. Singhal, V. Arora, B. Rao, P. Naik, U. Chakravarty, R. Khan, and P. Gupta, Phys. Rev. A **79**, 023807 (2009).
- [34] R. A. Ganeev, M. Suzuki, M. Baba, H. Kuroda, and T. Ozaki, Opt. Lett. **31**, 1699 (2006).
- [35] A. D. Shiner, B. E. Schmidt, C. Trallero-Herrero, H. J. Wörner, S. Patchkovskii, P. B. Corkum, J.-C. Kieffer, F. Légaré, and D. M. Villeneuve, Nat. Phys. **7**, 464 (2011).
- [36] X.-B. Bian and A. D. Bandrauk, Phys. Rev. A **83**, 041403 (2011).
- [37] M. Gaarde and K. Schafer, Phys. Rev. A **64**, 013820 (2001).
- [38] T. Ozaki, R. A. Ganeev, M. Suzuki, and H. Kuroda, High-order Harmonic Generation from Low-Density Plasma, in (In Tech, 2010).

Chapter 2

Experimental Setup

Experiments are performed at the Advanced Laser Light Source (ALLS, Varennes (QC) Canada). This is a high power multi-beam Ti:sapphire based laser system, providing laser pulses in a wide range of electromagnetic spectrum, ranging from terahertz (THz) to Soft X-rays [1–5]. At this laser facility, two laser lines are used for the HHG from LAP. These two laser lines are capable of producing laser pulses of energies 350 mJ and 80 mJ, at repetition rates of 10 Hz and 100 Hz, respectively. The central wavelength of these laser pulses is $\sim 0.8 \mu\text{m}$ and pulse duration before compression is $\sim 210 \text{ ps}$. These laser pulses are then seeded to different optical systems to generate laser pulses at variable wavelengths ranging from $0.266 \mu\text{m}$ to $2.3 \mu\text{m}$. Finally, these laser pulses with different specifications are used to generate high-order harmonics. On the high-order harmonic setup, XUV pulses of multi- μJ energy are produced. Complete details of the XUV beam line are given below.

2.1 Ti:sapphire Laser System

The schematic diagram of the Ti:sapphire laser system developed at ALLS is shown in **Fig. 2.1**. In this laser system, the femtosecond oscillator produces laser pulses of energy $\sim 4 \text{ nJ}$ at wavelength $\sim 795 \text{ nm}$. These laser pulses are then seeded to different optical systems for energy amplification. After amplification, this laser system produces laser pulses of energy $\sim 25 \text{ mJ}$, at 100 Hz repetition rate. These laser pulses are then divided into two parts, to generate laser pulses at two different repetition rates of 10 Hz and 100 Hz. One part of the 10 Hz line is passed through two amplification stages and laser pulses of energy $\sim 410 \text{ mJ}$ are produced. The second part of the beam (at 100 Hz repetition rate) is passed through different amplification stages (shown in **Fig. 2.1**) and laser pulses of energy $\sim 80 \text{ mJ}$ are produced.

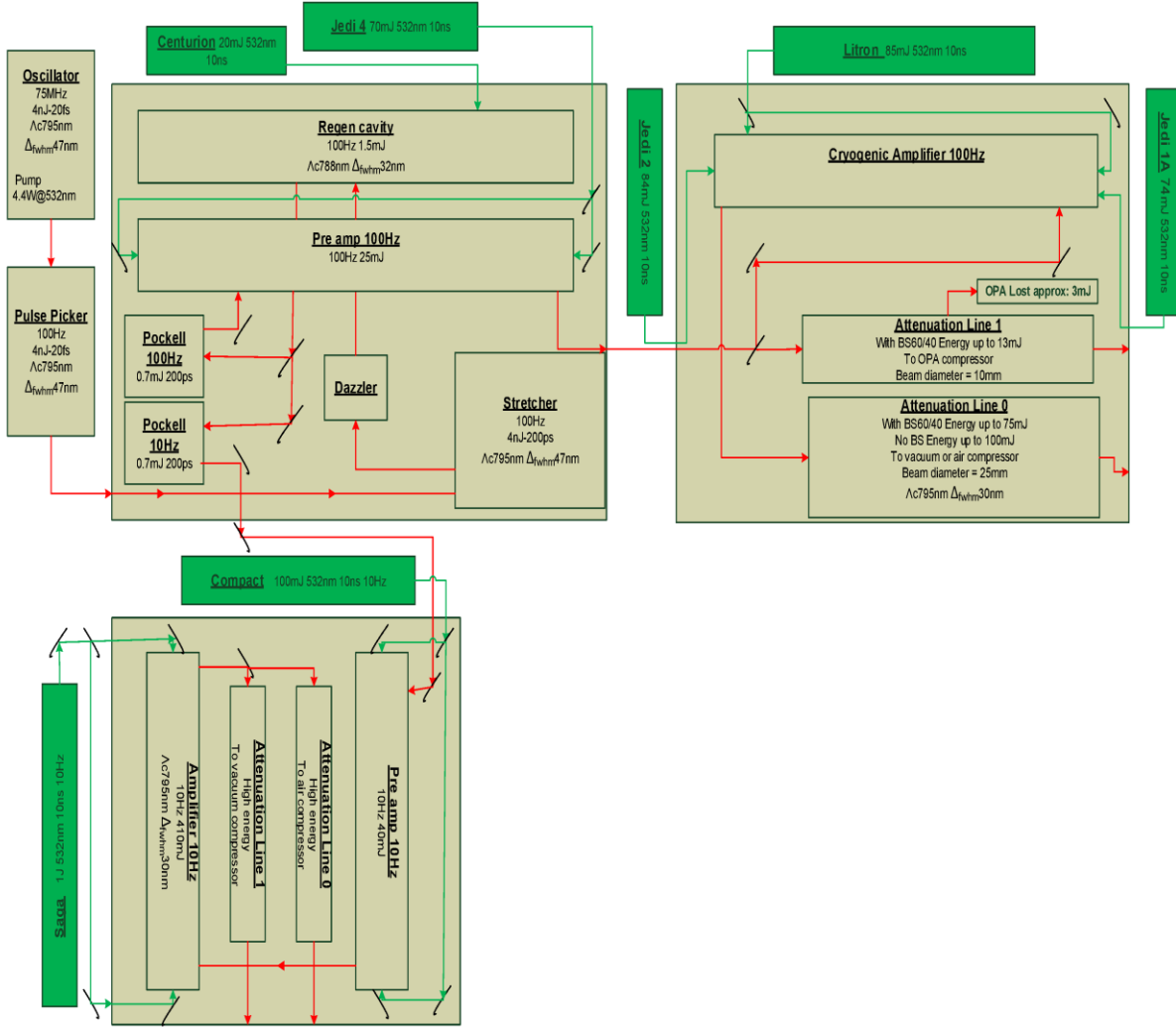


Figure 2.1: Schematic diagram of the laser system installed at ALLS. This is a Ti:sapphire based laser system that produces laser pulses of energy 410 mJ and 80 mJ at two different repetition rates of 10 Hz and 100 Hz respectively. The pulse duration of these laser pulses is \sim 210 ps and wavelength is centered at \sim 800 nm.

2.1.1 Pulse Compression

The pulse duration of this laser system (described above) is \sim 210 ps. These laser pulses have bandwidth around 30 nm at FWHM. To achieve high intensity, these laser pulses are further compressed with double grating compression technique. The schematic diagram of this double grating compression is shown in **Fig. 2.2**. In this technique, the path of the long-wavelength and short-wavelength components is varied to compress these pulses. With this compression technique, laser pulses as short as 40 fs are produced at both lines of ALLS laser system.

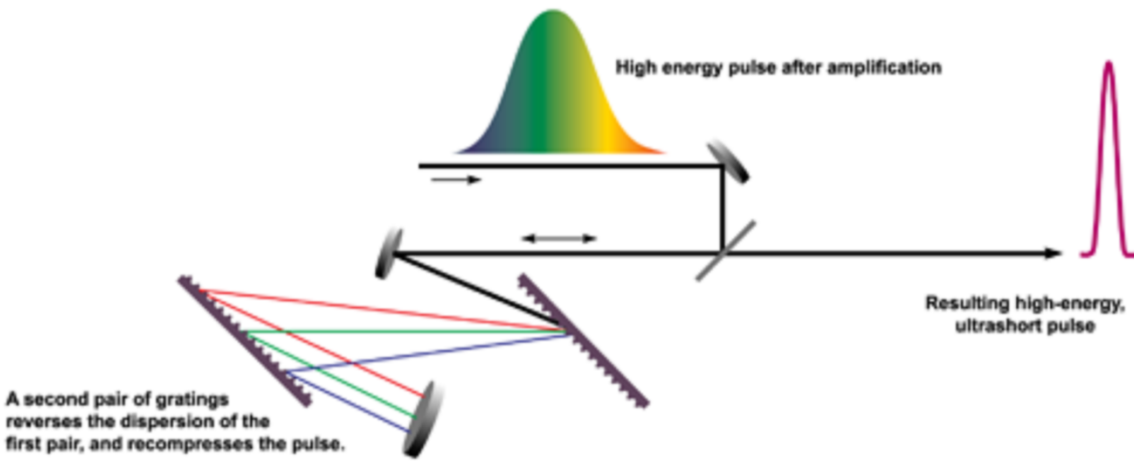


Figure 2.2: Schematic diagram of the double grating laser compressor.

2.2 Optical Parametric Amplifier

The optical parametric amplifier (OPA) installed at ALLS is the HE-TOPAS model from Light Conversion Ltd. This is a white light OPA based on the two-stage parametric amplifier. The schematic diagram of HE-TOPAS is given in **Fig. 2.3**. The configuration of this OPA comprises several subunits consisting of beam delivery, white light continuum (WLC) generation, and amplification stages. All subunits are arranged in a single unit and are computer controlled, which allow the precise control of the optics for efficient light conversion.

Compressed laser pulses of energy ~ 5 mJ and pulse duration ~ 40 fs are seeded to this OPA. A small part of this beam (about $1\text{-}3 \mu\text{J}$) is used to produce WLC in a sapphire plate. After that, this WLC along with a small fraction of the beam with energy $\sim 30\text{-}50 \mu\text{J}$ are focused into the pre-amplifier crystal. Non-collinear geometry is used to temporally overlap these pulses, as this configuration is suitable to separate the amplified signal beam. This signal beam is further amplified with a second amplification stage.

Wavelength tuning is achieved in the pre-amplifier stage by changing the delay of the white-light pulse with respect to the pump pulse and adjusting the crystal angle for optimal phase-matching. After that second amplification stage is optimized to amplify the power of these pulses.

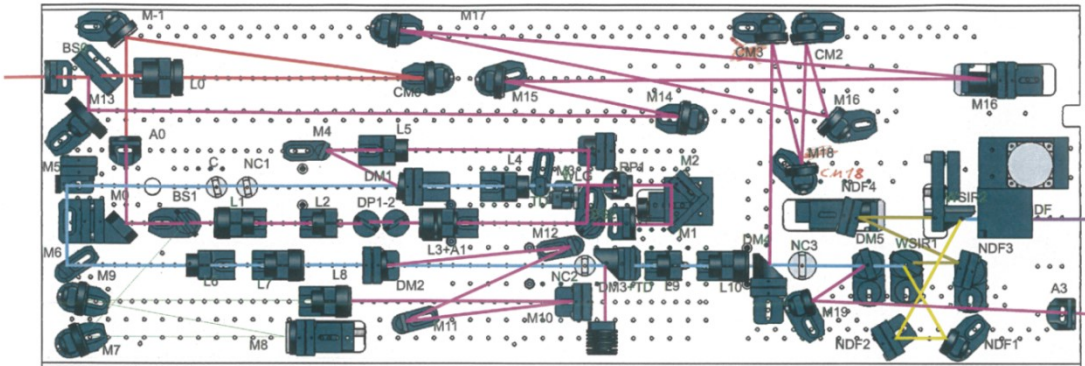


Figure 2.3: Configuration of the HE-TOPAS OPA installed at ALLS.

2.2.1 Amplification Stage of OPA

The output energy of the signal and idler beams from the OPA is low. The maximum output energy of both beams is ~ 1 mJ only. This low energy limits the application of this infrared laser source. Therefore, we use an amplification stage to increase the output energy of this laser system. The schematic diagram of this amplification stage is given below.

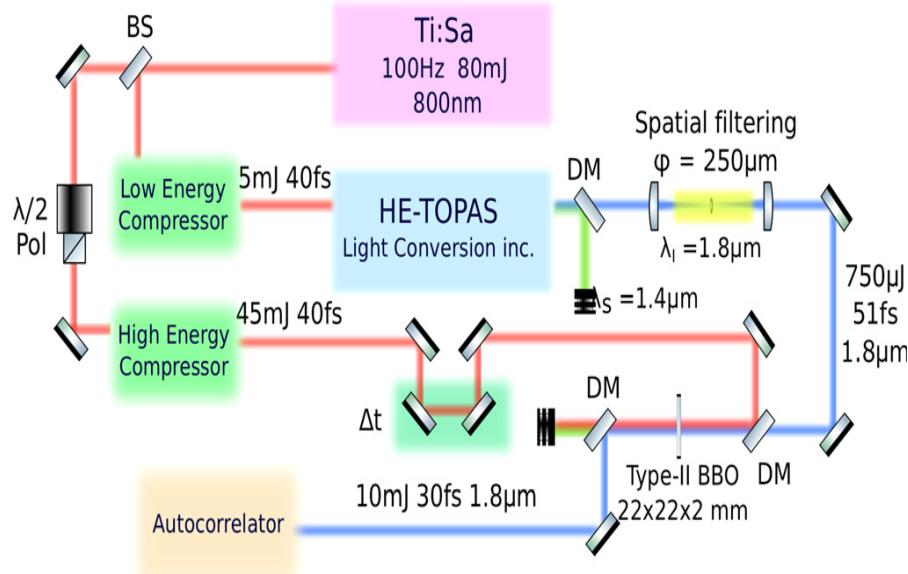


Figure 2.4: Schematic diagram of the setup used to increase the energy of the OPA; BS: Beam splitter; DM: Dichroic mirror; Pol: Polarizer; φ : Pinhole diameter used for spatial filtering; Autocorrelator: Homebuilt all reflective second harmonic generation autocorrelator; λ_i : central wavelength of the Idler of the optical parametric amplifier; high-order harmonic generation and detection setup.

Fig. 2.4 shows the schematic diagram of the amplification stage used to increase the energy of the conventional OPA (HE-TOPAS, Light Conversion, Ltd.). This setup is installed on the 100 Hz line, which can produce 80 mJ of energy at 0.8 μm wavelength. A small part of 100 Hz line (with energy \sim 5 mJ) is separated using a beam splitter (BS) and then seeded to the OPA after compression. This OPA has two outputs known as Signal ($\lambda_{\text{sig}} = 1.45 \mu\text{m}$) and Idler ($\lambda_{\text{Idl}} = 1.80 \mu\text{m}$), and the energies of these beams at specified wavelengths are \sim 1.1 mJ and 0.9 mJ respectively. The Idler beam is separated from the Signal using a dichroic mirror (DM), and then spatially filtered by focusing it through a 250 μm diameter pinhole, installed under vacuum. The transmission of this spatial filter is observed to be around 75%–80%. The remaining energy of the Ti:sapphire laser is compressed first with another double grating compressor and is then used to amplify the Idler beam using a type-II phase matching BBO crystal (22 \times 22 \times 2 mm). This laser system can produce 10 mJ of energy at 1.8 μm wavelength and the minimum pulse duration achieved is \sim 50 fs. The wavelength tuning range of Idler beam is from 1.6 μm to 2.2 μm . Further details of this intense femtosecond laser system are given in Ref. [3].

2.2.2 Hollow-core Fiber Compression

The pulse duration of the laser system after amplification is about 50 fs, at wavelength \sim 1.8 μm . This pulse duration is further reduced to 12 fs with the hollow-core fiber compression technique. The details of this hollow-core fiber compression setup are given below.

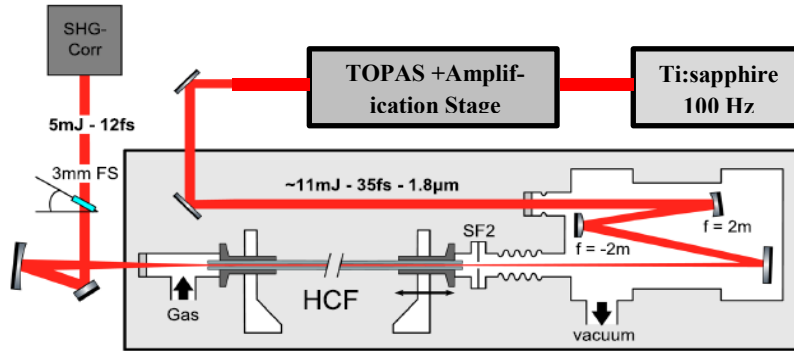


Figure 2.5: Schematic illustration of the setup used for few-cycle laser pulse generation at ALLS. Three meters long hollow-core fiber, with an inner diameter of 1mm, is used for pulse broadening and laser pulses of energy \sim 5 mJ and pulse duration \sim 12 fs are produced. Here, HCF and SHG-Corr represent the hollow-core fiber and second harmonic auto-correlator respectively [6].

For few-cycle laser pulse generation, the amplified Idler beam (discussed in section 2.2.1) are focused inside the three-meter long hollow-core fiber (HCF) with a beam coupling telescope. This telescope consists of two concave mirrors with separation around 105 cm. This beam is first passed through a spatial filtering pinhole (FS2) and then sent to the HCF. The inner diameter of this three-meter long HCF is \sim 1mm. Two fiber holders are connected with this fiber system for the gas input. All this setup is installed under vacuum and pressure is monitored at different input and output of the HCF system. Different gasses such as Ar, Kr, Ne or He are used for the pulse broadening. Finally, the output of this HCF system is compressed with a fused silica window. This laser system is capable of producing 0.42 TW laser pulses with pulse duration around 12 fs, at 1.8 μ m wavelength. Complete details of this laser system are given in Ref. [6].

2.3 High-order Harmonic Generation Setup

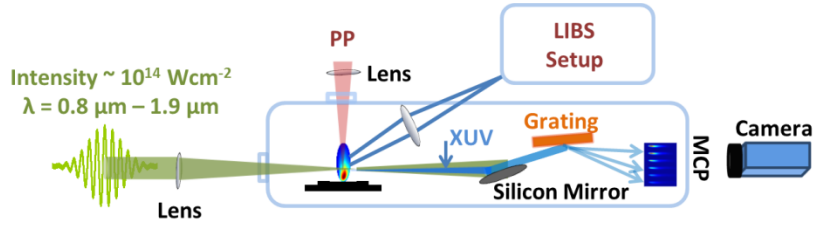


Figure 2.6: Schematic diagram of the experimental setup used for HHG from laser-ablated plumes.

For the HHG from laser-ablated plasma plume, we use two laser beams. We call these beams the prepulse (PP) and the main pulse (MP). The PP is used for the plasma ablation from the solid target, and the MP of different specification discussed in section 2.2 is used for HHG. The PP is usually separated from the laser beam before compression and is then focused on to a solid target for plume ablation. The solid target is placed inside a vacuum chamber and the pressure of this chamber is maintained at $\sim 10^{-5}$ Torr. The PP intensity is maintained at $\sim 10^{10} \text{ Wcm}^{-2}$ and plasma plume is ablated over the circular spot of $\sim 200 \mu\text{m}$. After a certain delay of few tens of nanoseconds, the MP is focused on to this LAP for harmonic generation. The delay is required between the PP and the MP so that the plasma can expand vertically from the surface. The generated harmonics are then sent to a soft X-ray spectrometer, consisting of a flat-field Hitachi grating (1200 lines/mm) and a multi-channel plate (MCP) followed by a phosphor screen.

Finally, the harmonic spectrum detected by the MCP is then captured by a 16-bit camera (CMOS, PCO-edge).

We also use time-resolved laser-induced breakdown spectroscopy (LIBS) for the visible plasma emission spectroscopy. In this technique, a computer-controlled triple grating spectrometer (Newport, MS260i; Spectral range from 200 nm to 1350 nm) is used for collecting the plasma emission. The spectral resolution of this spectrometer is ≈ 0.2 nm for the 1200 lines/mm grating, with a wavelength accuracy of 0.35 nm. The plasma emission is imaged on to the entrance slit of the spectrometer by an achromatic lens of 10 cm focal length and a magnification of ~ 2.5 . Then an ICCD camera (Andor, iStar 720) is used to record the images in a storage device. The minimum gate speed of this time-resolved system is < 2 ns, and it covers the spectral region from 115 nm to 920 nm wavelength.

References

- [1] L. B. Elouga Bom, Y. Pertot, V. R. Bhardwaj, and T. Ozaki, Opt. Express **19**, 3077 (2011).
- [2] T. Ozaki, J. C. Kieffer, R. Toth, S. Fourmaux, and H. Bandulet, Laser Part. Beams **24**, 101 (2006).
- [3] N. Thiré, S. Beaulieu, V. Cardin, A. Laramée, V. Wanie, B. E. Schmidt, and F. Légaré, Appl. Phys. Lett. **106**, 091110 (2015).
- [4] X. Ropagnol, F. Blanchard, T. Ozaki, and M. Reid, Appl. Phys. Lett. **103**, 161108 (2013).
- [5] F. Blanchard, B. E. Schmidt, X. Ropagnol, N. Thiré, T. Ozaki, R. Morandotti, D. G. Cooke, and F. Légaré, Appl. Phys. Lett. **105**, 241106 (2014).
- [6] V. Cardin, N. Thiré, S. Beaulieu, V. Wanie, F. Légaré, and B. E. Schmidt, Appl. Phys. Lett. **107**, 181101 (2015).

Chapter 3

Resonant Harmonic Generation from the Dressed Autoionizing States of Sn^+

Summary

In this chapter, we study properties of the RH of tin with mid-IR tunable driving laser pulses. These tunable pulses are used to investigate the physical phenomenon involved in RH generation. We have found that when harmonics from tin are driven with the mid-IR pulses, the RH of tin is a combination of two harmonics known as the RH, that is generated from the AIS, and the non-resonant harmonic, generated due to the normal three-step process. Further, we have observed that the RH's emission is bound within the linewidth of the AIS, whereas, the frequency of the non-resonant harmonic depends on the central wavelength of the driving laser pulses. The non-resonant harmonic is separated from the RH by carefully detuning the driving laser wavelength. This wavelength tuning exposes a new feature of the AIS of Sn^+ . We have found for the first time that the AIS of Sn^+ responds like a dressed AIS, and two coherent satellite harmonics from the dressed states are generated around the RH. The contribution of the dressed AIS in HHG is confirmed by solving the TDSE with different driving laser wavelengths.

3.1 Introduction

HHG process is explained with the semi-classical three-step model [1]. Complete details of this three-step model are described in chapter 1 (section 1.4). In this model, it is assumed that only ground state electron contributes in HHG and perturbation of atomic and ionic resonances is ignored [1,2]. The high-order harmonic spectrum, shown in **Fig. 1.3** (chapter 1), indicates that harmonic plateau consists of a series of harmonics having similar intensity. In 2006, Ganeev *et al.* [3] first observed that in harmonics from In^+ , intensity of a single harmonic in the plateau is increased. This intense single harmonic is named RH, and intensity of this RH has been observed to be about two orders of magnitude higher than the intensity of neighboring harmonic, generated with the conventional three-step process [3]. The reason behind this intensity enhancement of RH was attributed to the continuum AIS perturbing the RH intensity [3]. After that this RH has been observed in several laser-ablated media, used for HHG [4–6].

These RHs are the promising source for developing intense XUV pulses. These intense, monochromatic and narrow bandwidth XUV pulses are useful for many applications, *e.g.*, for the spectroscopy of highly charged ions [7] and the coherent diffractive imaging of nanoscale objects [8]. Also, it has been expected that these RHs might be used to produce an intense attosecond light source, by combining several resonant harmonics together [4,9].

The experimental studies of this RH generation have lacked the complete information about the physical phenomenon involved. This is because the properties of these RHs have been explored mainly to increase their photon flux [6,10,11]. Limited experiments have been performed to understand the RH generation mechanism and results of these experiments have shown that the RH intensity depends strongly on the ellipticity of the driving laser [6] and also RH follows phase matching conditions similar to other harmonics, generated with the three-step process [12].

Several theoretical models have been proposed to explain the mechanism of harmonic intensity enhancement in RH. For example, Faria *et al.* [13] proposed that this resonant enhancement might be due to the bound-bound transitions of an electron. However, bound-bound transition alone cannot explain the experimentally observed ellipticity dependence of the RH [5]. To allow ellipticity dependence in their models, other theories that consider the acceleration of the electron and the bound-bound transition have been introduced [9,14–16]. A theoretical model that has been compared with experimental observations is the four-step model, proposed by Strelkov [9]. In this model, steps 1 and 2 are the same as for the three-step model. However, in step 3, the electron accelerated in the continuum is trapped by the parent ion, so that the system lands in the AIS, and in step 4 the AIS relaxes to the ground state by emitting the harmonic photon. Experimentally observed intensity enhancements of RH have been compared with theory for several materials, and the relative phase between RH and non-RH have been experimentally measured and compared with theory [9]. However, intensity and phase measurements of the harmonics are still indirect evidence of the four-step model [17], and thus there currently lacks direct and concrete evidence that the AIS is involved in RH generation.

3.2 High-order Harmonic Generation from Sn^+

We use long-wavelengths tunable driving laser pulses ($1.75 \sim 1.90 \mu\text{m}$) to expose the physical mechanism involved in RH generation. Experimental details are described in the Chapter 2. In short, long-wavelength lasers are used to reduce the enhancement effect of the RH, compared to $0.8 \mu\text{m}$ laser pulses where RH intensity is very high. Sn^+ is used for these investigations, as Sn^+ contains a strong resonance at energy $\sim 26.3 \text{ eV}$. The high-order harmonic spectrum observed with $1.84 \mu\text{m}$ driving lasers is shown in **Fig. 3.1**.

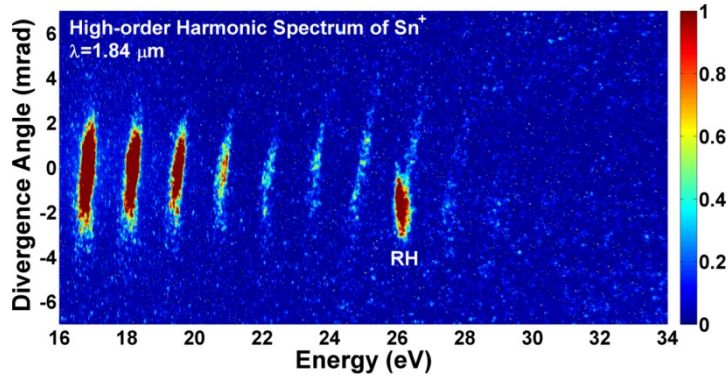


Figure 3.1: High-order harmonic spectrum of Sn^+ at $1.84 \mu\text{m}$ driving laser wavelength, showing that the RH and the non-resonant harmonic are overlapped with each other. This spectrum is recorded at laser intensity of $\sim 1.43 \times 10^{14} \text{ Wcm}^{-2}$.

Fig. 3.1 shows the high-order harmonic spectrum from tin plume with $1.84 \mu\text{m}$ driving laser wavelength. This wavelength is selected, as RH is only observable when driving laser wavelength is centered at exact or nearly exact multi-photon resonance with the atomic or ionic transition [5,6]. The driving laser pulses, centered at $1.84 \mu\text{m}$ wavelength are exactly 39-photon resonant with the $4d^9 5s^2 5p^2 \rightarrow 4d^{10} 5s^2 5p$ transition, and thus the RH of significant intensity is observed even at this high-order multiphoton interaction.

This figure also shows that around energies of 26 eV , there are actually two harmonics closely overlapped to each other. The harmonic with the higher intensity is the RH, and the other is the 39th order non-resonant harmonic from Sn^+ . This non-resonant harmonic is generated due to the conventional three-step model, where the electrons in the continuum recombine to the ground state of Sn^+ . This is in contrast to past works, which have shown that the intense RH always dominates over the much weaker non-resonant harmonic. One reason is because most of the

experimental studies on RH in the past have used driving lasers at 0.8 μm wavelength. At this laser wavelength, the intensity of the RH from Sn^+ is ~ 20 times higher than that of the non-resonant harmonic intensity [5], which makes it very difficult to distinguish the much weaker non-resonant harmonic from the RH. However, when 1.84 μm wavelength driving laser is used to generate tin harmonics, the intensity enhancement of the RH is reduced, and its intensity is observed to be only ~ 6 times higher than that of neighboring non-resonant harmonics. Therefore, the use of a long-wavelength driving laser allows one to identify this non-resonant harmonic alongside the RH. The presence of the non-resonant harmonic at the resonant energy level was actually theoretically predicted by Strelkov *et al.* [18], but no experimental signature has been revealed in the past. Therefore, our experimental observation confirms the theoretical model proposed by Strelkov, where he explains that the RH is the result of a single electron response, and the actual harmonic is a combination of the RH and the non-resonant harmonic [9,18].

Another interesting feature observed in this spectrum is that the divergence of the RH and the non-resonant harmonic is different. The divergence of the RH is observed to be smaller than the non-resonant harmonics. This different divergence of the RH and the non-resonant harmonic also helps to differentiate the non-resonant harmonic from the RH. The reason for this difference in the divergence of the two harmonics could be explained by phase matching conditions. For the non-resonant harmonics, it is the dynamics of the free electrons accelerated in the continuum that determines the wavelength shift of the harmonics. In this case, the short trajectory results in well-collimated harmonics located at the core frequencies of the harmonics, while the long trajectory results in spectrally shifted harmonics that are better phase matched off axis [19]. On the other hand, in the case of RH, the most intense harmonic emission is locked at the resonant wavelength of the strong radiative transition. Therefore, when the driving laser wavelength is in exact multiphoton resonance with the resonant wavelength, the RH is better phase matched, and the resonance forces the harmonics to be emitted at the core harmonic frequency [20], thus favoring harmonics with small divergence.

3.2.1 Resonant-Harmonic Response within the Driving Laser Bandwidth

As the driving lasers used for RH generation are broadband, the RH responds within a certain bandwidth of these laser pulses [5,17]. The RH intensity is higher when the central wavelength of the driving laser is tuned at the exact multiphoton resonance. The intensity of the RH decreases rapidly as the central wavelength is tuned away from the resonant wavelength. In our case, at laser wavelength centered at 1.84 μm , the driving laser bandwidth is ~ 100 nm. RH response at laser wavelength from 1.80 μm to 1.90 μm is investigated and results are shown in the figure below.

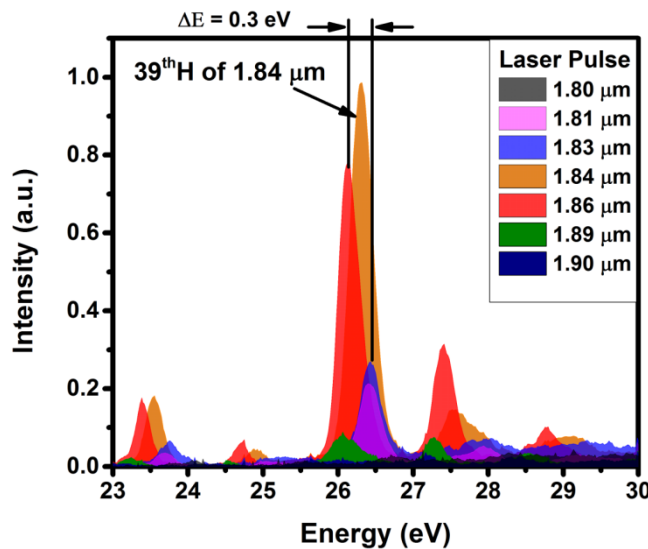


Fig. 3.2: The RH response at different driving laser wavelengths ranging from 1.80 μm to 1.90 μm . Maximum harmonic intensity is observed at 1.84 μm , as this wavelength is exactly 39-photon resonant with the $4\text{d}^{10}5\text{s}^25\text{p} \rightarrow 4\text{d}^95\text{s}^25\text{p}^2$ transition of Sn^+ , and then decreases rapidly as the driving laser wavelength is detuned. The RH disappears completely when the driving laser wavelengths are tuned at 1.80 μm and 1.90 μm . The driving laser intensity for these spectra is maintained at $\sim 1.3 \times 10^{14} \text{ Wcm}^{-2}$.

Fig. 3.2 shows the high-order harmonic spectra from tin plume around the resonance, when the central wavelength of the driving laser is varied from 1.80 μm to 1.90 μm . High RH intensity is observed at wavelength $\sim 1.84 \mu\text{m}$, as this wavelength is exactly 39-photon resonant with the 26.3 eV radiative transition of Sn^+ . The RH intensity decreases as we increase the detuning of the driving laser wavelength from this resonance. Only weak RH is observed at laser wavelengths of

1.81 μm and 1.89 μm , which disappears completely at 1.80 μm and 1.90 μm wavelengths. Therefore, these results show that when using driving lasers of \sim 100 nm bandwidth, the RH of Sn^+ responds well for at least \pm 30 nm of bandwidth, around the resonant wavelength of \sim 1.84 μm . A small energy shift of 0.3 eV is also observed in the RH when the driving laser is tuned from 1.83 μm to 1.86 μm .

As the wavelength of the RH is locked within the linewidth of the AIS, and this harmonic responds at least at 60% of the laser bandwidth, the non-resonant harmonics, which are generated due to the normal three-step process, are separated from the RH. This is done by carefully detuning the driving laser wavelength of the OPA, whose results are presented in **Fig. 3.3**.

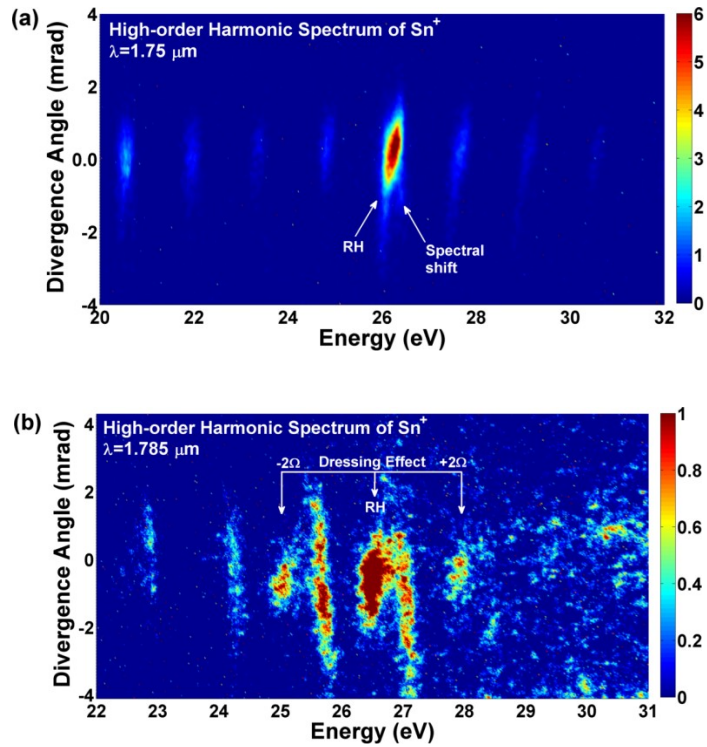


Figure 3.3: (a) High-order harmonic spectra of Sn^+ using a driving laser with $1.75 \mu\text{m}$ central wavelength, showing that the RH and the non-resonant harmonic are overlapped at 26.3 eV. (b) High-order harmonic spectrum of Sn^+ using a driving laser with $1.785 \mu\text{m}$ central wavelength. This spectrum indicates that the RH and the non-resonant harmonic can be separated by detuning the driving laser wavelength. In this spectrum two additional coherent harmonics are observed at $\pm 2\Omega$ around the RH, which are generated from the dressed AIS. The laser intensity of both spectra is maintained at $\sim 1.4 \times 10^{14} \text{ Wcm}^{-2}$.

Fig. 3.3 (a) shows the high-order harmonic spectrum of Sn^+ at $1.75 \mu\text{m}$ wavelength. This driving laser wavelength is exactly 37-photon resonant with the $4d^{10}5s^25p \rightarrow 4d^95s^25p^2$ transition, and the RH is observable at energy $\sim 26.3 \text{ eV}$. In this spectrum, a small spectral shift is observable at the tail of the RH. This spectral shift occurs due to the overlap of the RH with the 37th non-resonant harmonic of the $1.75 \mu\text{m}$ laser wavelength. We know from **Fig. 3.2** that the RH emission is bound within the linewidth of the AIS that is involved in RH generation, and this RH responds very well within the laser bandwidth of at least $\pm 30 \text{ nm}$. However, the energy of the non-resonant harmonics, which is generated with the normal three-step process, is determined by the central wavelength of the driving laser used for HHG. Therefore, when we detuned the driving laser wavelength to $1.785 \mu\text{m}$, we have observed that spectral shift between the RH and the non-resonant harmonic increases, and that both harmonics are separated from each other, as shown in **Fig. 3.3 (b)**. In the RH, a small energy shift is also observed from the resonant energy (26.3 eV), due to the detuning of the driving laser wavelength from the resonant wavelength of $\sim 1.75 \mu\text{m}$.

From this detuning of the driving laser wavelength at off-resonance, we reveal a never-considered feature of high-order harmonics. The harmonic spectra show that when the driving laser wavelength is slightly detuned, two additional harmonics appear at $\sim 25.0 \text{ eV}$ and $\sim 27.9 \text{ eV}$. These satellite harmonics are located exactly at $\pm 2\Omega$ around the RH, where Ω is the photon energy of the driving laser. The divergence of both satellite harmonics is similar to the divergence of the RH. We explain these observations as due to the generation of harmonics from the dressed AIS. In the original four-step model proposed by Strelkov [9], only a single state (the AIS in the case of Sn^+) is considered to be in multiphoton resonance with the driving laser. However, our experimental observations show that in RH generation, the continuum electron can scatter into three different states (in the third step of the four-step model); the actual AIS and the two dressed states located at $\pm 2\Omega$ around the resonant AIS. Then, in the fourth step, this scattered electron recombines to the ground state and emits three RHs. This complete mechanism of RH generation is illustrated in **Fig. 3.4**. When driving lasers with wavelength of exact multi-photon resonance is used for RH generation, the harmonics from these dressed states usually overlap with the neighboring non-resonant harmonics, and thus the two are difficult to differentiate (**Fig.**

3.3 (a)). However, these satellite harmonics can be distinguished from each other when driving lasers of slightly off-resonant wavelength are used for HHG.

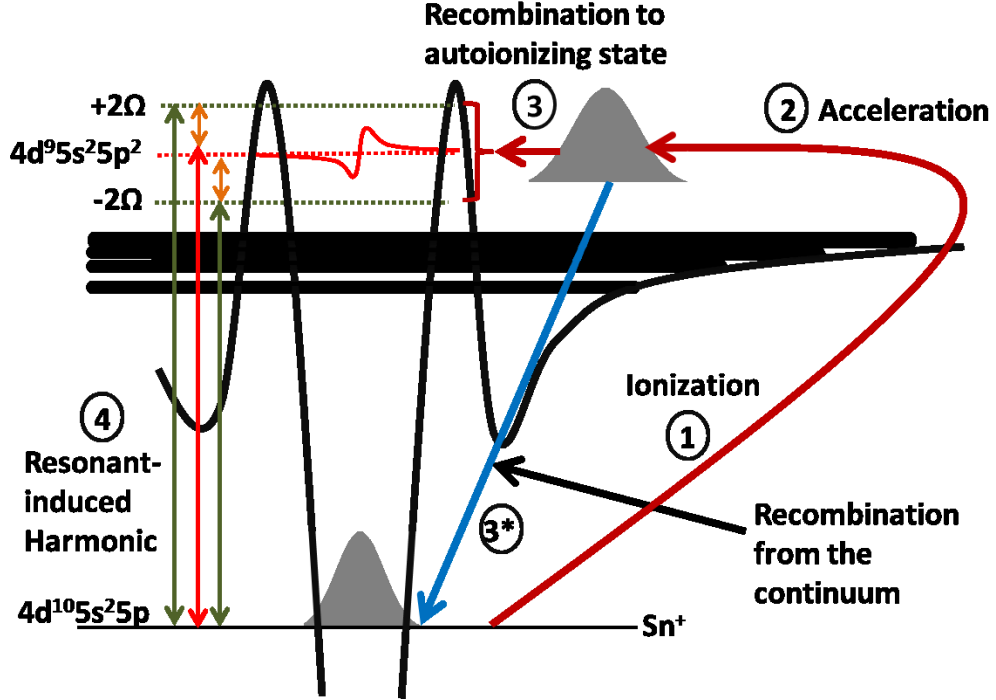


Figure 3.4: Energy diagram of the dressed AIS of Sn^+ . When high-intensity laser pulses ($\sim 10^{14} \text{ Wcm}^{-2}$) interact with the Sn^+ , an electron is liberated from the ground state (Step 1). This electron is then accelerated in the continuum by the applied laser field (Step 2). In the third step, the continuum electron has two possible paths to follow. It can either recombine directly to the ground state (Step 3*) and generate non-resonant harmonic at energy corresponding to RH energy or it can transit to the AIS (Responding as dressed AIS; Step 3) and then recombine to the ground state and generate RH (Step 4). In this scenario, there is a possibility that three coherent RHs can be generated.

3.3 Theoretical Calculations

We solve the 3D TDSE for a model Sn^+ ion in the external laser field to explain the harmonics from the dressed states. The complete details of this theoretical model are described in chapter 1 and also can be found in the Ref. [21]. In summary, the spectrum is found via numerical solution of the 3D TDSE for the model system in the laser field. Only short quantum path contribution to HHG is presented, and the long quantum path contribution is suppressed with the method suggested in Ref. [22]. The peak laser intensity is $3 \times 10^{14} \text{ Wcm}^{-2}$, the wavelength is $1.76 \mu\text{m}$, and

the laser pulse has flat-top temporal profile: that is, the intensity increases during the first 3 optical cycles, then it is constant for the next 4 optical cycles, and then decreases down to zero during the last 3 optical cycles. The calculated spectrum is shown in **Fig. 3.5**.

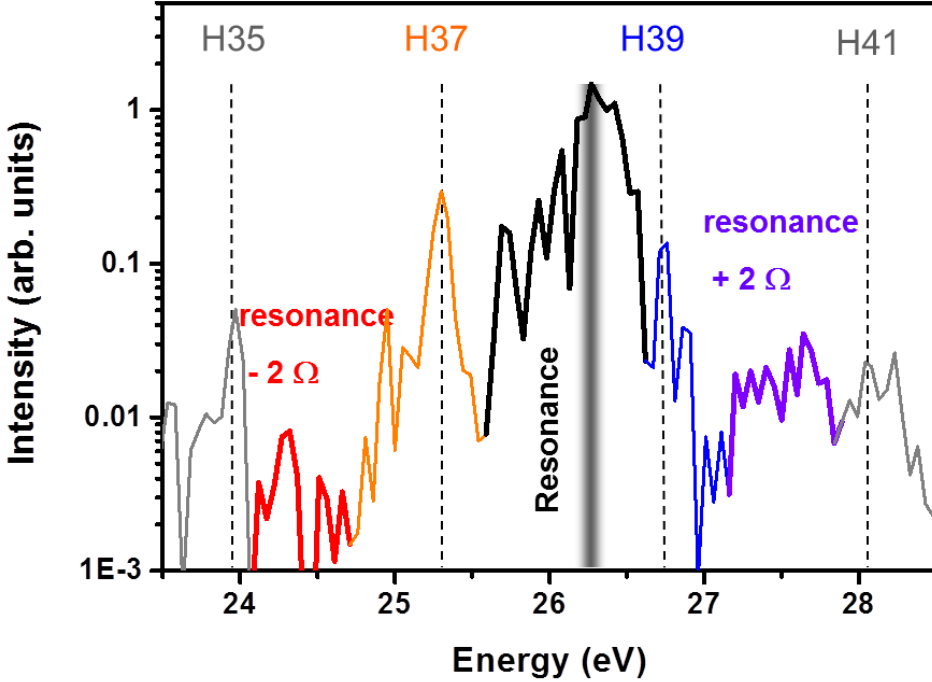


Figure 3.5: The spectrum calculated via 3D TDSE for model Sn^+ potential in $1.76 \mu\text{m}$ laser pulse; several spectral ranges chosen for further analysis are shown.

Fig. 3.5 shows the calculated extreme ultra-violet (XUV) spectrum near the resonance. In this spectrum, we see the usual 37^{th} (orange line) and the 39^{th} (blue line) harmonics, and additional peaks in between, in agreement with the experimental results. The position of the additional peak at the blue-side of the 37^{th} harmonic (purple line) is close to the exact resonance. The presence of this peak can be well-understood within the analytical theory given in Ref. [18] showing, in particular, that the line shape of the resonant harmonic is a combination of the harmonic line that would be emitted in the absence of the resonance, and the factor that is unity far from the resonance and has a sharp peak at the resonant frequency. For certain detunings of the driving laser wavelength from the resonance, this product results in a double-peak structure, where one peak is close to the harmonic frequency and the other is close to the resonance frequency.

To understand the origin of the additional peaks, appear in **Fig. 3.5**, we make the Gabor analyze of the spectrum, namely we select several peaks from the spectrum (shown in **Fig 3.5**) and study when they are emitted. The results of the Gabor analysis are presented in **Fig. 3.6**.

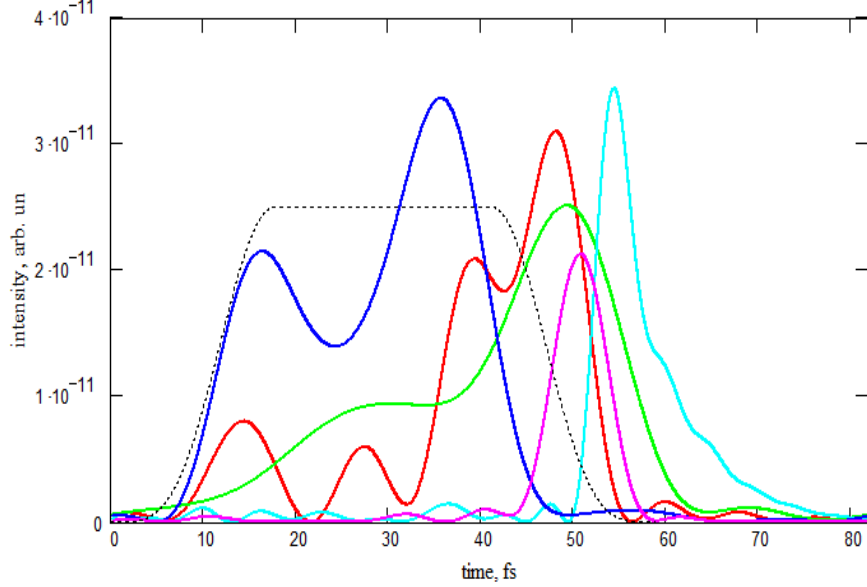


Figure 3.6: The gabor transforms showing the temporal envelopes of the emission of these spectral ranges. Dotted line in the panel presents the envelope of laser field. The curves are renormalized so that they have comparable magnitudes.

Fig. 3.6 shows the Gabor transform of the peaks appearing in the calculated spectrum. The temporal dynamics of the XUV emission with this Gabor analysis can be summarized as follows:

- The red-shifted satellite of the 37th harmonic (red line) is emitted mainly at the falling edge of the laser pulse, as it is usual for the red-shifted satellite of a harmonic [21].
- The central peak of the 37th harmonic (green line) is emitted within the top of the laser pulse and at the falling edge; such behavior is typical for the harmonic affected by resonance [22].
- The blue-shifted satellite of the 37th harmonic (light-blue line) is emitted at the falling edge of the pulse and after the pulse, thus opposite to the usual [23] blue-shifted satellite of a non-resonant harmonic. However, this behavior is typical for the resonant XUV [22], even

the exponential decrease of the emission caused by the decay of the AIS can be seen after the end of the laser pulse.

- The central peak of the 39th harmonic (blue line) is emitted mainly near the top of the laser pulse, as it should be for the non-resonant harmonic.
- The blue-shifted satellite of the 39th harmonic (magenta line) is emitted only during the falling edge of the laser pulse, but not after the pulse.

Taking into account this behavior, one can explain the emission of the blue-shifted satellite of the 39th harmonic by the resonance with the dressed AIS. Indeed, the AIS is mainly populated at the falling edge and after the pulse (see "usual resonant emission", light blue line in **Fig. 3.6**) but the dressed states exist only inside the laser pulse, not after it. Thus, the emission due to the resonance with the dressed AIS should be temporally confined within the falling edge of the pulse but not after it.

3.4 Coherence

When AIS is involved in RH generation, the common question that arises is whether RH emission is coherent or if it is a spontaneous emission from the AIS. The coherent emission of RH can be checked simply by looking into the divergence of the harmonics on the MCP. The high-order harmonics have well collimated emission that propagate collinearly with the driving laser field [24]. However, spontaneous atomic or ionic transitions are emitted in 4π direction, and thus cover the complete width of the slit, which is installed before the XUV grating. In reality, this emission angle is limited by the size of the slit, which is ~ 12 mrad. Therefore, harmonic emission can easily be differentiated from the spontaneous emission, as can be seen in **Fig. 3.7**. The divergence of the RH is observed to be much smaller than the divergence of the non-resonant harmonic, generated with the three-step process (**Fig. 3.1**). This is because the RH of Sn^+ is better phase matched for harmonic emission (details are given in the section 3.2). The low divergence of the RH indicates that RH propagates with the non-resonant harmonics in the same direction. The coherent RH emission occurs because of the short lifetime of the AIS involved in RH generation. The lifetime of the resonant state can be estimated with the line width of the AIS. The line width of the $4d^95s^25p^2$ (1D) $^2D_{5/2}$ state is $\Gamma=160$ meV, which corresponds to the life time of ~ 4.1 fs ($\tau = \hbar/\Gamma$) [11,25]. The similarity in divergence observed for the satellite

harmonics further confirms the coherent emission of the RH. Further information of the coherent RH emission can be found in references [6,12,14,26].

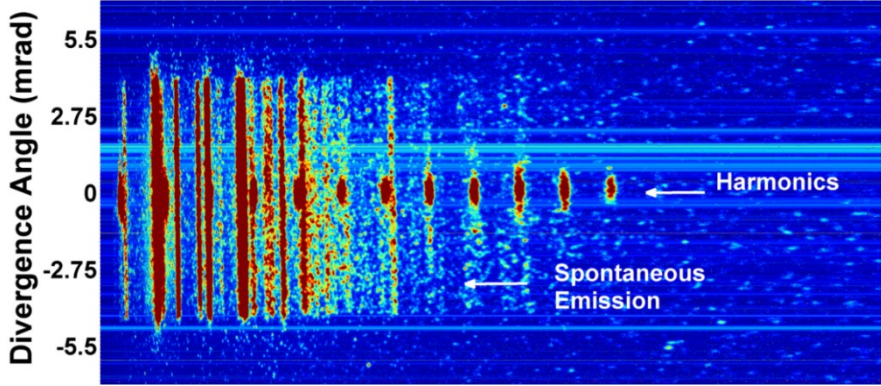


Figure 3.7: Random spectra showing collimated harmonic emission and the spontaneous emission from plasma, on the MCP.

Conclusions

Our observations provide the first direct experimental proof that the RH follows the four-step model for harmonic emission, where the electron is trapped in the AIS for a short time and then transitions to the ground state and emits intense coherent harmonic. The results confirm that when RH is emitted, the contribution from the non-resonant harmonic that follows the three-step model is always present. The presence of both resonant and non-resonant harmonics at the same energy level is interesting, as it will provide us with a new tool to study the ultrafast dynamics of the AIS, such as the electron-electron interaction in the continuum at the attosecond time scale [27–30]. Up to now, the study of AIS at the attosecond timescale has required the generation of sufficiently intense, isolated attosecond pulses, which is not a trivial task [31,32]. However, the current results show that one could alternatively use near-infrared lasers to generate attosecond electron bunches whose energy is in multiphoton resonance, to excite AIS and subsequently to study their dynamics. The observation of harmonics from dressed AIS is also important in terms of the application of the intense RH. Correct knowledge on the phase and intensity of RH (from both dressed and non-dressed AIS) would be important in determining and optimizing the temporal shape of this intense source of coherent XUV radiation, for use in various applications [7,32,33].

References

- [1] P. Corkum, Phys. Rev. Lett. **71**, 1994 (1993).
- [2] P. Corkum and F. Krausz, Nat. Phys. **3**, 381 (2007).
- [3] R. A. Ganeev, M. Suzuki, M. Baba, H. Kuroda, and T. Ozaki, Opt. Lett. **31**, 1699 (2006).
- [4] R. A. Ganeev, High-Order Harmonic Generation in Laser Plasma Plumes (World Scientific, 2013).
- [5] M. Suzuki, M. Baba, R. A. Ganeev, H. Kuroda, and T. Ozaki, Opt. Lett. **31**, 3306 (2006).
- [6] T. Ozaki, R. A. Ganeev, M. Suzuki, and H. Kuroda, In Tech, 2010.
- [7] W. Nörterhäuser, Hyperfine Interact. **199**, 131 (2011).
- [8] M. D. Seaberg, D. E. Adams, E. L. Townsend, D. A. Raymondson, W. F. Schlotter, Y. Liu, C. S. Menoni, L. Rong, C.-C. Chen, J. Miao, H. C. Kapteyn, and M. M. Murnane, Opt. Express **19**, 22470 (2011).
- [9] V. Strelkov, Phys. Rev. Lett. **104**, 123901 (2010).
- [10] R. A. Ganeev, C. Hutchison, A. Zaïr, T. Witting, F. Frank, W. A. Okell, J. W. G. Tisch, and J. P. Marangos, Opt. Express **20**, 90 (2012).
- [11] R. A. Ganeev, V. V. Strelkov, C. Hutchison, A. Zaïr, D. Kilbane, M. A. Khokhlova, and J. P. Marangos, Phys. Rev. A - At. Mol. Opt. Phys. **85**, 023832 (2012).
- [12] N. Rosenthal and G. Marcus, Phys. Rev. Lett. **115**, 133901 (2015).
- [13] C. F. D. M. Faria, R. Kopold, W. Becker, and J. M. Rost, Phys. Rev. A **65**, 023404 (2001).
- [14] L.-B. Elouga-Bom, F. Bouzid, F. Vidal, J.-C. Kieffer, and T. Ozaki, J. Phys. B. **41**, 215401 (2008).
- [15] M. Plummer and C. J. Noble, J. Phys. B. **35**, L51 (2002).
- [16] R. Taïeb, V. Véniard, J. Wassaf, and A. Maquet, Phys. Rev. A **68**, 033403 (2003).
- [17] S. Haessler, V. Strelkov, L. B. Elouga Bom, M. Khokhlova, O. Gobert, J. F. Hergott, F. Lepetit, M. Perdrix, T. Ozaki, and P. Salières, New J. Phys. **15**, 013051 (2013).
- [18] V. V Strelkov, M. A. Khokhlova, and N. Y. Shubin, Phys. Rev. A **89**, 53833 (2014).
- [19] E. Brunetti, R. Issac, and D. A. Jaroszynski, Phys. Rev. A **77**, 023422 (2008).
- [20] M. Chini, X. Wang, Y. Cheng, H. Wang, Y. Wu, E. Cunningham, P.-C. Li, J. Heslar, D. A. Telnov, S.-I. Chu, and Z. Chang, Nat. Photonics **8**, 437 (2014).
- [21] V. V Strelkov, A. F. Sterjantov, N. Y. Shubin, and V. T. Platonenko, J. Phys. B. **39**, 577 (2006).
- [22] M. Tudorovskaya and M. Lein, Phys. Rev. A. **84**, 013430 (2011).
- [23] M. Gaarde, F. Salin, E. Constant, P. Balcou, K. Schafer, K. Kulander, and A. L'Huillier, Phys. Rev. A **59**, 1367 (1999).
- [24] C. Winterfeldt, C. Spielmann, and G. Gerber, Rev. Mod. Phys. 80, 117 (2008).
- [25] H. Wang, M. Chini, S. Chen, C.-H. Zhang, F. He, Y. Cheng, Y. Wu, U. Thumm, and Z. Chang, Phys. Rev. Lett. **105**, 143002 (2010).
- [26] J. Rothhardt, S. Hädrich, S. Demmler, M. Krebs, S. Fritzsche, J. Limpert, and A. Tünnermann, Phys. Rev. Lett.

- 112**, 033002 (2014).
- [27] N. Dudovich, O. Smirnova, J. Levesque, Y. Mairesse, M. Y. Ivanov, D. M. Villeneuve, and P. B. Corkum, *Nat. Phys.* **2**, 781 (2006).
- [28] P. Eckle, A. N. Pfeiffer, C. Cirelli, A. Staudte, R. Dörner, H. G. Müller, M. Büttiker, and U. Keller, *Science* **322**, 1525 (2008).
- [29] K. Schiessl, K. Ishikawa, E. Persson, and J. Burgdörfer, *Phys. Rev. Lett.* **99**, 253903 (2007).
- [30] A. Zaïr, M. Holler, A. Guandalini, F. Schapper, J. Biegert, L. Gallmann, U. Keller, A. S. Wyatt, A. Monmayrant, I. A. Walmsley, E. Cormier, T. Auguste, J. P. Caumes, and P. Salières, *Phys. Rev. Lett.* **100**, 143902 (2008).
- [31] T. Popmintchev, M.-C. Chen, D. Popmintchev, P. Arpin, S. Brown, S. Alisauskas, G. Andriukaitis, T. Balciunas, O. D. Mücke, A. Pugzlys, A. Baltuska, B. Shim, S. E. Schrauth, A. Gaeta, C. Hernández-García, L. Plaja, A. Becker, A. Jaron-Becker, M. M. Murnane, and H. C. Kapteyn, *Science* **336**, 1287 (2012).
- [32] Y. Wu, E. Cunningham, H. Zang, J. Li, M. Chini, X. Wang, Y. Wang, K. Zhao, and Z. Chang, *Appl. Phys. Lett.* **102**, 201104 (2013).
- [33] C. Ott, A. Kaldun, L. Argenti, P. Raith, K. Meyer, M. Laux, Y. Zhang, A. Blättermann, S. Hagstotz, T. Ding, R. Heck, J. Madroñero, F. Martín, and T. Pfeifer, *Nature* **516**, 374 (2014).

Chapter 4

Role of Inner-shell 3p-3d Resonances in High-order Harmonic Generation

Summary

In this chapter, we study the role of inner-shell resonances in HHG. Manganese is used as a nonlinear medium, as this material contains strong inner-shell resonance at energy ~ 51 eV. It is observed that from laser-ablated manganese plume, high-order harmonics up to 125 eV are generated, when driven with $0.8\text{ }\mu\text{m}$ driving lasers. In laser-ablated manganese plume, Mn^+ is observed as an active species responsible for HHG. From Mn^+ , two high-order harmonic series are generated. The first harmonic series consists of harmonics up to ~ 48 eV. After that, the second harmonic series starts from 51 eV and harmonics up to 125 eV are generated. The physical mechanism involved behind this second harmonic series generation was uncertain. We used mid-IR laser pulses ($\sim 1.82\text{ }\mu\text{m}$) to investigate the mechanism involved and revealed that this second harmonic series is generated from the inner-shell 3p-3d resonance of Mn^+ .

4.1 Introduction

HHG from LAP is a unique way to generate highly efficient coherent pulses of XUV radiation [1–4]. This is a promising technique to develop a tabletop HHG source with high photon flux [5–7]. In this technique, the HHG process is interpreted within the framework of the semi-classical three-step model [8,9]. The complete details of this model are described in Chapter 1. In summary, when ultrafast laser pulses with peak intensity of $\sim 10^{14}\text{ Wcm}^{-2}$ interact with an atom or molecule, an electron is liberated from the ground state to the continuum via tunnel-ionization. In the second step, this electron is accelerated in the continuum by the applied laser field, and finally some of the laser trajectories (known as long and short trajectories) allow this electron to recombine again to the ground state and emit XUV radiation [10]. In this way, high-order harmonics with very high photon energy are generated [11,12]. This semi-classical three-step model explains correctly the cutoff energy of the harmonics that can be generated from a specific element. This cutoff energy of the harmonics can be estimated using the cutoff rule given in Eq. 1.12.

This model estimates the high-order harmonic cutoff accurately. **Eq. 1.12** ($E_{cutoff} = I_p + 3.17U_p = I_p + 9.33 \times 10^{14} I\lambda^2$) indicates that the high-order harmonic cutoff is proportional to the driving laser intensity and the square of the wavelength. Therefore, for a specific element having fixed ionization potential, the high-order harmonic cutoff can be increased by increasing the laser pulse intensity and the wavelength.

It is observed that the laser pulse intensity is limited up to a certain limit, called the saturation intensity [4]. The saturation intensity is known as the intensity where the nonlinear medium is almost fully ionized, and high-order harmonic cutoff saturates. The other possible way of increasing this cutoff is to increase the driving laser wavelength. Extensive work [13–15] has been done in this direction and high-order harmonics up to 1.5 keV have been demonstrated with the 3.9 μm driving laser pulses, using helium as the nonlinear medium [12]. One disadvantage of using long-wavelengths for HHG is that when we increase the driving laser wavelength, high-order harmonic efficiency reduces drastically. This is mainly due to the quantum diffusion of the wave packet, since electron takes a longer time to propagate in the continuum [14,16,17].

From **Eq. 1.12**, the third possibility of increasing high-order harmonic cutoff is to generate harmonics with elements having large ionization potential. With this method, the high-order harmonic cutoff increases due to the increase in gain energy that the electron experiences while recombining with the parent ion. In the LAP technique, high-order harmonic from neutral atoms and singly charged ions has been demonstrated successfully [4], whereas in gaseous media, contribution of doubly charged ions have been observed in HHG [18]. Regarding the ionization potential, this high-order harmonic cutoff can be further increased if we use highly charged ions for the HHG. However, preparation of nonlinear medium of highly charged ions with sufficient number density (10^{16} to 10^{17} cm^{-3}) is not an easy task.

The alternative of using highly charged ions to generate harmonics up to very high energy, is to use inner-shell electrons for HHG. In the three-step model, it is assumed that only ground state electron contributes to HHG, and this electron can only gain energy from the parent ion equivalent to the ionization energy [9]. However, if the continuum electron recombines to the inner-shells, it can gain even more energy. This is because the energy that electron will experience from the parent ion will be the sum of the ionization energy and the energy difference

between the ground state and the inner-shell energy level where the continuum electron will recombine. The contribution of inner-shell electrons in HHG was first observed by Shiner *et al.* [19], in the harmonics from Xenon. Shiner *et al.* observed that when few-cycle long-wavelength laser pulses (centered at $\sim 1.8 \mu\text{m}$) interact with Xenon, the inner-shell resonances of Xenon are perturbed and these inner-shell resonances lead to generate broadband harmonics around 100 eV. Shiner *et al.* explained that this phenomenon of harmonic generation, along with the contribution of inner inner-shell electrons, can be explained as exchange in energy between the continuum electron and the electron from the inner-shell $4d \rightarrow 5p$ resonance. According to Shiner *et al.*, when inner-shell resonances are involved in HHG, the HHG process can be explained as,

- i. When laser-pulses interact with Xe, an electron is ionized from the ground state.
- ii. This electron accelerates in the continuum by the applied laser field.
- iii. When the continuum electron returns back to the parent ion, an inelastic collision occurs and the continuum electron exchange energy with the electron located at inner-shell 4d state and 4d electron is promoted to the 5p state of Xe.
- iv. Finally, the continuum electron recombines to the inner-shell 4d state.

According to Shiner *et al.*, this process of energy exchange occurs due to the energetic inelastic collision of continuum electron that has large kinetic energy, compared to the energy difference of 4d-5p state of Xenon (~ 56 eV). In this inelastic collision, the continuum electron loses energy first and then regains this energy while recombining to the inner shell 4d state. In this process of HHG, the harmonic efficiency increases about one order of magnitude at energy ~ 100 eV.

In solid materials, there are several elements that contain strong inner-shell resonances in the soft X-ray region [20–22]. For example, the 3d elements of the periodic table (Sc to Cu) contain inner-shell resonances in region from 35 eV to 75 eV [23]. These resonances mainly occur due to the 3p-3d transitions that have large PICS. The photoabsorption spectra of these 3d elements from Sc to Cu are shown in **Fig. 4.1**.

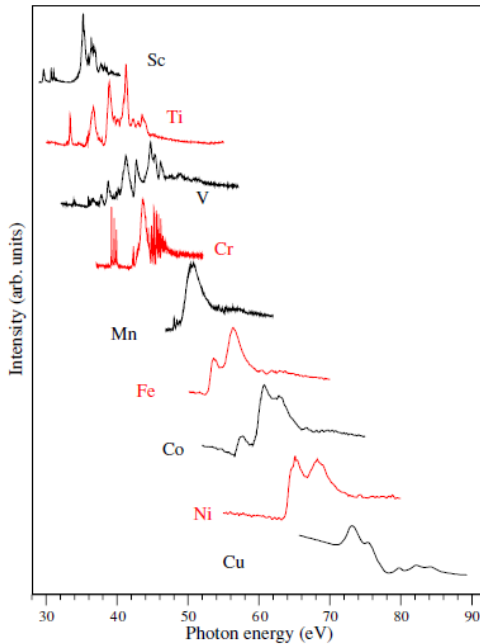


Figure 4.1: Experimental photoabsorption spectra of 3d metals (Sc to Cu), showing strong resonance in the XUV region. These resonances mainly occur due to the 3p-3d excitations [23].

4.2 High-order Harmonic Generation from Manganese

From these 3d elements, manganese is selected as the nonlinear medium to check the contribution of inner-shell resonances in HHG. In the first step of experiments, driving laser of central wavelength $\sim 0.8 \mu\text{m}$ (pulse duration $\sim 42 \text{ fs}$) is used for HHG. The high-order harmonic spectrum observed with $0.8 \mu\text{m}$ driving laser pulses is shown in **Fig. 4.2**.

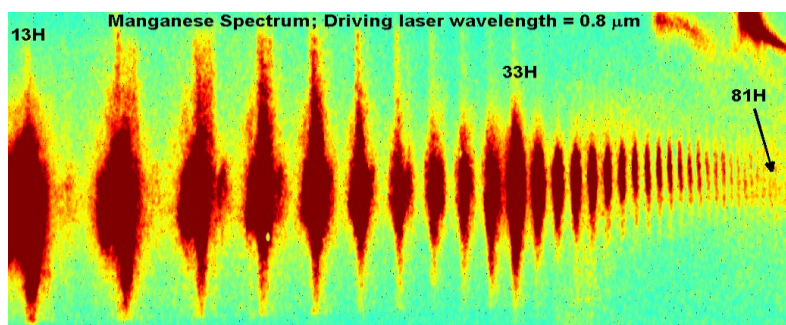


Figure 4.2: High-order harmonic spectrum from manganese, generated with the $0.8 \mu\text{m}$ driving lasers. This spectrum shows that high-order harmonics up to 81^{st} order ($\sim 125 \text{ eV}; 9.87 \text{ nm}$) are generated from manganese, at laser intensity $\sim 1 \times 10^{15} \text{ Wcm}^{-2}$. This harmonic spectrum contains two harmonic series, where the second harmonic series starts from 33^{rd} order.

It has been observed that from manganese plume, high-order harmonics up to the 81st order (~ 125 eV; 9.87 nm) are generated with ~ 0.8 μm driving lasers. In a typical HHG process, high-order harmonic spectrum consists of a plateau and cutoff (details given in chapter 1). The plateau contains a series of virtually flat harmonics, and the cutoff gives the maximum harmonic order that can be generated from a specific element. However, in the high-order harmonic spectrum from manganese, two high-order harmonic series are generated and this second harmonic series starts from energy ~ 51 eV. The first high-order harmonic series consist of harmonics up to the 31st order. After that, the second harmonic series starts from the 33rd order and harmonics up to the 81st order or higher values are generated. We have noticed that this second harmonic series is only observable when driving lasers of high intensity are used for HHG. For example, the spectrum presented in **Fig. 4.2** is recorded with a laser intensity of $\sim 1.0 \times 10^{15} \text{ Wcm}^{-2}$. This laser intensity is about an order of magnitude higher than the normal laser intensity we use for HHG from other laser-ablated materials ($\sim 10^{14} \text{ Wcm}^{-2}$) [4].

There could be two reasons that might be involved in the generation of this second harmonic series. The first possibility is that the laser-ablated manganese plume might contain species with large ionization potential (*e.g.* Mn^{2+} or Mn^{3+}) and high-order harmonics are generated from them. This could be checked by scaling the harmonic cutoff with the ionization potential [4,11]. The second possibility is that the inner-shell electrons are contributing to HHG [19,24,25]. In further discussions, we will investigate the role of both possibilities to find the actual phenomenon involved behind this second harmonic series generation.

4.2.1 High-order Harmonic Cutoff Scaling with the Ionization Potential

In HHG, cutoff is estimated accurately with the three-step model [9]. The details of this model are explained in Chapter 1 and also in the introduction section of this chapter. According to this model, high-order harmonic cutoff depends on the ionization potential and the ponderomotive energy that an electron can gain in the continuum. For a specific element with certain ionization potential, the high-order harmonic cutoff can be estimated with this three-step model.

The active species responsible for HHG in laser-ablated manganese plume is uncertain. Therefore, first we check the dominant species in laser-ablated manganese plume that is responsible for HHG. Let's assume that the laser-ablated manganese plume contains Mn, Mn^+ and Mn^{2+} . The ionization potentials of these species are, $\text{Ip}_{\text{Mn}} = 7.43 \text{ eV}$, $\text{Ip}_{\text{Mn}^+} = 15.64 \text{ eV}$ and $\text{Ip}_{\text{Mn}^{2+}} = 34 \text{ eV}$. For a fixed LAP size ($\sim 200 \mu\text{m}$ width), the high-order harmonic cutoff increases linearly with the ionization potential, at laser intensities close to the saturation intensity [11]. Ganeev *et al.* scaled the high-order harmonic cutoff of different laser-ablated species and found that the harmonic cutoff observed from manganese plume agrees well with the ionization potential of Mn^{2+} . The variation of the high-order harmonic cutoff with the ionization potential of different species is given in **Fig. 4.3**.

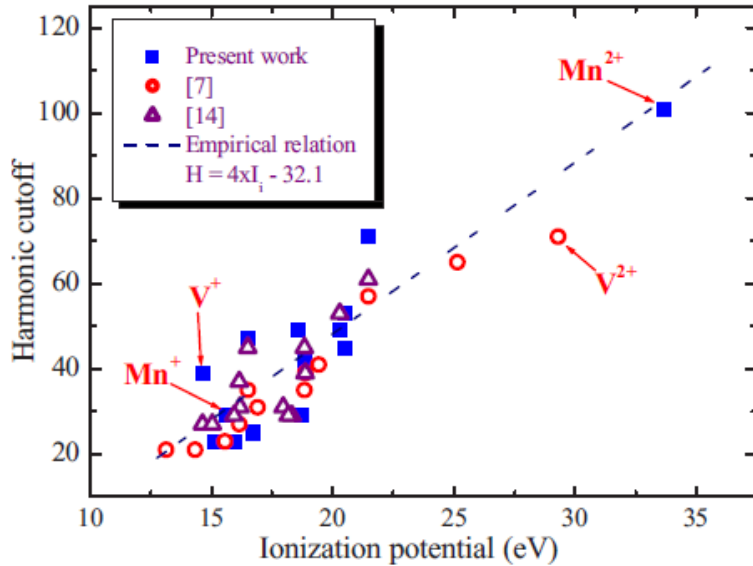


Figure 4.3: High-order harmonic cutoff scaling with the ionization potential. This scaling shows that the high-order harmonic cutoff increases linearly with the ionization potential and that the high-order harmonic cutoff from manganese agrees very well with the ionization potential of Mn^{2+} [11].

4.2.2 Role of Inner-shell Resonances in HHG

The second phenomenon that might be involved in double harmonic series generation could be the involvement of inner-shell resonances. The contribution of inner-shell electrons in HHG was first observed by Shiner *et al.* in high-order harmonics from Xenon [19]. He observed that when inner-shell resonances of Xenon [26,27] are perturbed, broadband harmonics of bandwidth ~ 30

eV are generated at energy \sim 100 eV. In solid materials, several elements contain inner-shell resonances and their properties have been mainly studied with the photoabsorption spectroscopy [20,22,23]. The data of photoabsorption spectroscopy shows that manganese contains a strong resonance around \sim 51 eV [20]. This resonance in manganese appears mainly from the inner-shell 3p-3d transitions. We check if these inner-shell resonances of manganese contribute in second harmonic series generation.

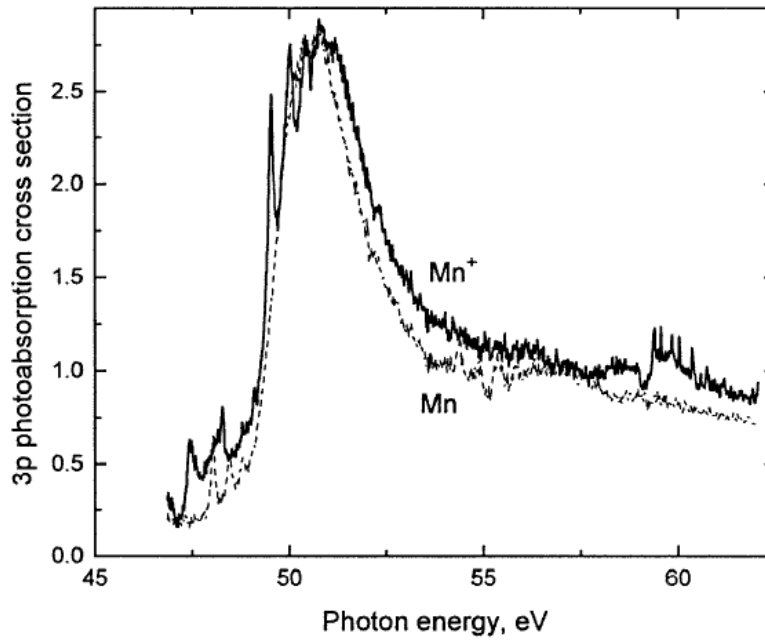


Figure 4.4: Photoabsorption spectra of Mn and Mn⁺ [22] showing the photoabsorption cross-section.

Fig. 4.4 shows the photoabsorption spectra of Mn and Mn⁺, reported by Dolmatov *et al.* [22]. These spectra indicate that the PICS of both Mn and Mn⁺ is high at \sim 51 eV. In the photoabsorption spectrum of Mn⁺, some additional peaks appear at energy around 50 eV that results from the 3p-4s transitions of Mn⁺ [20]. In the next discussion, we will check the role of these two resonances (3p-3d and 3p-4s) for coherent harmonic emission. The spectroscopic parameters, such as the oscillator strength and the lifetime, are the essential parameters to check the perturbation of bound atomic or ionic states in HHG [6,28]. Therefore, the spectroscopic parameters of the Mn⁺ resonances are collected from the literature and are listed in **Table 4.1**.

Table 4.1: Spectroscopic parameters of Mn^+ such as the energy, oscillator strength, linewidth and lifetime of the $3\text{p}^53\text{d}^64\text{s}$ and $3\text{p}^53\text{d}^54\text{s}^2$ ${}^7\text{P}$ resonances, showing the effects of configuration mixing on the $3\text{p}^53\text{d}^54\text{s}^2$ resonances [29].

State	Energy (eV)	F	Γ (eV)	$\tau = \hbar/\Gamma$ (fs)
$3\text{d}^54\text{s}^2$ ${}^7\text{P}_4$	49.33	0.128	0.115	5.723
$3\text{d}^54\text{s}^2$ ${}^7\text{P}_3$	49.82	0.135	0.201	3.274
$3\text{d}^54\text{s}^2$ ${}^7\text{P}_2$	50.18	0.065	0.373	1.764
$3\text{d}^64\text{s}$ ${}^7\text{P}_2$	51.28	0.408	2.67	0.246
$3\text{d}^64\text{s}$ ${}^7\text{P}_3$	51.41	0.642	2.84	0.231
$3\text{d}^64\text{s}$ ${}^7\text{P}_4$	51.61	0.866	2.93	0.224

The resonant bound states of atoms/ions contribute in HHG when the oscillator strength of the corresponding state is large [4]. The spectroscopic data of Mn^+ (listed in **Table 4.1**) shows that the oscillator strength of the $3\text{p}^53\text{d}^64\text{s} \rightarrow 3\text{p}^63\text{d}^54\text{s}$ transition is very high, indicating that this transition can considerably perturb the HHG process. As we know from **Fig. 4.4** that the PICS of manganese is high around 50 eV, one way of checking the perturbation of this resonant state for HHG should be to compare the harmonic spectra with the PICS. This is because recent theoretical [30] and experimental [19] studies show that the harmonic spectrum closely follows the PICS of the responsible species participating in HHG. The complete details of this method are described in Chapter 5. Therefore, we compare the PICS with the harmonic spectrum to check if the high-order harmonic spectrum follows the PICS of laser-ablated manganese species.

The PICS of an element can be calculated simply with the equation,

$$\sigma(\lambda) = 2r_e \lambda f_2 \quad (4.1)$$

Here r_e (2.82×10^{-13} cm), λ [cm] and f_2 are the electron radius, driving laser wavelength and scattering factor, respectively. The value of the scattering factor of different species can be collected from Ref. [31]. The energy variation of the PICS is calculated with **Eq. 4.1** and then compared with the harmonic spectrum, as shown in **Fig. 4.5**.

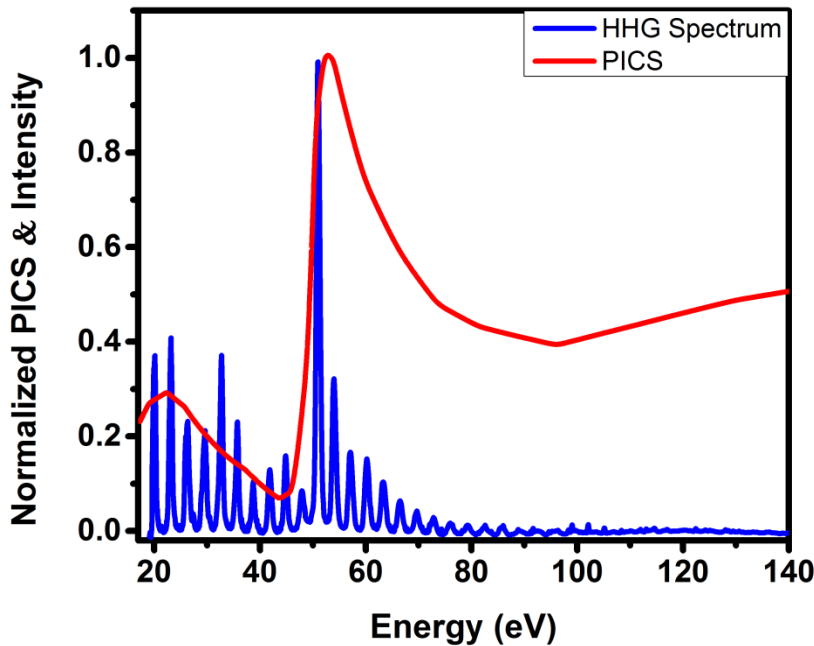


Figure 4.5: Comparison of the photoionization cross-section of manganese with the HHG spectrum.

We observe similar energy variation in the PICS and the HHG spectrum, particularly around 50 eV, as can be seen in **Fig. 4.5**. We know from **Fig. 4.4** that the PICS around 51 eV is large because of the inner-shell 3p-3d resonance of manganese. As high-order harmonic spectrum is showing high perturbation at 51 eV, the role of inner-shell 3p-3d transition becomes important in second harmonic series generation. However, from this spectrum, observed with 0.8 μm driving lasers, it is not clear that either the second harmonic series is generated from Mn or Mn^+ , as the 3p-3d resonance of both species is at same energy (~ 51 eV). One way of checking the contribution of Mn and Mn^+ in HHG is to see the cutoff of first harmonic series. In **Fig. 4.5**, we can see that high-order harmonics up to the 31st order belong to the first harmonic series. If we scale this cutoff with the ionization potential, shown in **Fig. 4.3**, the first harmonic series belongs to Mn^+ . Therefore, the probability of Mn^+ for second harmonic series generation is high.

When resonant bound states contribute in HHG, the main question that arises is whether the harmonic emission is coherent or not. In chapter 3, we have observed that the coherent emission of harmonics from resonant states depend mainly on the lifetime of the state involved in HHG. We know that the lifetime of the atomic or ionic state is associated with the line width of the state and can be estimated with the relation $\tau = \hbar/\Gamma$. The line width of the $3p^53d^64s$ state of Mn^+

is listed in **Table 4.1**, which shows that the lifetime of the 3d state is only few hundreds of attoseconds. This life time is even shorter than the lifetime of the continuum AIS lying above the ionization threshold that contribute in intensity enhancement of single resonant-harmonic. For example, the lifetime of the AIS of Sn^+ is 4.1 fs [4].

This large oscillator strength and the short lifetime of the 3d state of Mn^+ indicate that the 3p-3d resonance can considerably perturb the HHG process. The comparison of PICS with the high-order harmonic spectrum and the spectroscopic parameters supports that the intensity enhancement in manganese harmonics (~51 eV) is from the 3p-3d resonance. The manganese spectrum shows that this inner-shell resonance not only increases the intensity of the harmonic around the resonance energy, but generates a series of harmonics up to very high energy (~125 eV with 0.8 μm). This could be because of the additional energy gap that the electron experience while recombining to the inner-shell 3p state.

From the above observations and discussions, we conclude that the second harmonic series could be generated from the 3p-3d resonance of Mn^+ and also when these inner-shell resonances contribute to HHG, two high-order harmonic series are generated from a single element. The second harmonic series starts from the resonance energy and harmonics up to very high energy are generated even with 0.8 μm driving laser pulses.

The photoabsorption spectrum of Mn^+ (given in **Fig. 4.4**) shows that two states contribute in increasing the PICS around 51 eV. These are the 3d and 4s states located at energies 51.6 eV and 50.16 eV, respectively. We also know from chapter 3 that when atomic resonances are involved in HHG, the non-resonant harmonic generated due to three-step process is overlapped with the resonant harmonic. Therefore, one question arising at this stage is that if the 3d inner-shell resonance is really involved in HHG, we should observe several peaks around 51 eV. However, the high-order harmonic spectrum shown in **Fig. 4.5** indicates that there is only one peak at ~51 eV. This could be because we are not using proper driving laser wavelength to hit the other resonances around the resonant energy. As such, we use long-wavelength tunable driving laser pulses to check the contribution of other resonant and non-resonant harmonics around 51 eV.

4.3 Harmonic Generation with Long-wavelength Driving Lasers

Long-wavelength laser pulses are used for HHG, and the observed harmonic spectra from manganese plume are presented in **Fig. 4.6**.

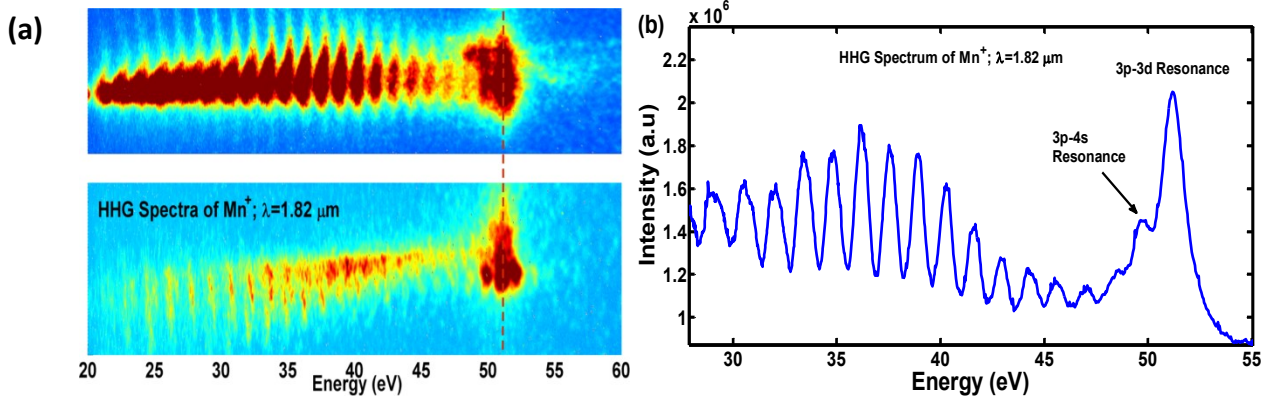


Figure 4.6: (a). High-order harmonic spectra from manganese plume at 1.82 μm driving laser wavelength. Harmonic intensity increases at 51 eV because of the 3p-3d resonance and the intensity of neighboring harmonic (observed at energy \sim 50 eV) is high because of the 3p-4s resonance. (b). Line plot of the harmonic spectrum showing the perturbation in harmonic intensity from 3p-3d and 3p-4s resonances.

Fig 4.6 shows the high-order harmonic spectra generated from manganese plume with 1.82 μm driving lasers. These spectra are recorded at laser pulse intensity $\sim 4.0 \times 10^{14} \text{ Wcm}^{-2}$. **Fig. 4.6 (a)** shows that the harmonic intensity at \sim 51 eV is high (marked with the light brown line). This is the 75th order harmonic of 1.82 μm wavelength. Similarly, the intensity of the 73rd harmonic is also observed to be high compared to the intensity of the 71st and lower order harmonics of the first harmonic series. In **Fig. 4.5**, we observed that when harmonics are driven with 0.8 μm driving lasers, the high-order harmonic intensity increases at 51 eV only. However, with 1.82 μm driving lasers, the enhanced intensity of the 73rd order harmonic (located at \sim 50 eV) infers that perturbation in lower energy harmonics is coming from the 3p-4s resonance. This perturbation in harmonic intensity in the lower energy harmonic (\sim 50 eV) is observed consistently and is direct evidence that the electrons from inner-shell 3p states are participating in HHG. This observation also confirms that in laser-ablated manganese plume, Mn⁺ is responding as an active species responsible for HHG. **Fig. 4.6 (b)** is the line plot of the high-order harmonics, showing intensity perturbation in harmonics around 51 eV.

Conclusions

From all these observations, we conclude that in laser-ablated manganese plume, Mn^+ is the major active species responsible for HHG. From Mn^+ , two high-order harmonic series are generated, where the second harmonic series starts from 51 eV. This second harmonic series is generated from the inner-shell 3p-3d resonance that increases the harmonic cutoff up to very high energy from the elements having low ionization potential ($I_{\text{p}}\text{Mn}^+ = 15.64 \text{ eV}$). In Mn^+ , there are two major resonances that appears from 3p-3d and 3p-4s transitions. When we use 0.8 μm driving laser pulses, only 3p-3d resonance contribute in HHG. However, when driving laser wavelength is increased, the contribution of 3p-4s resonance in HHG also appears in the spectrum.

References

- [1] R. A. Ganeev, L. B. Elouga Bom, J. Abdul-Hadi, M. Wong, J. Brichta, V. Bhardwaj, and T. Ozaki, Phys. Rev. Lett. **102**, 013903 (2009).
- [2] R. A. Ganeev, M. Suzuki, M. Baba, and H. Kuroda, Appl. Phys. Lett. **86**, 131116 (2005).
- [3] R. A. Ganeev, High-Order Harmonic Generation in Laser Plasma Plumes (World Scientific, 2013).
- [4] T. Ozaki, R. A. Ganeev, M. Suzuki, and H. Kuroda, in (In Tech, 2010).
- [5] R. A. Ganeev, M. Suzuki, and H. Kuroda, Phys. Rev. A. **89**, 033821 (2014).
- [6] V. Strelkov, Phys. Rev. Lett. **104**, 123901 (2010).
- [7] L. B. Elouga Bom, Y. Pertot, V. R. Bhardwaj, and T. Ozaki, Opt. Express **19**, 3077 (2011).
- [8] M. Lewenstein, Ph. Balcou, M. Yu. Ivanov, Anne L’Huillier, and P.B. Corkum, Phys. Rev. A **49**, 2117 (1994).
- [9] P. Corkum, Phys. Rev. Lett. **71**, 1994 (1993).
- [10] C. Winterfeldt, C. Spielmann, and G. Gerber, Rev. Mod. Phys. **80**, 117 (2008).
- [11] R. A. Ganeev, L. B. Elouga Bom, J. C. Kieffer, M. Suzuki, H. Kuroda, and T. Ozaki, Phys. Rev. A **76**, 023831 (2007).
- [12] T. Popmintchev, M.-C. Chen, D. Popmintchev, P. Arpin, S. Brown, S. Alisauskas, G. Andriukaitis, T. Balciunas, O. D. Mücke, A. Pugzlys, A. Baltuska, B. Shim, S. E. Schrauth, A. Gaeta, C. Hernández-García, L. Plaja, A. Becker, A. Jaron-Becker, M. M. Murnane, and H. C. Kapteyn, Science **336**, 1287 (2012).
- [13] Z. Chang, A. Rundquist, H. Wang, M. Murnane, and H. Kapteyn, Phys. Rev. Lett. **79**, 2967 (1997).
- [14] B. Shan and Z. Chang, Phys. Rev. A **65**, 011804 (2001).
- [15] T. Popmintchev, M.-C. Chen, P. Arpin, M. M. Murnane, and H. C. Kapteyn, Nat. Photonics **4**, 822 (2010).
- [16] M. V. Frolov, N. L. Manakov, and A. F. Starace, Phys. Rev. Lett. **100**, 173001 (2008).
- [17] A. Shiner, C. Trallero-Herrero, N. Kajumba, H.-C. Bandulet, D. Comtois, F. Légaré, M. Giguère, J.-C. Kieffer, P. Corkum, and D. Villeneuve, Phys. Rev. Lett. **103**, 073902 (2009).
- [18] D. Gaudiosi, B. Reagan, T. Popmintchev, M. Grisham, M. Berrill, O. Cohen, B. Walker, M. Murnane, H. Kapteyn, and J. Rocca, Phys. Rev. Lett. **96**, 203001 (2006).
- [19] A. D. Shiner, B. E. Schmidt, C. Trallero-Herrero, H. J. Wörner, S. Patchkovskii, P. B. Corkum, J. C. Kieffer, F. Légaré, and D. M. Villeneuve, Nat. Phys. **7**, 464 (2011).
- [20] J. Costello, E. Kennedy, B. Sonntag, and C. Clark, Phys. Rev. A **43**, 1441 (1991).
- [21] D. Becker and U. Shirley, VUV and Soft X-Ray Photoionization (1996).
- [22] V. K. Dolmatov and S. T. Manson, J. Phys. B At. Mol. Opt. Phys. **31**, 999 (1998).
- [23] M. Martins, K. Godehusen, T. Richter, P. Wernet, and P. Zimmermann, J. Phys. B At. Mol. Opt. Phys. **39**, R79 (2006).
- [24] C. Butth, F. He, J. Ullrich, C. H. Keitel, and K. Z. Hatsagortsyan, Phys. Rev. A **88**, 033848 (2013).
- [25] C. Butth, M. C. Kohler, J. Ullrich, and C. H. Keitel, Opt. Lett. **36**, 3530 (2011).
- [26] M. Kutzner, V. Radojevic, and H. P. Kelly, Phys. Rev. A **40**, 5042 (1989).
- [27] D. L. Ederer, Phys. Rev. Lett. **13**, 760 (1964).

- [28] M. Suzuki, M. Baba, R. A. Ganeev, H. Kuroda, and T. Ozaki, Opt. Lett. **31**, 3306 (2006).
- [29] J. W. Cooper, C. W. Clark, C. L. Cromer, and T. B. Lucatorto, Phys. Rev. A **39**, 6074 (1989).
- [30] A. T. Le, R. R. Lucchese, S. Tonzani, T. Morishita, and C. D. Lin, Phys. Rev. A. **80**, 013401 (2009).
- [31] http://henke.lbl.gov/optical_constants/asf.html.

Chapter 5

Carbon Molecules for Intense High-order Harmonics from Laser-ablated Graphite Plume

Summary

High-order harmonics of multi- μ J energy are generated from laser-ablated graphite plume. Up to now, the physical reasons involved behind these intense harmonics were uncertain and lacked information of ablated species from laser produced graphite plume contributing to HHG. In this chapter, we collect information about carbon species that are ablated from graphite and investigate their role in HHG. Information on the carbon species are collected with plasma emission spectroscopy and our results show that, within the laser-ablation parameters used for efficient HHG, graphite plume contain an abundance of diatomic carbon molecules (C_2). The contribution of these molecules (along with that of monoatomic carbon) to HHG is studied by comparing the harmonic spectra with their PICS and a good agreement is found between them. However, the PICS of monoatomic carbon is low in the soft X-ray region, and also deviates considerably from the harmonic spectra. These observations are strong evidence that in graphite plume, diatomic molecules of carbon are the key species for intense HHG from graphite plume.

5.1 High-order Harmonics from Laser-ablated Graphite Plume

During the last decade, the development of the coherent source of ultrafast XUV, based on LAP have been advanced rapidly [1–5]. This is a promising technique to develop a tabletop HHG source with high-photon flux [6–9]. With this technique, wide range of solid materials have been used for HHG, and their nonlinear properties in the XUV region have been studied [4,10].

One intriguing characteristic of the LAP technique is that for some target materials, the efficiency of the single high-order harmonic is high [11]. For example, in harmonics from In^+ , the intensity of the RH at ~ 20 eV is about two orders of magnitude higher than the harmonic intensity generated with the conventional three-step process [4]. This is because the resonant states are involved in RH generation (details given in chapter 3). From LAP, the most intense harmonics have been observed from carbon plumes. It has been observed that the intensity of each harmonic from carbon plume is comparable or even higher than that of RH [11]. Our group has demonstrated that high-order harmonics with multi- μ J energy are generated from the carbon

LAP [6]. To better understand the efficiencies of harmonics following different mechanism of HHG, a comparison of harmonic spectra (with maximum observed intensity) generated from Mg, In⁺ and graphite plums is shown in **Fig. 5.1**.

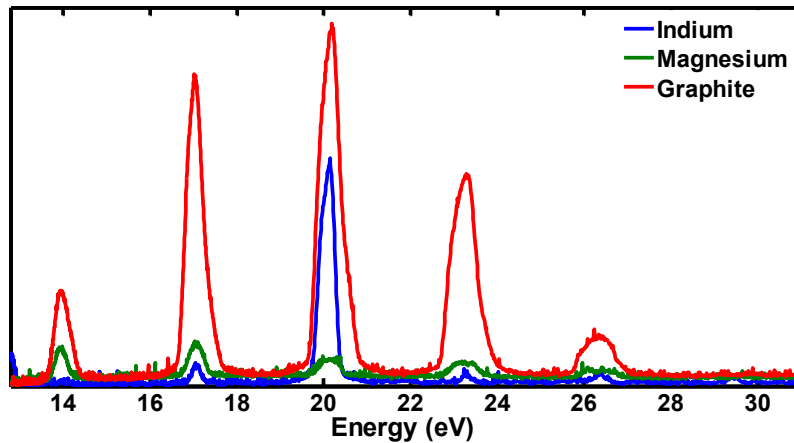


Figure 5.1: High-order harmonic spectra generated from laser-ablated In⁺ (blue), Mg (green) and carbon plume (red).

Fig. 5.1 shows the high-order harmonic spectra from In⁺, Mg and carbon plumes. We selected these elements, since the HHG mechanism is different for each of these materials. In Mg, high-order harmonics are generated with the conventional three-step process. Indium's spectrum contains RH at ~20 eV, which follows the four-step process for harmonic emission (details are given in chapter 3). The mechanism involved in HHG from carbon plume is one of the objectives of this thesis and will be described later.

High-order harmonics from Mg are observed to be weak compared to the other two. This is because of the low recombination rate of electrons following the three-step process for HHG [3]. The high-order harmonic spectrum of In⁺ shows that the intensity of a specific harmonic, located at ~20.15 eV is high, compared to the neighboring harmonic intensity, or the harmonics from Mg, where harmonics are generated with the conventional three-step process. This increase in RH intensity at ~20.15 eV is because of the perturbation by the 4d¹⁰5s² 1S₀ - 4d⁹5s²5p (2D) 1P₁ resonance [4]. High-order harmonics from carbon plume are intense. Comparison between the RH and the carbon harmonics indicate that the intensity of each carbon harmonic is comparable or even higher than the RH intensity.

The high intensity of the carbon harmonics shows that carbon LAP is a promising medium to generate bright tabletop sources of coherent XUV radiation, and is an excellent element to generate intense attosecond pulses, which would allow one to explore new frontiers in science, such as the control of atomic motion in real time [12], attosecond time resolved dynamics of atoms, molecules [13], solids [14] and also the high contrast imaging of biological molecules in the water window region [15,16].

However, the laser-ablated carbon species that is responsible for intense HHG are unknown. This is a big barrier to understand the reasons why harmonics from carbon plumes are intense. To better understand the physics behind intense HHG from carbon LAP, first we identify the carbon species that are responsible for the HHG. This is especially important in LAP harmonics, where the composition of the plume is complex, typically involving not just atoms and ions, but also larger molecules and even clusters [17,18].

5.2 Time Resolved Laser-induced Breakdown Spectroscopy

Time-resolved laser-induced breakdown spectroscopy (TR-LIBS) is used to study the carbon species that are present in the graphite plume. In graphite plume, there is a possibility that we ablate different types of carbon species [19–21]. To clarify the carbon species that are responsible for the intense HHG from graphite LAP, we also perform simultaneous measurements of plasma emission spectroscopy and HHG from the laser-ablated graphite plume. From the TR-LIBS, we optimize HHG within the plasma region, at a time and position where visible plasma emission is most intense. Information on the carbon species within the graphite plume are collected by observing the visible plasma emission lines, and their relevance to HHG is confirmed by comparing the high-order harmonic spectra with the PICS of each possible carbon species.

Plasma emission is recorded with the TR-LIBS spectrometer (Newport, MS260i) and the spectral emission lines are shown in **Fig. 5.2** at 30 ns of time period from the start of ablation (t_{sa}). The visible spectral region of 410 nm to 580 nm wavelength is selected for this measurement, as this region contains the dominant emission transitions of monoatomic carbon and molecules [17,22]. In this specified region, strong spectral emissions of the Swan bands are observed, which are

signatures of diatomic molecules of carbon (C_2) [18]. In this spectrum, the observed adjacent bands are associated with the $d^3\Pi_g \rightarrow a^3\Pi_u$ transitions, which belongs to the vibrational progressions of $\Delta v = 0, \pm 1$ and $+2$ bands. The peaks of the bands, (2,0), (1,0), (0,0) and (0,1) are observed at 436, 473, 516 and 563 nm wavelengths, respectively. We have also observed very weak transitions of the (0,2) band (not shown in the figure), with a peak at 619 nm wavelength. From this spectrum, it is evident that the graphite plasma plume contains an abundance of C_2 molecules.

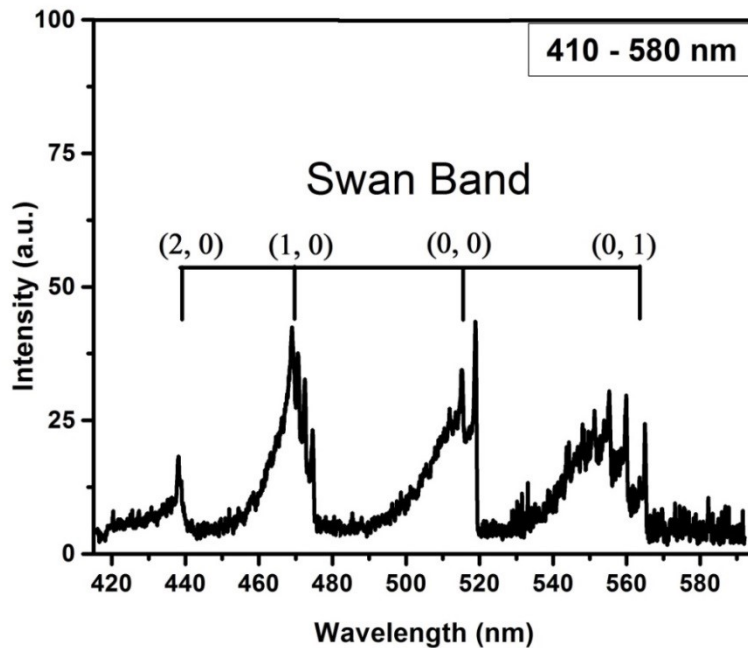


Figure 5.2: The spectrum of graphite plasma emission, showing predominantly vibronic transitions of carbon molecules (C_2). The spectral region is selected from 410 nm to 580 nm, and this spectrum is recorded at $t_{sa} = 30$ ns.

Interestingly, we could not observe any signature of neutral or ionic transitions of monoatomic carbon in our visible emission, which is contrary to what is usually observed in other materials using nanosecond or femtosecond laser ablation [17,18]. We have observed that, for the PP laser parameters used in this work with the graphite target (pulse duration ~ 210 picoseconds, central wavelength at $0.8 \mu\text{m}$ and intensity $\sim 10^{10} \text{ Wcm}^{-2}$), the ablated plume emits strong radiation related to molecular bands, such as C_2 . This is in sharp contrast to past LAP harmonics, where mostly monoatomic particles from low-density LAP have been used for HHG [4,10]. Another technique of harmonic generation, similar to LAP technique, is the harmonic generation with

gases [15,23]. In gas harmonics, several types of diatomic molecules have been used for HHG and very interesting features have been observed [24–26]. However, to the best of our knowledge, no diatomic response for HHG has been observed previously with the LAP technique. Therefore, HHG from graphite LAP is a first molecular medium that can be used to study molecular dynamics of HHG from solid materials.

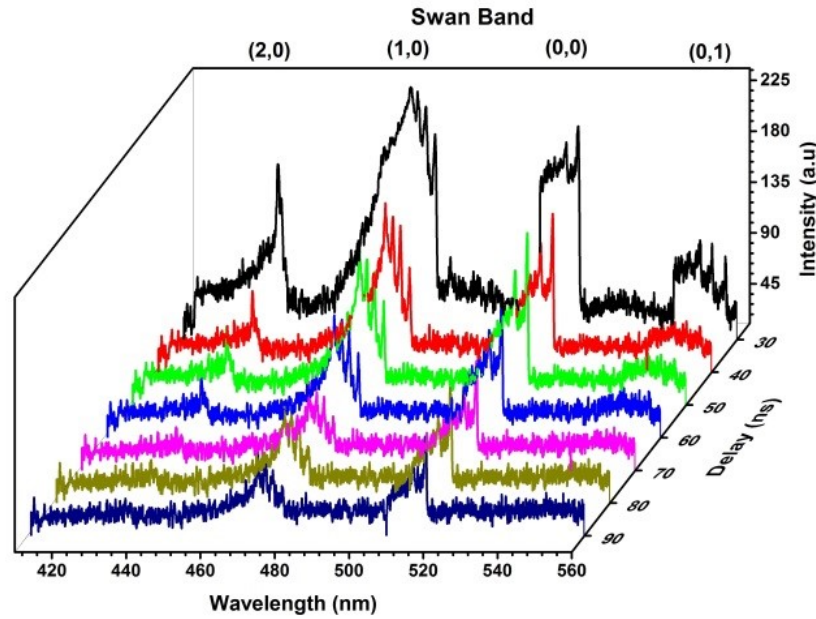


Figure 5.3: Variation of the Swan bands for t_{sa} of 30 to 90 ns, in the spectral region between 410 nm to 560 nm, at a fixed PP laser intensity of $3.0 \times 10^{10} \text{ Wcm}^{-2}$.

The temporal variation in the intensity of the plasma emission around the Swan band is recorded for different t_{sa} . The spectral region from 410 nm to 560 nm is selected for these measurements. After ablation, plasma emission is recorded for t_{sa} of 30 ns to 90 ns, at a fixed laser intensity of $3.0 \times 10^{10} \text{ Wcm}^{-2}$, shown in **Fig. 5.3**. It has been shown that such plasma spectroscopy technique is useful to find the optimum conditions for intense HHG from solid materials [27]. From this figure, we see that the intensity of the Swan band emission is high at 30 ns, which decreases rapidly as the plasma expands. The emission of the Swan band almost disappears after $t_{sa} = 90$ ns. This observation suggests that within the specified plasma emission region of 30 ns to 90 ns, C_2 molecules are abundant around 30 ns and disappear at 90 ns.

To compare the intensity variation of C₂ observed in **Fig. 5.3**, we study the variation of the harmonic intensity with the delay between the PP and the MP. With this delay variation, we will be able to find the delay time at which the harmonic intensity is maximum. It should be noted that along with the delay time between the PP and the MP, the intensity of the PP is also a crucial parameter for maximizing the harmonic output flux, as this intensity is used to control the density of the ablated plume. For graphite LAP, the optimum PP intensity for efficient HHG is $\sim 1.4 \times 10^{10} \text{ Wcm}^{-2}$. At higher intensities, we start to observe spectral line emission of monoatomic carbon in the visible region, accompanied by a significant reduction in the harmonic intensity. Similarly, low PP intensities (discussed below) also reduce the photon flux of the XUV pulses. To better understand the tradeoff between the PP intensity and PP-to-MP delay, we use two different PP laser intensities near the optimum to produce the graphite LAP, and then we vary the delay between the PP and the MP.

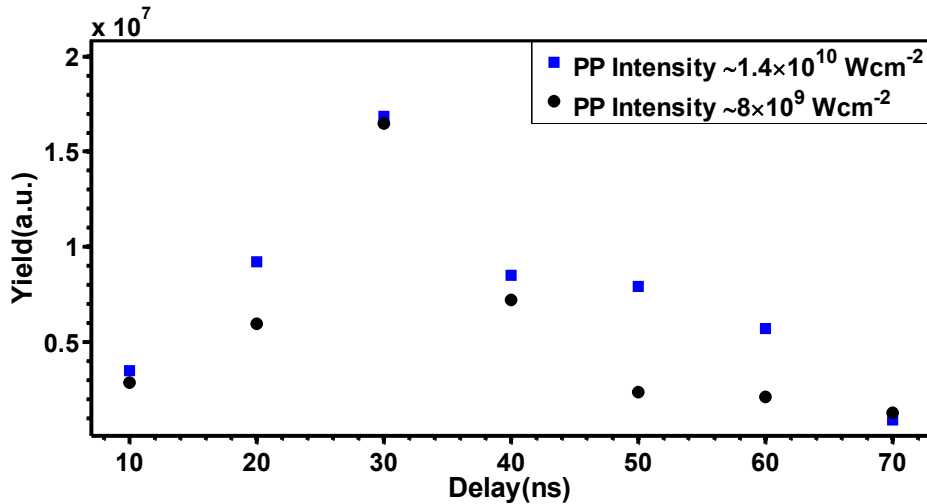


Figure 5.4: Variation of high-order harmonic yield with respect to the delay between the PP and MP at two different PP ablation intensities of $\sim 1.4 \times 10^{10} \text{ Wcm}^{-2}$ (blue squares) and $\sim 8 \times 10^9 \text{ Wcm}^{-2}$ (black circles) using main pulse intensity of $\sim 2.5 \times 10^{14} \text{ Wcm}^{-2}$.

The variation of the harmonic yield for a PP-to-MP delay from 10 ns to 70 ns is shown in **Fig 5.4**. In this measurement, the intensity of the MP is kept constant at $\sim 2.5 \times 10^{14} \text{ Wcm}^{-2}$. It is observed that at a PP intensity of $1.4 \times 10^{10} \text{ Wcm}^{-2}$, very weak harmonic signal starts to appear on the MCP for delays as short as 2 ns. As the delay is increased, we observe that harmonic signal of sufficient yield is observed from 10 ns delay. However, at this relatively short delay, the

background noise due to plasma emission is high, since the plasma temperature during the initial stage of ablation is generally high. Results show that XUV harmonics with highest yield is generated at 30 ns delay. After that, the high-order harmonic yield decrease as the delay is increased, and almost vanishes after a delay of 70 ns.

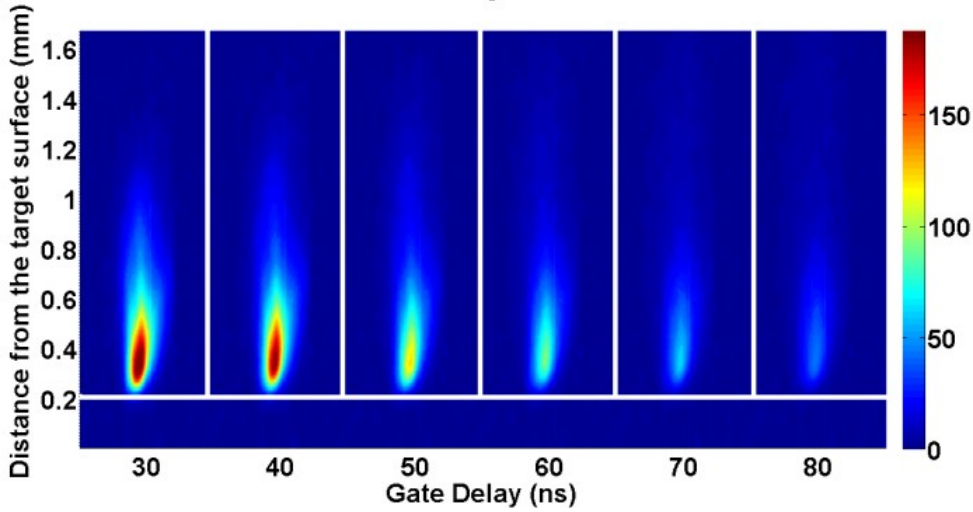


Figure 5.5: Spectrally integrated images of carbon plasma plume expansion at variable time periods of plasma evaluation, at fix prepulse laser intensity of $3.0 \times 10^{10} \text{ Wcm}^{-2}$.

Further, the spectrally integrated images of the plasma at variable t_{sa} are recorded, as shown in **Fig. 5.5**. These images are recorded to check the plume size and its emission dynamics at different t_{sa} , by imaging the plasma directly on to the ICCD Camera (iStar 720; bypassing the grating), where the CCD of this camera is capable of detecting the spectral emission from 120 nm to 1090 nm. This figure shows that the vertical extension of the plasma plume is ~ 1 mm from the target surface. Plasma emission is observed to be strong at positions close to the target surface, because of the higher density in this region. The variation of the plasma intensity at different t_{sa} shows that this emission intensity decreases rapidly at large t_{sa} , which reveals that the density of the medium is higher at shorter delays. Finally, the emission of the plume vanishes after $t_{sa} = 80$ ns. These observations show strong correlation between the intensity of the Swan band emission (**Fig. 5.3**) and harmonic yield (**Fig. 5.4**), pointing to the contribution of C_2 molecules for intense harmonic generation from graphite LAP.

5.3 Comparison between the High-order Harmonic Spectrum and the Photo-ionization Cross-section

To further study the contribution of C₂ molecules to graphite HHG, we compare the PICS of C₂ with the graphite harmonic spectra. According to QRS theory for high-order harmonics, the harmonic spectra from a single atom or molecule should replicate the field-free PICS of the atom or molecule [28]. Mathematically, HHG spectra for an extended system can be written as

$$S_h(\omega) \propto |W(\omega)|^2 \sigma^R(\omega) \quad (5.1)$$

Here, $W(\omega)$ is the macroscopic wave packet (MWP), and $\sigma^R(\omega)$ is the photo-recombination cross section, which is the inverse conjugate of the PICS. The macroscopic wave packet $W(\omega)$ depends on the system and includes phase matching condition, and differs from the single atom wave packet only by the phase matching condition. For harmonic generation in thin medium (such as in our case, where the plume is 100 - 200 μm in width), the phase mismatch tolerances are broader and it reduces the impact of the phase matching influence on the wave packet. In this case, the harmonic spectrum should follow closely the PICS of the medium.

Several methods can be used to calculate the PICS [29–32]. We use Hartee-Fock Approximation (HFA) to compare the high-order harmonic spectra with the PICS of monoatomic and diatomic carbon, to identify the contribution of both elements to HHG. The details of the calculation of the PICS used here can be found elsewhere [29]. In HFA, the equation for PICS can be written as,

$$d\sigma^i/d\Omega = \sigma^i/4\pi[1 + \beta P_2(\cos(\theta))] \quad (5.2)$$

Here σ^i is the total ionization cross-section, β is the asymmetry parameter, $P_2(\cos(\theta))$ is an associated Legendre polynomial ($3/2\cos(\theta) - 1/2$) and θ is the angle between the direction of polarization of light and the momentum of the outgoing electron. For HHG, the polarization of the generated harmonics is parallel to the re-colliding electron, so the $\theta=0$ contribution is considered. The values of the total ionization cross-section σ^i and asymmetry parameters (β) are given in **Table 5.1**, at certain energies.

Table 5.1: The parameters, σ_i (Mb) and β (asymmetry parameter) used for the calculation of photoionization cross-section, collected from ref. [28,29].

Monoatomic Carbon														
Energy (eV)	16.7	20.0	21.2	25.0	26.8	30.0	35.0	40.0	40.8	45.0	50.0	55.0	60.0	
σ^i (Mb)	8.28	6.63	6.12	4.8	4.29	3.52	2.62	1.97	1.88	1.5	1.16	0.91	0.72	
B	1.16	1.28	1.31	1.38	1.41	1.44	1.48	1.5	1.51	1.52	1.52	1.52	1.52	
Diatomeric Carbon (C_2)														
Energy (eV)	14.5	15.0	17.5	20.0	22.5	25.0	27.5	30.0	32.5	35.0	37.5	40.0	45.0	50.0
σ^i (Mb)	51.3	51.1	42.3	28.7	18.9	13.0	9.54	7.43	6.05	5.06	4.29	3.67	2.73	2.1
B	0.71	0.77	0.94	1.01	1.07	1.14	1.21	1.28	1.35	1.42	1.47	1.52	1.59	1.64

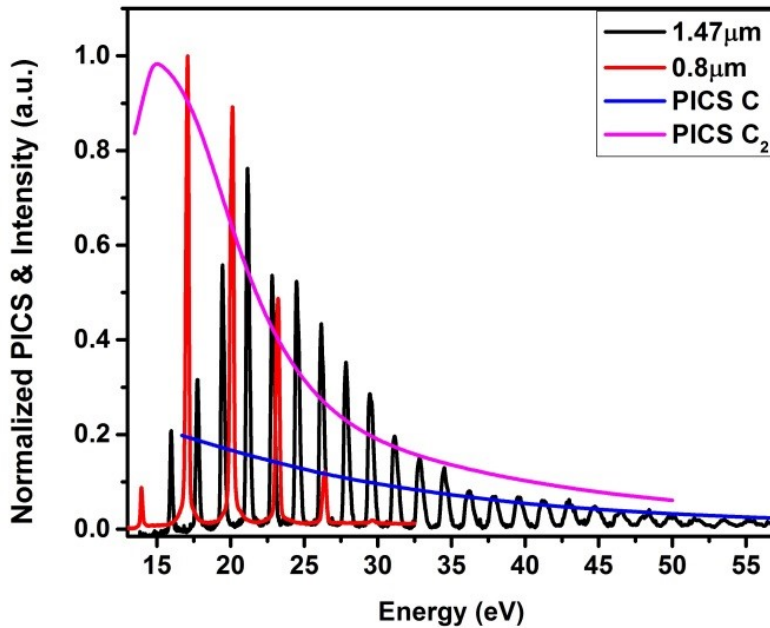


Figure 5.6: Comparison of the high-order harmonic spectra, generated with two different driving laser wavelengths of $0.8 \mu\text{m}$ and $1.47 \mu\text{m}$, and photo-ionization cross-section is presented, for carbon species C and C_2 .

A comparison of the PICS with the high-order harmonic spectra is shown in **Fig 5.6**. We can see that the PICS for diatomic carbon is higher compared to neutral carbon. By comparing with the

HHG spectra generated using 0.8 μm laser (red curve), we find that the wavelength dependence of the PICS for C_2 is in better agreement with the harmonic spectra than for monoatomic carbon. However, the cutoff of the harmonics from graphite plume with the 0.8 μm driving laser is limited to around 30 eV. To compare the PICS with harmonics at higher energies, high-order harmonics are generated using 1.47 μm wavelength driving laser. Again, we find good agreement between the harmonics and the PICS of C_2 when driving laser pulses of 1.47 μm wavelength are used (black curve). In addition to the Swan bands observed in **Fig. 5.2**, this observation again supports that harmonics are generated from diatomic carbon molecules, instead of monoatomic carbon.

In **Fig. 5.6**, we have observed that high-order harmonics up to \sim 32 eV are generated from laser-ablated carbon molecules using 0.8 μm wavelength driving lasers. The ionization potential of the C_2 molecule is \sim 11.4 eV and the saturation intensity is estimated to be \sim 3.64 \times 10¹⁴ Wcm⁻². From this ionization potential and saturation intensity, the high-order harmonic spectra in **Fig. 5.6** indicate that harmonics are generated from neutral diatomic carbon molecules.

Conclusion

In conclusion, we have simultaneously studied laser-induced plasma emission spectroscopy and HHG from laser-ablated graphite plume. The evolution of the plasma species that are ablated from solid graphite is investigated in the different time domains of ablation. We find that for the experimental conditions used for material ablation for HHG, the plume has an abundance of diatomic carbon molecules (C_2) instead of monoatomic carbon. The variation of the diatomic molecules is investigated as a function of time after ablation, and harmonics are optimized within the region where neutrals are abundant. It is observed that harmonics with high-efficiency can be generated 30 ns after ablation. Finally, the tendency of the PICS for C and C_2 is compared with the HHG spectra, and good agreement is observed for C_2 , instead of C.

References

- [1] R. A. Ganeev, M. Suzuki, M. Baba, H. Kuroda, and T. Ozaki, Opt. Lett. **30**, 768 (2005).
- [2] R. A. Ganeev, M. Suzuki, M. Baba, H. Kuroda, and T. Ozaki, Opt. Lett. **31**, 1699 (2006).
- [3] P. Corkum, Phys. Rev. Lett. **71**, 1994 (1993).
- [4] T. Ozaki, R. A. Ganeev, M. Suzuki, and H. Kuroda, in (In Tech, 2010).
- [5] R. A. Ganeev, Nonlinear Optical Properties of Materials (2013).
- [6] L. B. Elouga Bom, Y. Pertot, V. R. Bhardwaj, and T. Ozaki, Opt. Express **19**, 3077 (2011).
- [7] R. A. Ganeev, L. B. Elouga Bom, J. Abdul-Hadi, M. Wong, J. Brichta, V. Bhardwaj, and T. Ozaki, Phys. Rev. Lett. **102**, 013903 (2009).
- [8] V. Strelkov, Phys. Rev. Lett. **104**, 123901 (2010).
- [9] R. A. Ganeev, L. Elouga Bom, M. Wong, J.-P. Brichta, V. Bhardwaj, P. Redkin, and T. Ozaki, Phys. Rev. A **80**, 043808 (2009).
- [10] R. A. Ganeev, High-Order Harmonic Generation in Laser Plasma Plumes (World Scientific, 2013).
- [11] R. A. Ganeev, T. Witting, C. Hutchison, F. Frank, P. V. Redkin, W. A. Okell, D. Y. Lei, T. Roschuk, S. A. Maier, J. P. Marangos, and J. W. G. Tisch, Phys. Rev. A **85**, 015807 (2012).
- [12] P. Corkum and F. Krausz, Nat. Phys. **3**, 381 (2007).
- [13] F. Krausz and M. Ivanov, Rev. Mod. Phys. **81**, 163 (2009).
- [14] S. Ghimire, A. D. DiChiara, E. Sistrunk, P. Agostini, L. F. DiMauro, and D. A. Reis, Nat. Phys. **7**, 138 (2010).
- [15] T. Popmintchev, M.-C. Chen, D. Popmintchev, P. Arpin, S. Brown, S. Alisauskas, G. Andriukaitis, T. Balciunas, O. D. Mücke, A. Pugzlys, A. Baltuska, B. Shim, S. E. Schrauth, A. Gaeta, C. Hernández-García, L. Plaja, A. Becker, A. Jaron-Becker, M. M. Murnane, and H. C. Kapteyn, Science **336**, 1287 (2012).
- [16] Z. Chang, A. Rundquist, H. Wang, M. Murnane, and H. Kapteyn, Phys. Rev. Lett. **79**, 2967 (1997).
- [17] K. F. Al-Shboul, S. S. Harilal, and A. Hassanein, J. Appl. Phys. **113**, 163305 (2013).
- [18] Y. Yamagata, A. Sharma, J. Narayan, R. M. Mayo, J. W. Newman, and K. Ebihara, J. Appl. Phys. **86**, 4154 (1999).
- [19] L. Nemes, A. M. Keszler, C. G. Parigger, J. O. Hornkohl, H. A. Michelsen, and V. Stakhursky, Appl. Opt. **46**, 4032 (2007).
- [20] S. S. Harilal, A. Hassanein, and M. Polek, J. Appl. Phys. **110**, 053301 (2011).
- [21] S. J. Henley, J. D. Carey, S. R. P. Silva, G. M. Fuge, M. N. R. Ashfold, and D. Anglos, Phys. Rev. B **72**, 205413 (2005).
- [22] Y. Yamagata, A. Sharma, J. Narayan, R. M. Mayo, J. W. Newman, and K. Ebihara, J. Appl. Phys. **88**, 6861 (2000).
- [23] C. Winterfeldt, C. Spielmann, and G. Gerber, Rev. Mod. Phys. **80**, 117 (2008).
- [24] R. Velotta, N. Hay, M. B. Mason, M. Castillejo, and J. P. Marangos, Phys. Rev. Lett. **87**, 183901 (2001).
- [25] L. Holmegaard, J. H. Nielsen, I. Nevo, and H. Stapelfeldt, Phys. Rev. Lett. **102**, 023001 (2009).
- [26] X.-B. Bian and A. D. Bandrauk, Phys. Rev. Lett. **113**, 193901 (2014).

- [27] R. A. Ganeev, L. B. Elouga Bom, and T. Ozaki, Phys. Plasmas **18**, 083101 (2011).
- [28] A. T. Le, R. R. Lucchese, S. Tonzani, T. Morishita, and C. D. Lin, Phys. Rev. A. **80**, 013401 (2009).
- [29] Z. Chang, Fundamentals of Attosecond Optics (CRC Press, 2011).
- [30] J. J. Yeh and I. Lindau, At. Data Nucl. Data Tables **32**, 1 (1985).

Chapter 6

Properties of High-order Harmonics Generated from Diatomic Carbon Molecules

Summary

In this chapter, we study the properties of high-order harmonics generated from diatomic carbon molecules. There are three major results presented in this chapter. In the first step, three graphite targets with carbon compositions of 91, 97 and 99.9 percent are used for HHG and harmonics with similar intensity are observed with the 0.8 μm driving lasers. This shows that impurities in the graphite plumes have less perturbation to affect the harmonic efficiency. Therefore, graphite with 91% of carbon composition is found as an economical target material for intense HHG.

High-order harmonic cutoff from diatomic carbon is observed to be relatively low (~ 32 eV), when driven with 0.8 μm driving lasers. This cutoff is extended by increasing the driving laser wavelength from 0.8 μm to 1.71 μm . The higher-order harmonic spectra reveal that by changing driving laser wavelength from 0.8 μm to 1.71 μm , high-order harmonic intensity reduces by only about 30%.

Finally, we have observed that high-order harmonics from laser-ablated carbon molecules contain strong redshift. This redshift is observed to be continuous in nature and increases linearly with the driving laser intensity. Recent theoretical studies predict that this redshift in harmonics could appear when resonant-excited states contribute in HHG or it may appear due to molecular dissociation, during HHG. We perform different experiments to investigate the actual mechanism involved behind this redshift.

6.1 Introduction

In most of the laser-ablated media used for HHG, high-order harmonics are generated from monoatomic particles [1,2]. The contribution of diatomic carbon molecules in HHG from laser-ablated graphite plume has been observed for the first time (details are given in chapter 5). In past, high-order harmonic properties of diatomic molecules have been extensively studied with gaseous media [3–5]. But now, with laser-ablation technique, we can study the properties of molecules that are not available in gaseous form. In the field of laser-ablation spectroscopy, the information about the laser-ablated species is collected from plasma emissions [6,7]. These

spectroscopic studies show that different types of diatomic molecules can be ablated from solid surfaces [8–10]. Therefore, the next trend of LAP technique for HHG will be to study the properties of different laser-ablated diatomic molecules.

In this chapter, we investigate the properties of diatomic carbon harmonics. In the first step, we use graphite target with different carbon composition to find an economical target material for intense HHG.

6.2 High-order Harmonics from Laser-ablated Graphite Plumes Containing Different Carbon Composition

High-order harmonics with multi- μJ energy have been generated from carbon molecules. These carbon molecules are ablated from graphite targets having carbon purity $\sim 99.9\%$. The graphite targets with high purity are very expensive, as these materials are refined with different purification processes. Most recently, our group has demonstrated that the pencil lead can be used as an inexpensive source of HHG [11]. However, in pencil lead, carbon concentration was found to vary between about 23% to 47% at different ablation positions. This shows that the carbon concentration is inhomogeneous in the pencil lead plume and it can fluctuate the shot to shot stability of the XUV pulses. To generate stable XUV pulses and make carbon target cost efficient, we use graphite with different carbon compositions ranging from 91% to 99.99% for the plume ablation. High-order harmonic spectra generated from three graphite targets having carbon composition of 99.9, 97.0 and 91.0 % are given in the following figure.

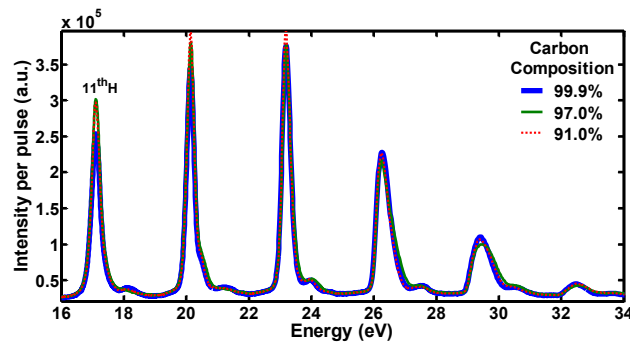


Figure 6.1: High-order harmonic spectra generated using $0.8 \mu\text{m}$ driving laser from three laser-ablated graphite plumes with carbon composition of 91.0, 97.0 and 99.9 %. High-order harmonics of similar yield and cutoff are generated from these plumes. These spectra are recorded with MP intensity of $\sim 2.73 \times 10^{14} \text{ Wcm}^{-2}$.

Fig. 6.1 shows the high-order harmonic spectra generated with 0.8 μm driving laser from three graphite targets having carbon composition of 99.9% (Green; Alfa-Aesar), 97.0% (Red) and 91.0% (Blue; McMaster-Carr, Graphite-91). In Graphite-91, the impurity is mostly 9% of oxygen that is observed with the energy dispersive X-ray spectroscopy (EDS) technique. The laser parameters, especially the PP and the MP intensities ($\sim 1.2 \times 10^{10} \text{ Wcm}^{-2}$ and $\sim 2.73 \times 10^{14} \text{ Wcm}^{-2}$, respectively), are kept constant to allow accurate comparison of the harmonic properties. It is observed that high-order harmonics of similar yield and cutoff are generated from these three targets. The yield per pulse observed from targets containing 99.9%, 97.0% and 91.0% of carbon are 4.8×10^7 , 5.1×10^7 and 5.0×10^7 (arb. units) respectively, and the maximum high-order harmonic cutoff is observed at ~ 32 eV. The results shown in **Fig. 6.1** indicate that impurities in Graphite-91 have no effects on the harmonic efficiency. Therefore, Graphite-91 is found to be an inexpensive material that can be used for tabletop HHG source with LAP technique.

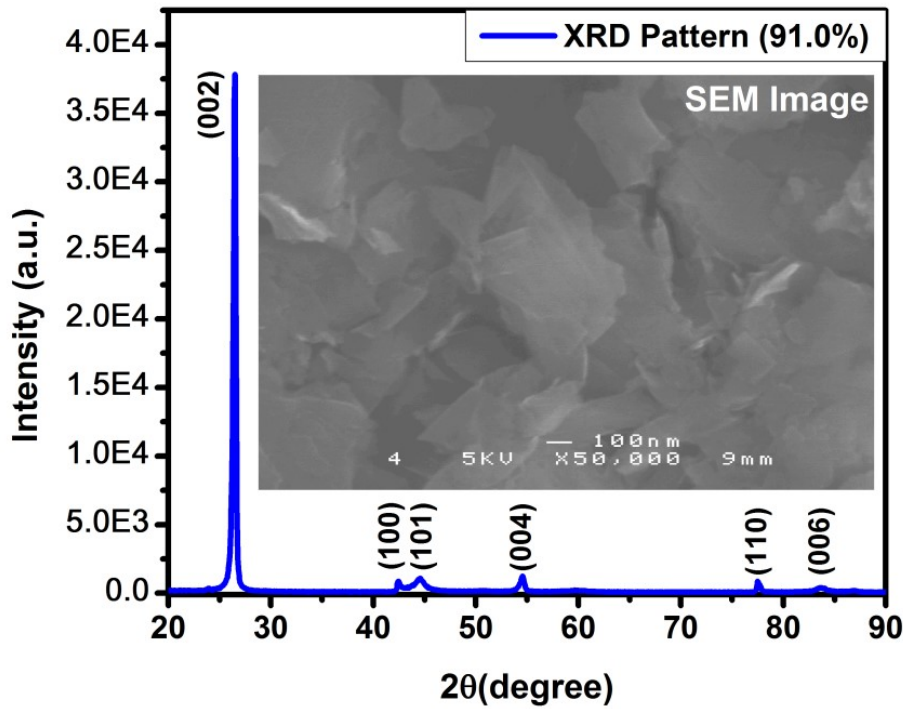


Figure 6.2: XRD pattern and SEM image of Graphite-91 target. The XRD pattern shows that this target has neutral graphite structure, and the SEM image gives the graphite grain size, which is about $\sim 200\text{-}500$ nm.

The industrial Graphite-91 target is prepared by pressing small graphite grains at very high pressure and is used as heat-resistance material at high temperatures. We use EDS, X-ray

diffraction (XRD) and scanning electron microscope (SEM) analysis to characterize this material. The EDS results (not shown here) reveal that this material contains 91% of carbon and oxygen is observed as an impurity. The XRD pattern, shown in **Fig. 6.2**, shows six XRD peaks at (002), (100), (101), (004), (110) and (006), which confirms the graphitic nature of the target after compression. Further, the grain size of this target is estimated with the high-resolution SEM image, shown in **Fig. 6.2(b)**, which indicates that the Graphite-91 is a composite of graphite grains with sizes around 200-500 nm.

6.3 Wavelength Scaling of High-order Harmonics

The high-order harmonics from laser-ablated graphite plume contains multi- μ J of energy [14], when driven with 0.8 μ m driving lasers. However, the high-order harmonic cutoff is observed to be very low (\sim 32 eV; **Fig. 6.1**). This low cutoff limits the applications of this intense XUV source, such as for generating intense attosecond pulses with very short pulse duration [15], and to study the X-ray magnetic dichroism properties [16,17] that require intense soft X-rays of energy 25 eV - 250 eV. We know from the three-step model [18] that HHG cutoff can be extended by increasing the driving laser wavelength. Therefore, we use long-wavelength laser pulses to drive LAP, to extend the harmonic cutoff and high-order harmonic spectra observed at different driving laser wavelengths.

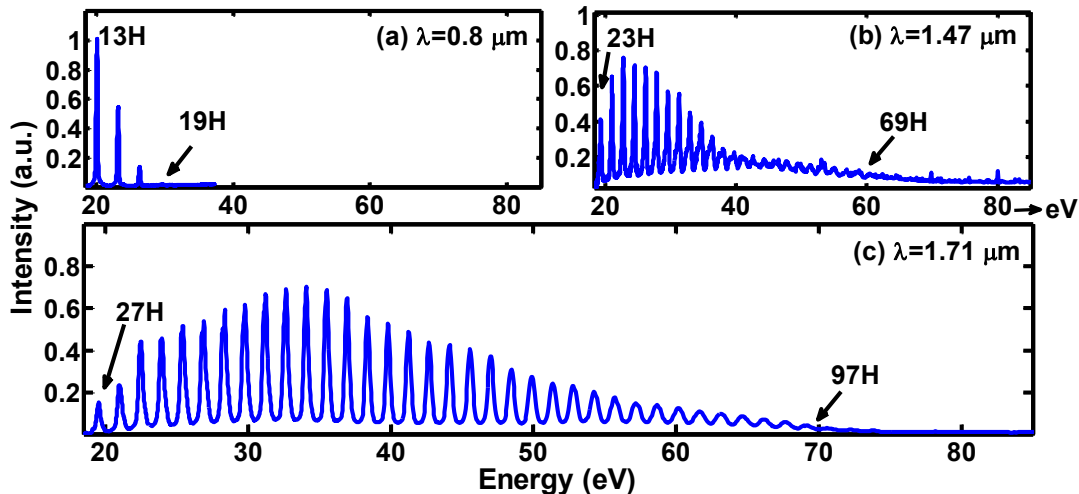


Figure 6.3: High-order harmonic spectra generated from carbon molecules at driving lasers with wavelength (a) 0.8 μ m, (b) 1.47 μ m and (c) 1.71 μ m. These spectra are recorded with laser peak intensity $\sim 1.4 \times 10^{14}$ Wcm $^{-2}$.

Fig. 6.3 shows the high-order harmonic spectra generated from carbon molecules at three driving laser wavelengths, centered at 0.8 μm , 1.47 μm and 1.71 μm . To accurately compare the harmonic intensity, the driving laser intensity for these three wavelengths is maintained at the same value of $\sim 1.4 \times 10^{14} \text{ Wcm}^{-2}$. **Fig. 6.3(a)** shows the high-order harmonic spectrum generated using driving lasers of 0.8 μm wavelength, showing a cutoff of ~ 32 eV. This harmonic cutoff is further extended up to ~ 60 eV by increasing the driving laser wavelength to 1.47 μm , as can be seen in **Fig. 6.3(b)**. The maximum harmonic cutoff is observed with 1.71 μm laser pulses, where we have demonstrated harmonics up to ~ 70 eV (**Fig. 6.3(c)**). In fact, the configuration of our spectrometer limited the detection of harmonics up to this energy, and thus there is a possibility that the actual harmonic cutoff with 1.71 μm laser is even higher than 70 eV.

From **Fig. 6.3**, we also notice that the carbon harmonics are comparable in intensity even when using driving lasers with longer wavelength. In **Fig. 6.3**, the harmonic intensities between the three spectra can be directly compared. Using 0.8 μm driving lasers, our group has already demonstrated that high-order harmonics of multi- μJ energy with efficiencies of 2×10^{-4} for the 13th harmonic are generated from laser-ablated graphite plume [14]. The ratio of the peak harmonic intensity for 0.8 μm , 1.47 μm and 1.71 μm driving lasers is observed to be 1 : 0.76 : 0.70. This indicates that when the driving laser wavelength is changed from 0.8 μm to 1.71 μm , the high-order harmonic peak intensity is reduced by only 30%, for a fixed MP laser intensity of $\sim 1.4 \times 10^{14} \text{ Wcm}^{-2}$ (which is close to the saturation intensity $\sim 3.6 \times 10^{14} \text{ Wcm}^{-2}$). From these results, we can estimate that conversion efficiencies of $> 10^{-4}$ is obtained for carbon harmonics from 25 to 40 eV.

6.4 Tunable Redshift

In HHG, when high-intensity laser pulses interact with the nonlinear medium, the high-order harmonics experience a frequency shift. This frequency shift could be of two types, known as the blue shift and the redshift. Blue shift is commonly observed when high-order harmonics are generated at the rising part of the laser pulse [24]. This blue shift is explained as the change in refractive index [25] due to the ionization of the medium and mainly depends on the medium density and laser pulse intensity [26,27]. The second frequency shift that harmonics could experience is the redshift. This redshift is not common in the high-order harmonics. This redshift

was first reported by Brandi *et al.* [28] in 2006, in the harmonics from Xenon atom. However, in that experiment, the driving lasers of relatively long pulse duration (~ 200 ps) were used for HHG than the normal laser pulses we use for HHG (~ 40 fs). Brandi *et al.* explained that this redshift in Xenon harmonics occurs due to change in refractive index [28].

We have observed that high-order harmonics from diatomic carbon molecules contain a strong redshift. This redshift is found to be continuous in nature and increases linearly with laser pulse intensity. High-order harmonic spectra containing redshift at different laser intensities is shown in the figure given below.

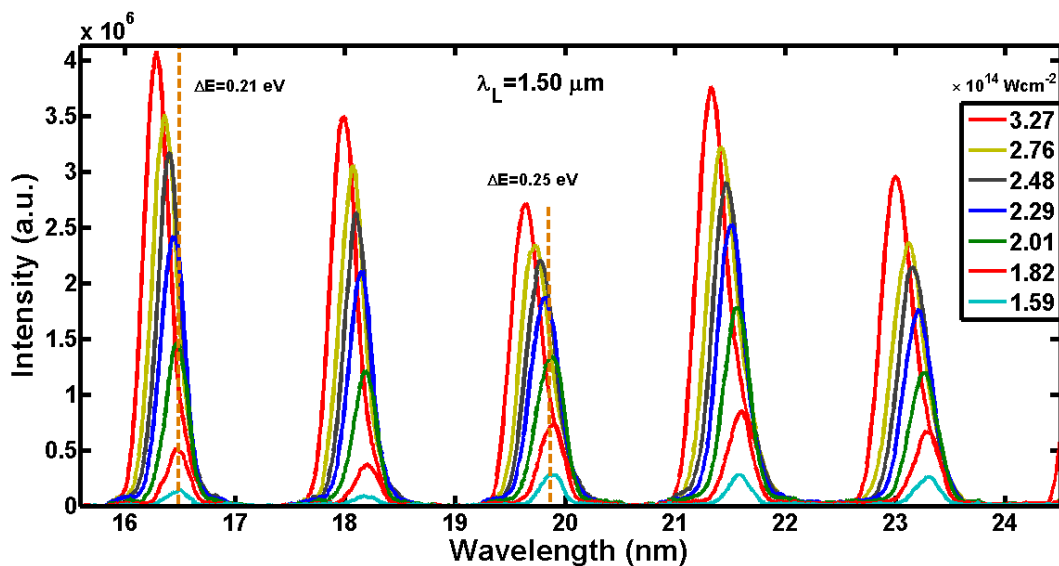


Figure 6.4: High-order harmonic spectra of C_2 , driven with $1.5 \mu\text{m}$ wavelength, at laser intensities from $1.59 \times 10^{14} \text{ Wcm}^{-2}$ to $3.27 \times 10^{14} \text{ Wcm}^{-2}$.

It has been observed that high-order harmonics from diatomic carbon molecules contain strong redshift. This redshift increases continuously when the driving laser intensity is increased from $1.59 \times 10^{14} \text{ Wcm}^{-2}$ to $3.27 \times 10^{14} \text{ Wcm}^{-2}$. These spectra show that within the specified laser intensity, a redshift of 0.25 eV occurs in the high-order harmonics when driven with $1.5 \mu\text{m}$ lasers. In molecular media, this redshift could occur because of three reasons; **(i)** Laser propagation [29], **(ii)** Pre-excitation of the medium at rising part of the laser pulse [30], and **(iii)** Molecular dissociation [5]. The first possibility of laser propagation was introduced by Kim *et al.*, who showed that when laser pulses propagate through a high-density medium (density $\sim 10^{18}$

cm^{-3} ; length ~ 3 mm), these pulses experience a redshift and change the shape [29]. This possibility is uncertain in our case as we are using low-density medium ($\sim 10^{17} \text{ cm}^{-3}$) with reduced dimensions ($\sim 200 \mu\text{m}$ plume width) for HHG. Further, Ganeev *et al.* [31] have also shown that in HHG, when ultrashort driving lasers propagate through the medium, the shape of the laser pulse remains the same.

Therefore, in our next discussion, we will explore the other possibility, which are the involvement of resonant states and molecular dissociation, to find the exact phenomenon involved in producing redshift in the high-order harmonic from carbon molecules.

6.4.1 Role of Resonant-excited States

In 2011, Bian *et al.* [30] predicted redshift in high-order harmonics from polar molecules. He used HeH^{2+} molecules to calculate the high-order harmonic spectra by solving TDSE. In the calculated spectra, he showed that when resonant-excited states with a long lifetime are involved in HHG, a redshift is produced in the harmonic spectrum. According to his model, when resonant-excited states are involved in HHG, the electrons follow the four-step process for HHG, which can be described as,

- i. When laser pulses interact with the molecule, an electron is excited to the bound states with a long lifetime.
- ii. In the second step, this electron is ionized in the continuum from the excited states.
- iii. In the third step, the continuum electron is accelerated by the applied laser field.
- iv. Finally, the electron recombines to the ground state and emits XUV radiation.

As the bound atomic and molecular states are discrete in nature, one way of checking this model is to use tunable driving laser wavelength to see if the resonant-excited states contribute in HHG. At ALLS, we have an OPA that can produce intense, tunable laser pulses ranging from $1.2 \mu\text{m}$ to $2.2 \mu\text{m}$ wavelengths. The complete details of this OPA are given in chapter 2. We use these tunable wavelengths to confirm that either the resonant-excited states of diatomic molecules contribute in HHG or not. The high-order harmonic spectra observed at different laser intensities and at variable driving laser wavelengths are given below.

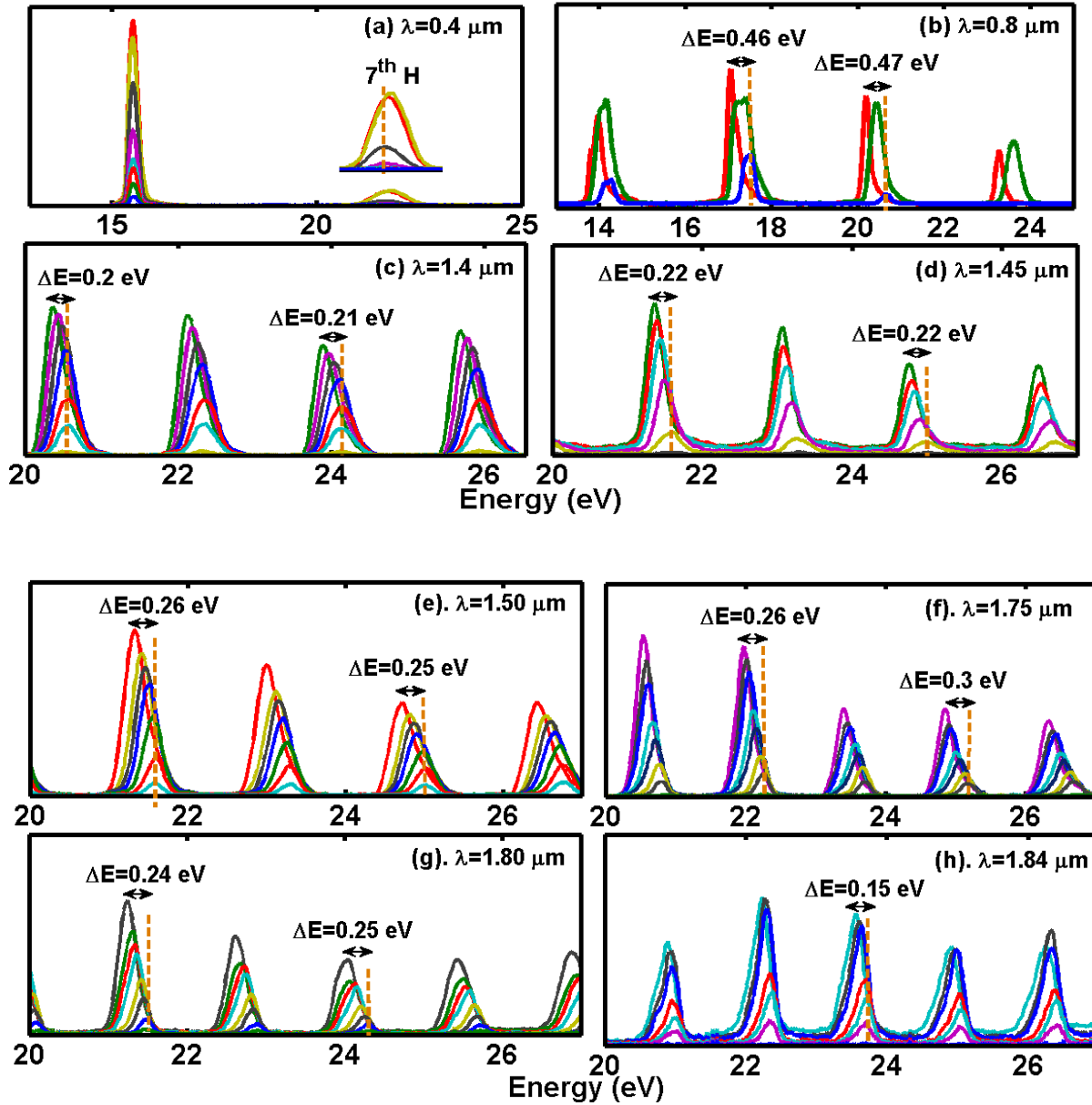


Figure 6.5: Intensity variation of the high-order harmonic spectra, generated from diatomic carbon, at variable driving laser wavelengths. The harmonic spectra generated with laser of (a), $0.4 \mu\text{m}$, at laser intensities from $7.5 \times 10^{13} \text{ Wcm}^{-2}$ to $3.0 \times 10^{14} \text{ Wcm}^{-2}$, (b) $0.8 \mu\text{m}$, at laser intensities from $8.4 \times 10^{13} \text{ Wcm}^{-2}$ to $2.3 \times 10^{14} \text{ Wcm}^{-2}$, (c) $1.4 \mu\text{m}$, at laser intensities from $1.1 \times 10^{14} \text{ Wcm}^{-2}$ to $2.3 \times 10^{14} \text{ Wcm}^{-2}$, (d) $1.45 \mu\text{m}$, at laser intensity from $2.19 \times 10^{14} \text{ Wcm}^{-2}$ to $4.56 \times 10^{14} \text{ Wcm}^{-2}$, (e) $1.5 \mu\text{m}$, at laser intensity from $1.59 \times 10^{14} \text{ Wcm}^{-2}$ to $3.27 \times 10^{14} \text{ Wcm}^{-2}$, (f) $1.75 \mu\text{m}$, at laser intensity from $1.49 \times 10^{14} \text{ Wcm}^{-2}$ to $3.35 \times 10^{14} \text{ Wcm}^{-2}$, (g) $1.8 \mu\text{m}$, at laser intensity from $1.29 \times 10^{14} \text{ Wcm}^{-2}$ to $2.28 \times 10^{14} \text{ Wcm}^{-2}$ and (h) $1.84 \mu\text{m}$, at laser intensity from $1.3 \times 10^{14} \text{ Wcm}^{-2}$ to $2.37 \times 10^{14} \text{ Wcm}^{-2}$.

In **Fig. 6.5**, we present our results of the high-order harmonics from diatomic carbon molecules. It is observed that when laser pulses of $\sim 10^{14}$ Wcm $^{-2}$ interact with the medium, the high-order harmonics that are generated with the laser pulses from 0.8 μm to 1.84 μm wavelengths contain a strong redshift (**Fig. 6.5 (b-h)**). This redshift is observed as a linear function of the laser intensity and increases rapidly when the laser intensity is varied between the generation threshold (e.g., $\sim 0.8 \times 10^{14}$ Wcm $^{-2}$) and the saturation intensity (e.g., $\sim 4.56 \times 10^{14}$ Wcm $^{-2}$) for different driving laser wavelengths. From the harmonic spectra at each wavelength, it is observed that the shift in the harmonics is almost the same for each harmonic. For example, for the harmonics generated with the 0.8 μm laser (**Fig. 6.5 (b)**), a redshift of 0.46 eV is observed for the harmonic at ~ 17 eV and ~ 20 eV, when the laser intensity is increased from 8.4×10^{13} Wcm $^{-2}$ to 2.3×10^{14} Wcm $^{-2}$. Similarly, for other laser wavelengths, shown in **Fig. 6.5 (c-h)**, a shift from 0.2 eV to 0.3 eV is observable when driven with wavelengths ranging from 1.4 μm to 1.84 μm . The laser parameters used for HHG at different driving laser wavelengths are given in the **Table 6.1**. A small discrepancy is observed in the laser intensity due to different efficiency of OPA at variable wavelengths. On the other hand, for 400 nm wavelength driving lasers, no redshift is observed in the harmonics. Rather, it is observed that at very high laser intensities ($\sim 3.0 \times 10^{14}$ Wcm $^{-2}$), a blue shift in the harmonics appears, as shown in **Fig. 6.5(a)**.

From these observations, it can be inferred that the resonant states are not involved in producing redshift, as redshift is observable at all wavelengths, except at 0.4 μm . This blue shift at 0.4 μm laser pulses might be due to the normal HHG process at the rising edge of the laser pulse.

Table 6.1: Laser parameters used for high-order harmonic generation from diatomic carbon molecules.

λ (μm)	Source	τ (fs)	Peak Intensity Min ($\times 10^{14}$ Wcm $^{-2}$)	Peak Intensity Max (10 14 Wcm $^{-2}$)
0.40	Ti:sapp.; 2 nd Har.	42	0.75	3.00
0.80	Ti:sapphire.	42	0.84	2.30
1.40	OPA, Signal	50	1.10	2.30
1.45	OPA, Signal	45	2.19	4.56
1.50	OPA, Signal	60	1.59	3.27
1.75	OPA, Idler	55	1.49	3.35
1.80	OPA, Idler	60	1.29	2.28
1.84	OPA, Idler	71	1.30	2.37

6.4.2 Redshift due to Molecular Dissociation

The second possibility of redshift in high-order harmonics could be molecular dissociation. Most recently, Bian *et al.* [5] predicted that if high-order harmonics are generated at the falling edge of the laser pulse, they might experience a strong redshift. He used non-Born-Oppenheimer approximation to model the harmonic spectra of H^{2+} and D^{2+} molecules and explained redshift. According to his model, when laser-pulses interact with the molecule, an electron is ionized from the ground state. In the second step, the molecular dissociation starts at the rising part of the laser pulse. At certain internuclear distance, the PICS of molecules increase rapidly. In the third step, the ionized electron is accelerated in the continuum. Since, the molecular dissociation is a long process (several tens of femtoseconds to picoseconds), the harmonics with high-yield are generated at falling edge of the driving laser. In this scenario, high-order harmonic spectrum will experience a redshift as the ionized electron is recombining with the state having different energy than that it was ionized.

We know that molecules have different dissociation periods. For the case of diatomic carbon molecule, the resonant period is at ~ 20 fs. Therefore, one way of checking the contribution of molecular dissociation in producing redshift could be to use laser pulses with very short pulse duration (<20 fs). With this technique, one can freeze the nuclear motion of C_2 molecules and generate harmonics before the molecular dissociation starts. This will confirm if the dissociation is really involved in producing redshift in the high-order harmonics.

References

- [1] R. A. Ganeev, Nonlinear Optical Properties of Materials (Springer, 2013).
- [2] T. Ozaki, R. A. Ganeev, M. Suzuki, and H. Kuroda, in (In Tech, 2010).
- [3] S. Baker, J. S. Robinson, M. Lein, C. C. Chiril, R. Torres, H. C. Bandulet, D. Comtois, J. C. Kieffer, D. M. Villeneuve, J. W. G. Tisch, and J. P. Marangos, Phys. Rev. Lett. **101**, 053901 (2008).
- [4] S. Baker, J. S. Robinson, C. A. Haworth, H. Teng, R. A. Smith, C. C. Chiril, M. Lein, J. W. G. Tisch, and J. P. Marangos, Science **312**, 424 (2006).
- [5] X.-B. Bian and A. D. Bandrauk, Phys. Rev. Lett. **113**, 193901 (2014).
- [6] M. A. Baig, M. A. Fareed, B. Rashid, and R. Ali, Phys. Plasmas **18**, 083303 (2011).
- [7] R. A. Ganeev, L. B. Elouga Bom, and T. Ozaki, Phys. Plasmas **18**, 083101 (2011).
- [8] J. J. Camacho, J. M. L. Poyato, L. Díaz, and M. Santos, J. Phys. B. **40**, 4573 (2007).
- [9] C. Dutouquet, S. Acquaviva, and J. Hermann, Spectrochim. Acta - Part B At. Spectrosc. **56**, 629 (2001).
- [10] M. Oujja, R. de Nalda, M. López-Arias, R. Torres, J. P. Marangos, and M. Castillejo, Phys. Rev. A **81**, 043841 (2010).
- [11] Y. Pertot, L. B. Elouga Bom, V. R. Bhardwaj, and T. Ozaki, Appl. Phys. Lett. **98**, 101104 (2011).
- [12] R. A. Clausius "Process for purifying graphite", Carbon N. Y. **23**, I (1985).
- [13] G. Sun, X. Li, Y. Qu, X. Wang, H. Yan, and Y. Zhang, Mater. Lett. **62**, 703 (2008).
- [14] L. B. Elouga Bom, Y. Pertot, V. R. Bhardwaj, and T. Ozaki, Opt. Express **19**, 3077 (2011).
- [15] P. Corkum and F. Krausz, Nat. Phys. **3**, 381 (2007).
- [16] C. T. Chen, Y. U. Idzerda, H.-J. Lin, N. V Smith, G. Meigs, E. Chaban, G. H. Ho, E. Pellegrin, and F. Sette, Phys. Rev. Lett. **75**, 152 (1995).
- [17] D. Wilson, D. Rudolf, C. Weier, R. Adam, G. Winkler, R. Frömter, S. Danylyuk, K. Bergmann, D. Grützmacher, C. M. Schneider, and L. Juschkin, Rev. Sci. Instrum. **85**, 103110 (2014).
- [18] P. Corkum, Phys. Rev. Lett. **71**, 1994 (1993).
- [19] E. Constant, D. Garzella, P. Breger, E. Mével, C. Dorrer, C. Le Blanc, F. Salin, and P. Agostini, Phys. Rev. Lett. **82**, 1668 (1999).
- [20] T. Popmintchev, M.-C. Chen, D. Popmintchev, P. Arpin, S. Brown, S. Alisauskas, G. Andriukaitis, T. Balciunas, O. D. Mücke, A. Pugzlys, A. Baltuska, B. Shim, S. E. Schrauth, A. Gaeta, C. Hernández-García, L. Plaja, A. Becker, A. Jaron-Becker, M. M. Murnane, and H. C. Kapteyn, Science **336**, 1287 (2012).
- [21] H. Singhal, V. Arora, B. Rao, P. Naik, U. Chakravarty, R. Khan, and P. Gupta, Phys. Rev. A **79**, 023807 (2009).
- [22] E. Sistrunk, J. Grilj, J. Jeong, M. G. Samant, A. X. Gray, H. A. Dürr, S. S. P. Parkin, and M. Gühr, Ultrafast Phenom. XIX **3**, 64 (2015).
- [23] F. Krausz and M. Ivanov, Rev. Mod. Phys. **81**, 163 (2009).
- [24] K. J. Schafer and K. C. Kulander, Phys. Rev. Lett. **78**, 638 (1997).
- [25] Wm. M. Wood, C. W. Siders, and M. C. Downer, Phys. Rev. Lett. **67**, 3523 (1990).

- [26] H. Shin, D. Lee, Y. Cha, K. Hong, and C. Nam, Phys. Rev. Lett. **83**, 2544 (1999).
- [27] H. J. Shin, D. G. Lee, Y. H. Cha, J. H. Kim, K. H. Hong, and C. H. Nam, Phys. Rev. A **63**, 53407 (2001).
- [28] F. Brandi, F. Giannanco, and W. Ubachs, Phys. Rev. Lett. **96**, 123904 (2006).
- [29] K. Kim, I. Alexeev, T. Antonsen, A. Gupta, V. Kumarappan, and H. Milchberg, Phys. Rev. A **71**, 011201 (2005).
- [30] X.-B. Bian and A. D. Bandrauk, Phys. Rev. A **83**, 041403 (2011).
- [31] R. A. Ganeev, M. Baba, M. Suzuki, and H. Kuroda, J. Appl. Phys. **99**, 103303 (2006).

Chapter 7

Conclusions and Applications

HHG is a technique to produce XUV or soft X-ray pulses with the ultrafast lasers by nonlinear frequency conversion. These pulses are used to study material properties in the XUV and soft X-ray region. Further, the broad bandwidth of harmonics is useful to produce attosecond pulses that are promising to capture and control the motion of electrons at attosecond timescales. Since the first observation of high-order harmonics in 1988 in gasses, the major drawback of this technique was the low conversion efficiency. In gaseous media, several methods such as HHG in gas cells and waveguides have been introduced to enhance the conversion efficiency and maximum conversion efficiency achieved for the low order harmonics is about 10^{-4} . However, it has been observed that conversion efficiency decreases drastically for higher frequencies.

In 2005, Ganeev *et al.* demonstrated high-order harmonics from laser-ablated plumes. This technique of HHG appeared to be an efficient method of producing intense XUV pulses over the gaseous media. It has been demonstrated that without using any appropriate phase matching technique (e.g. waveguides) high-order harmonics of conversion efficiency about 10^{-4} can be generated with this method. Further, laser-ablation technique also provides the opportunity to use a variety of materials for the high-order harmonic studies.

In HHG, one method of increasing high-order harmonic flux is to generate harmonics from atomic or molecular resonances. It has been observed that when atomic or molecular resonances contribute to coherent harmonic emission, high-order harmonic intensity increases about one to two orders of magnitude in certain energy region. In HHG from laser-ablated plumes, intense harmonics have been observed from different resonances. However, in most cases, the physical phenomenon of harmonic generation from these resonances was not clear. This was the main limitation to further advance research in this direction. In this thesis, we generate harmonics from laser ablated plumes containing different resonances and investigate the harmonic generation process involved behind. Along with the harmonic generation process, we also introduce new methods to generate broadband and intense harmonics from atomic and molecular resonances for the first time.

7.1 High-order harmonics from autoionizing states

Autoionizing resonances are ubiquitous in nature. In HHG from elements containing autoionizing resonance, significant intensity enhancement is observed in a single harmonic. This intense single harmonic is named RH and linewidth of this harmonic is observed about few nanometers. In laser-ablated plumes, most popular elements producing intense RH are indium, tin, and chromium. However, in laser-ablated plumes, physical phenomenon of RH generation was circumstantial since its first observation in 2006. We used mid-IR tunable pulses to study quantum trajectories of electron wavepacket in the vicinity of autoionizing resonance. Tin was used as a nonlinear medium because tin contains strong autoionizing resonance around 26 eV. Indium was used in parallel to confirm the universality of our observations (the results of indium will be presented in a separate manuscript).

Our main observations of RH are summarized below,

- ❖ At resonant energy, there are two harmonics. One is the RH generated from autoionizing resonance and second is the normal harmonic generated due to the three-step process.
- ❖ Quantum trajectories of RH and normal harmonic can be separated by careful detuning of the driving laser field.
- ❖ RH emission is locked in a certain energy range, within the linewidth and stark shift of the AIS.
- ❖ An energy shift is observable in RH when laser wavelength is detuned from the resonance. This energy shift is comparable to the linewidth of the AIS.
- ❖ Two satellite harmonics are observed from dressed states at frequency $\pm 2\Omega$.

On the behalf of these observations, we have explained the exact phenomenon of RH. This explanation has been provided by extending the four-step model of RH that was initially proposed by Dr. Strelkov in 2010 for single harmonic at resonant energy.

Applications

The applications of RH are given below,

A. Multiple intense harmonics from atomic and molecular resonances:

Our results provide firm evidence that RH involves the autoionizing state, thus clarifying the mechanism of intense harmonic generation. This, in turn, would allow the development of intense high-order harmonic and attosecond sources using the RH process, thus promoting novel applications in attosecond science. Considering that the applications of such technology would span a wide range of sciences.

High-order harmonics from dressed states has been revealed for the first time. This observation is not only important as a core process involved in RH generation, but it could also be used to further shorten the pulse duration of the intense RH sources. Our results show that one could generate multiple harmonics from AIS. In the current study, two dressed harmonics are generated due to the sub-cycle response of the driving field. However, in future, we can also extend this harmonic series by involving other dressed-states (for example $\pm 1\Omega$, $\pm 2\Omega$, $\pm 3\Omega$, and above) using two-color driving fields. Our numerical simulations confirm this possibility. In this way, the bandwidth of the intense RH could be greatly expanded, thus opening the way toward intense and short attosecond pulses.

Further, RH can also be generated from other atomic and molecular resonances. For example, we can generate harmonics from the Rydberg states. In HHG from gasses, harmonics from Rydberg states has been observed from argon (Michael Chini *et al.* *Nature Photonics*, **8** (2014) 437). However, in laser-ablated plumes, we have observed harmonics from Rydberg states of indium (not presented in the thesis). Therefore, harmonics from dressed Rydberg states will be useful to extend the bandwidth of this intense harmonics source. Further, RH is also observable from molecular resonances (Ferré *et al.* *Nature Communications*, **6** (2015) 5952). Therefore, the present study can be extended to molecular media as well.

The other advantage of this study might be that atomic and molecular resonances exist at different energies. Therefore, we can generate several harmonics at required wavelengths using a particular resonance and its dressed states.

B. Fundamental understanding and applications:

The study of atomic and molecular resonances is of great interest for ultrafast and attosecond spectroscopy (Kotur, M. *et al.* *Nat. Commun.* **7**, 10566 (2016); Ferré, A. *et al.* *Nat. Commun.* **6**, 5952 (2015); Ott, C. *et al.* *Nature* **516**, 374 (2014); Chini, M. *et al.* *Sci. Rep.* **3**, 1105 (2013); Ott, C. *et al.* *Science* **340**, 716 (2013); Sekikawa, T. *et al.* *Nature* **432**, 605 (2004)). However, in past, major studies of AIS have been performed mainly with the absorption techniques where XUV+IR pulses are required. Some of these studies report dynamics of AIS, for example, one- and two-electron interactions with the AIS and information about their line profiles.

As discussed above, our results clearly show direct involvement of AIS in RH generation via microscopic response, hence opening roots to study emission dynamics of AIS with ultrafast lasers (without XUV). For example, we can extract information about the absolute time that the electron stays in the AIS before emission, study electron-electron interaction, and interference of RH and direct harmonic at attosecond time scale by driving harmonics using pulses with certain duration, since the electron stays for a short time in the AIS. Further, the response of virtual quantum states for harmonic emission has been observed for the first time. Current spectroscopy tools (particularly in attosecond science) will provide opportunities to understand the nature of virtual states and their influence on the physical systems both in physics and chemistry, hence providing better control on the systems and roots to find new applications. This sub-cycle response of dressed states might also be useful to study the influence of dressed states on electron motion at attosecond time scales.

7.2 High-order harmonics from inner-shell giant resonances

Inner-shell giant resonances are mostly broader in nature than AIS. This is because inner-shell resonances involve multiple channels and complex energy level system. The contribution of inner-shell resonances in HHG was first observed by Ganeev *et al.* in 2007 (PRA **76** (2007) 023831. In this study, Ganeev *et al.* observed a complex harmonic series from laser-ablated

manganese. The involvement of inner-shell resonances in this complex harmonic series generation was later explained by Frolov *et al.* (PRA **82** (2010) 023424). Before this explanation in laser-ablated plumes, Frolov *et al.* already predicted HHG from the inner shells of xenon (PRL **102** (2009) 243901) that was later observed by Shiner *et al.* (Nat. Phys. **7** (2011) 464).

We decided to further investigate the properties of this complex harmonic series involving inner-shell resonances. For this purpose, we used manganese as a nonlinear medium. The advantage of using manganese as a nonlinear medium is that the inner-shell resonance of manganese involves only few channels, compared to other media. For example, in the case of xenon, inner-shell resonance appears from several channels (Kutzner *et al.*, PRA **40** (1989) 5052), whereas manganese resonance occurs mainly due to 3p-3d transitions. In this study, we revealed that in laser-ablated manganese plume Mn^+ responds as an active species for harmonic emission. Further, we have found that at certain laser conditions we can probe the inner-shell resonances with high-order harmonic spectroscopy.

Apart from the work presented in this thesis, we have recently observed some additional properties of HHG from inner-shell resonances. We have found that with the mid-IR driving laser, harmonics from inner-shell resonances are observable at laser pulse duration of 30 fs or below. However, these harmonics disappear when laser pulse duration is increased to 50 fs. Intense and broadband harmonics have been observed from inner-shell resonances with the few-cycle mid-IR driving fields. We have observed continuum like spectrum from inner-shell resonances at energy from 49 eV to 53 eV. An intensity enhancement of more than order of magnitude has been observed in this energy region. These additional results of high-order harmonics from inner-shell resonances will be presented in the manuscript.

Applications

Our results confirm that inner-shell resonances indeed participate in producing intense and broadband harmonics with the mid-IR driving fields. Further, we can also probe inner-shell resonances with the high-order harmonic spectroscopy, using certain laser conditions.

Previous photoionization studies have shown that several materials contain strong inner-shell resonances (Becker and Shirley, “VUV and Soft X-Ray Photoionization” (1996)). The current

study will be useful to search for an appropriate material to produce intense and broadband harmonics from inner-shell resonances, suitable for intense and short attosecond pulse generation. One interesting aspect of this study should be to use materials that contain strong resonances in the water window (Becker and Shirley, “VUV and Soft X-Ray Photoionization” (1996)). As we have observed intense harmonics from inner-shell resonances with the few-cycle mid-IR driving lasers, these laser conditions (with high intensity) might be more suitable for studying harmonics in water window, both from laser-ablated plumes and gaseous media. Further, HHG from inner-shell resonances is also interesting because one can study multi-electron dynamics with high-order harmonic spectroscopy since more than one electron contributes in such complex harmonic series generation.

7.3 Role of molecular resonances in high-order harmonic generation

Laser-ablated carbon plumes are appeared to be a source of intense harmonics. This nonlinear medium can be used to produce high-order harmonics of multi- μJ energy, without using any appropriate phase matching techniques (e.g. waveguides). However, the physical reasons of these intense harmonics were not clear. The major problem of understating the physics was the lack of information about active species responsible for harmonic generation. Our results show that at laser conditions where we observe intense harmonics, laser-ablated carbon plume contains an abundance of diatomic carbon molecules and high-order harmonics are generated from them. One reason of high intensity of harmonics from carbon plume might be the large photoionization cross-section of the diatomic carbon in the XUV region.

Further, we have found that high-order harmonics from diatomic carbon experience strong redshift at high laser intensities. This redshift is not common in high-order harmonics. It has been predicted that if HHG process occurs on the falling edge of the driving laser, the generated harmonics might experience redshift. This can only happen if some other change occurs on the rising part of the driving laser. Two possible changes predicted in molecular media at rising part of the driving laser are the excitation of the electron in the bound states or dissociation of molecules. In both cases, high-order harmonics might be generated at falling part of the driving laser and high-order harmonics might experience a redshift. In these processes, it has been predicted that high-order order harmonic yield may also increase drastically.

We explored the reasons behind the redshift observed in HHG from diatomic molecules and our results shows that this redshift appears probably due to the dissociation of diatomic molecules. This dissociation might be another reason for producing high-intensity harmonics from diatomic carbon. Further, we have observed that the harmonic yield is also high at mid-IR driving lasers. An intensity reduction of 30% is observed when driving laser wavelength was changed from 0.8 μm to 1.7 μm .

Applications

The high flux of high-order harmonics from carbon plumes makes this material attractive for the development of tabletop high-order harmonic source. The high intensity and broad bandwidth of harmonic with mid-IR driving laser show that this material can be used to produce intense single attosecond pulses.

Moreover, the contribution of diatomic molecules in HHG has been observed for the first time in laser-ablated plumes. Previous spectroscopic studies show that molecular species can be ablated from solid targets at certain laser ablation conditions. Therefore, the current study will be useful to explore the properties of molecular species that are not available in gaseous form. In this direction, preliminary results have been collected to study high-order harmonics from boron nitride. Surprisingly, we have observed high-order harmonics with intensity comparable to carbon harmonics. However, further work is required to understand the physics of HHG from boron nitride.

Résumé en français

1) Génération d'harmoniques d'ordres élevés

La génération d'harmoniques d'ordre élevé (ou HHG, pour « High-order harmonic generation ») est un processus extrêmement non-linéaire ayant lieu lorsqu'un atome ou une molécule interagit avec un champ laser intense ($\geq 10^{13} \text{ Wcm}^{-2}$). Ce processus d'HHG est communément décrit par un modèle quasi-classique à trois étapes [1]. Selon ce modèle, lorsqu'une impulsion laser ultra-rapide interagit avec un atome ou une molécule, elle l'ionise par effet tunnel en agissant sur un électron. Cette première étape est suivie de l'accélération de l'électron dans le continuum d'états sous l'effet du champ laser puis par la recombinaison de l'électron et de l'ion en émettant un photon de haute énergie. Un schéma illustrant ces trois étapes est donné en Fig. 1 :

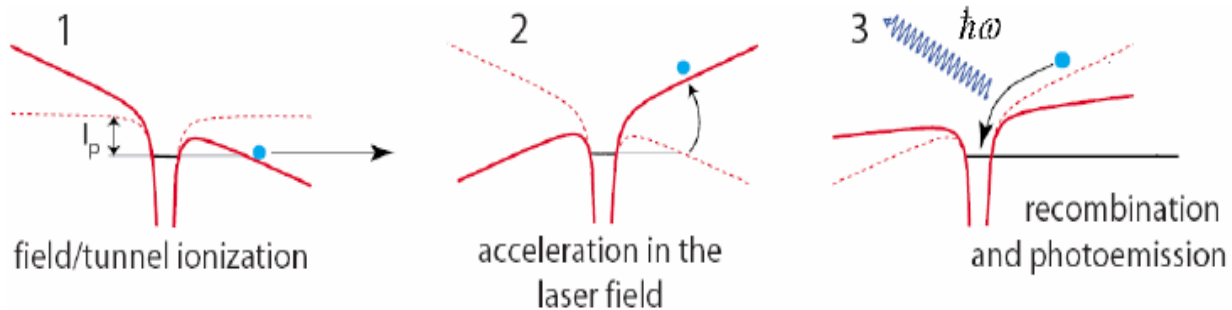


Figure 1: Illustration schématique de la génération d'harmoniques d'ordres élevés. Selon le modèle en trois étapes, un électron est d'abord ionisé par tunnelage (1). Ensuite cet électron est accéléré sous l'effet du champ laser (2) et finalement se recombine à l'atome en émettant un photon XUV (3) [2]

1.1 Rôle des différentes résonances en HHG

Le modèle à trois étapes suppose que seuls les électrons à l'état de repos participent à la HHG et que sont ignorées les contributions provenant des couches internes et des états de résonances.

Pourtant plusieurs résultats expérimentaux ont montré que le processus de HHG est perturbé par la présence de résonances atomiques ou moléculaires. Ganeev et collaborateurs [3] furent les premiers à l'observer pour la technique de HHG par ablation laser réalisée sur de l'indium In⁺. Ils mesurèrent une grande différence dans l'intensité d'une harmonique unique qu'ils attribuèrent à la présence d'états auto-ionisant (ou AIS pour « Auto-Ionizing State ») en HHG au-dessus du seuil d'ionisation. Plus tard, ces perturbations de la HHG furent observées dans plusieurs matériaux du fait de la présence de résonances des couches internes [4], ou d'ionisation en dessous [5,6] et au-dessus [7] du seuil.

Le mécanisme de HHG pour ces résonances est différent. Pour cette thèse nous avons utilisés différents éléments contenant plusieurs types de résonances comme celles des couches internes, d'états liés ou d'AIS que nous avons étudiés en vue d'estimer leurs contributions au processus d'HHG cohérent.

2) Montage expérimental

Les mesures expérimentales furent réalisées au centre ALLS (« Advanced Laser Light Source »). Utilisant un laser Ti:saphir de haute puissance fournissant des impulsions électromagnétiques dans une large gamme du spectre. Deux lignes laser du centre sont utilisées pour la HHG par ablation laser. Les deux lignes sont capables de produire des impulsions laser à 350 mJ et 80 mJ à des taux de répétitions de 10 Hz et 100 Hz respectivement. La longueur d'onde centrale de ces pulses est de ~ 0,8 μm pour une durée avant compression de ~ 210 ps. Ces impulsions sont ensuite traités sous différents montages optiques afin de générer des impulsions de longueur d'ondes allant de 0,266 μm à 2,3 μm. Ces impulsions laser aux caractéristiques prédéfinies sont utilisées pour générer des harmoniques d'ordre élevé sous formes d'impulsions dans la gamme XUV de plusieurs μJ d'énergie. Le détail du montage expérimental utilisé pour la HHG est donné dans la suite.

Un schéma du montage expérimental utilisé pour la HHG par ablation laser est donné **Fig. 2**. On y voit une petite part du faisceau envoyé vers un compresseur par un séparateur de faisceau (BS) où il est compressé à 40 fs par l'utilisation d'un compresseur basse énergie à double réseaux. Ces

impulsions compressées d'énergie proche de 5mJ subissent ensuite une conversion de fréquence en passant par un amplificateur paramétrique optique (APO) en lumière blanche (HE-TOPAS, Light Conversion, Inc.).

Cet APO, capable de produire un Signal à 1,1 mJ ($\lambda_{\text{sig}} = 1.45 \mu\text{m}$) et un Idler à 0,9 mJ ($\lambda_{\text{Idl}} = 1.80 \mu\text{m}$) est installé sur la ligne fonctionnant à 100 Hz. Le faisceau Idler est séparé du Signal par un miroir dichroïque (DM) puis filtré spatialement en le focalisant sous vide au travers d'une ouverture circulaire de 250 μm de diamètre, pour une transmission de 75%-80%. Le restant d'énergie (~75 mJ) fournie par le laser Ti:saphir est également compressé à 40fs par un compresseur haute énergie à double réseaux puis utilisé afin d'amplifier l'Idler au travers d'un cristal BBO à accord de phase de type-II. Ce système peut produire un Idler de 10 mJ à 1,8 μm pouvant être ajustée sur une gamme allant de 1,6 μm à 2,2 μm .

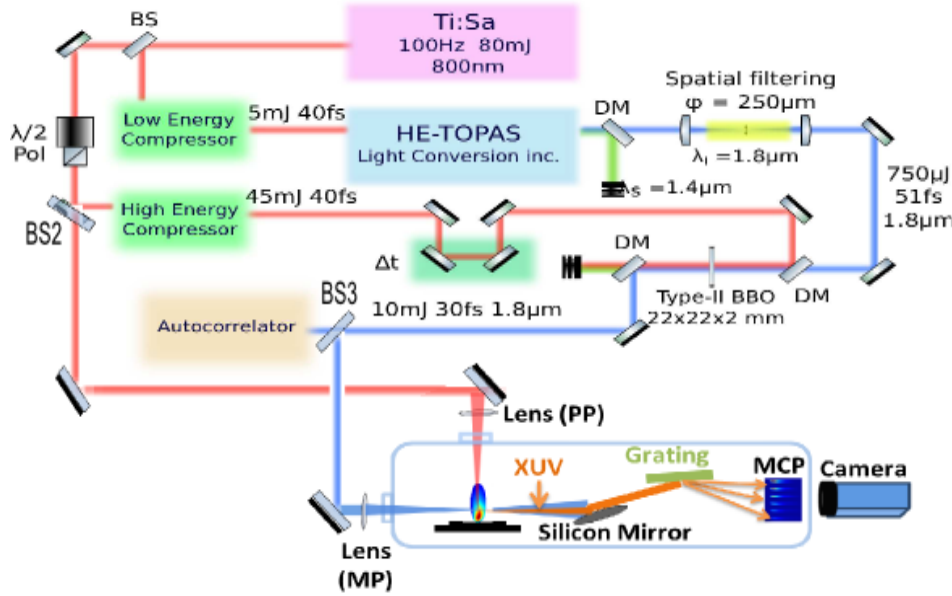


Figure 2: Diagramme schématique du montage expérimental utilisé pour la génération et la détection d'harmoniques d'ordres élevés au travers d'un panache obtenu par ablation laser. Lexique : BS : Séparateur de faisceau. DM : Miroir dichroïque. Pol : Polariseur. φ : ouverture circulaire. Autocorrelateur : auto-correlateur de génération de seconde harmonique en réflexion, fait maison. λ_l : longueur d'onde centrale de l'Idler de l'amplificateur paramétrique optique.

Pour la HHG par ablation laser, nous utilisons deux faisceaux laser que nous appelons pré-pulse (PP) et pulse principal (MP). Le premier sert à effectuer l'ablation plasma sur une cible solide, le

second (qui est le faisceau Idler) est utilisé pour la HHG. Une partie du faisceau laser est soustraite à l'étape d'amplification par un séparateur de faisceau (BS2) pour être focalisée sur une cible solide pour l'ablation. La cible solide est placée dans une chambre sous une pression de $\sim 10^{-5}$ Torr. L'intensité du PP est maintenue à $10^{-10} \text{ W.cm}^{-2}$ et un panache plasma est ablaté dans un disque de diamètre $\sim 200 \mu\text{m}$. Après un délai de 30 ns à 70 ns le faisceau Idler est focalisé sur ce panache plasma (ou LAP pour Laser-Ablated Plume) pour la génération d'harmoniques, ce temps est employé pour permettre au panache de s'étendre suffisamment au-delà de la surface de la cible solide. Les harmoniques générées sont alors envoyées vers un spectromètre à rayons X mous constitué d'un réseau champ-plat Hitachi (1200 lignes. mm^{-1}) et d'une plaque multi-canaux (PMC) couplée à un écran phosphoré. Le spectre ainsi étalé est mesuré par une caméra CMOS 16-bits (PCO-edge).

3) Résultats et discussions

Pour cette thèse nous utilisons différents éléments contenant plusieurs types de résonances (auto-ionisation, résonance géante, etc...) et étudions leur rôle dans la HHG. L'étain, le manganèse et le carbone diatomique sont utilisés comme milieux non-linéaires puisqu'ayant de fortes résonances à différentes énergies. Une résonance de l'étain se trouve à $\sim 26.35 \text{ eV}$, au-dessus du seuil d'ionisation comme vu par la présence d'AIS. Le manganèse a une résonance géante dans ses couches internes à $\sim 51 \text{ eV}$ due à des transitions 3p-3d. Les molécules de carbones diatomiques ont des résonances pouvant provenir de la dissociation moléculaire, de l'AIS ou d'états liés.

Dans un premier temps nous utilisons l'étain comme milieu non-linéaire pour la HHG afin d'étudier l'auto-ionisation par l'état $4d^{10}5s^25p$.

3.1 Génération d'harmoniques d'ordre élevés via Sn^+

Nous utilisons des impulsions laser à haute longueur d'onde ($1.75 \sim 1.90 \mu\text{m}$) pour observer le mécanisme de génération impliquant l'AIS. Nous appelons cette harmonique, harmonique résonante (HR). Le spectre d'harmonique observé par excitation à $1,84\mu\text{m}$ est donné **Fig. 3.1**, il présente une HR intense aux alentours de 26 eV , amplifié par la transition $4d^95s^25p^2 \rightarrow$

$4d^{10}5s^25p$ de l'étain Sn^+ . On aperçoit sur cette figure que vers 26 eV deux harmoniques se superposent, celle de plus forte intensité est la HR et l'autre est la 39eme harmonique non-résonante du Sn^+ . Cette harmonique non-résonante est générée par le processus conventionnel en trois étapes, lorsque les électrons dans le continuum d'états se recombinent directement vers l'état normal du Sn^+ . Ce qui contraste avec des travaux antérieurs qui montraient que la HR dominait en intensité les contributions non-résonantes. Une explication provient de la longueur d'onde d'excitation laser ($0.8 \mu m$) lors des précédents travaux, qui donnait une HR d'intensité vingt fois supérieure au signal non résonant [8], rendant ce dernier difficile à distinguer. Dans le cas présent, l'utilisation d'une longueur d'onde laser à $1,84 \mu m$ entraîne un rapport d'intensité entre la RH et les modes non résonants de 6 seulement, permettant l'observation de ces derniers.

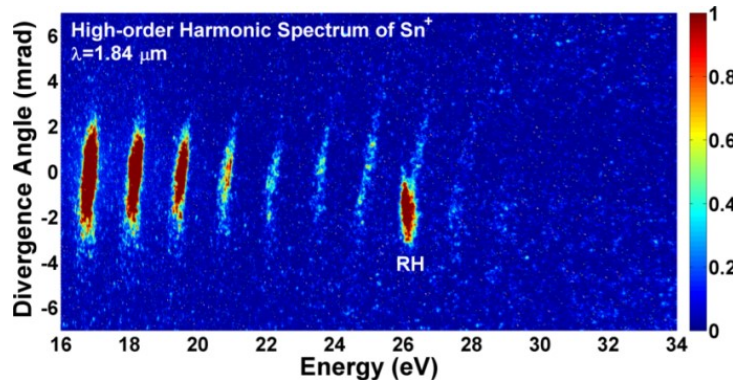


Figure 3.2: Spectre d'harmoniques d'ordres élevés du Sn^+ par un laser à $1.84 \mu m$, montrant le chevauchement du HR avec une harmonique non-résonante. Ce spectre est mesuré pour une intensité du laser de $\sim 1.43 \times 10^{14} W cm^{-2}$.

3.1.1 Réponse d'harmonique à résonance dans la bande spectrale du laser

Puisque les lasers utilisés pour la génération de HR sont à large bande, la HR répond dans une certaine bande de fréquence à ces impulsions laser [8]. Nous étudions la réponse HR pour des longueurs d'onde laser allant de $1,80 \mu m$ à $1,90 \mu m$, les résultats sont présentés Fig. 3.2. Cette figure montre les spectres d'harmoniques d'ordre élevé pour un plasma d'étain aux alentours de la résonance. Une HR de forte intensité est observée à $1,84 \mu m$ qui correspond exactement au 39eme ordre de la transition radiative du Sn^+ à 26,3 eV, et cette intensité décroît à mesure que l'on s'éloigne de cette longueur d'onde. Seule une faible HR est observée pour un laser à $1,81 \mu m$ ou $1,89 \mu m$ et elle disparaît complètement à $1,80 \mu m$ ou $1,90 \mu m$. Ainsi, ces résultats

démontrent que pour l'utilisation d'un laser de largeur spectrale 100 nm, la HR du Sn^+ est principalement due à une réponse centrée à 1,84 μm d'une largeur de ± 30 nm. Un léger décalage en énergie de 0,3 eV de la HR est également observé lorsque le laser passe de 1,83 μm à 1,86 μm , il est dû au passage au travers de la bande spectrale de l'AIS.

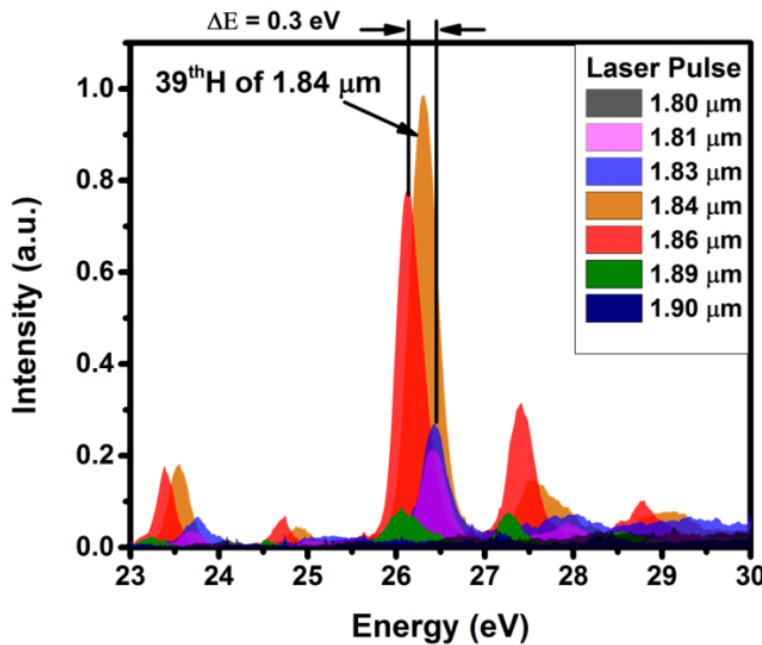


Fig. 3.2: La réponse HR à différentes longueur d'onde d'excitation laser allant de 1.80 μm à 1.90 μm . Le maximum d'intensité est observée pour 1.84 μm , qui correspond exactement au 39eme ordre harmonique de la transition $4\text{d}^{10}5\text{s}^25\text{p} \rightarrow 4\text{d}^95\text{s}^25\text{p}^2$ du Sn^+ , le signal décroît rapidement lorsque la longueur d'onde du laser est changée. La HR disparaît complètement lorsque le laser émet à 1.80 μm et 1.90 μm . L'intensité du laser pour ces mesures est maintenue à $\sim 1.3 \times 10^{14} \text{ Wcm}^{-2}$.

Lorsque la longueur d'onde de la HR est fixée dans la fenêtre de l'AIS, et qu'elle répond à au moins 60% de la bande spectrale du laser, les harmoniques non résonantes qui sont due au processus à trois étapes sont séparées de la HR. Ceci peut être réalisé en ajustant soigneusement la longueur d'onde du laser depuis l'APO, le résultat est visible Fig. 3.3.

La **Fig. 3.3 (a)** présente le spectre d'harmoniques d'ordre élevé du Sn^+ à 1,75 μm , avec une HR visible à 26,3 eV. Cette longueur d'onde correspond exactement à la 37eme harmonique de la transition $4\text{d}^{10}5\text{s}^25\text{p} \rightarrow 4\text{d}^95\text{s}^25\text{p}^2$. On observe sur ce spectre un léger décalage sur la queue de la HR due à un chevauchement avec la 37eme harmonique non résonante du laser à 1,75 μm . Nous

savons à partir des enseignements de la **Fig. 3.2** que l'émission de la HR est liée à la bande spectrale de l'AIS qui est impliquée dans sa génération et que la HR répond fortement dans une fenêtre de ± 30 nm dans la bande du laser. Toutefois, l'harmonique non résonante qui est obtenue par le processus normal à trois étapes a une énergie déterminée par la longueur d'onde centrale du laser. Par conséquent en ajustant le laser à $1,785 \mu\text{m}$ nous observons que le décalage spectral entre la HR et l'harmonique non résonante croît et que les deux signaux sont séparés comme on peut le voir **Fig. 3.3 (b)**.

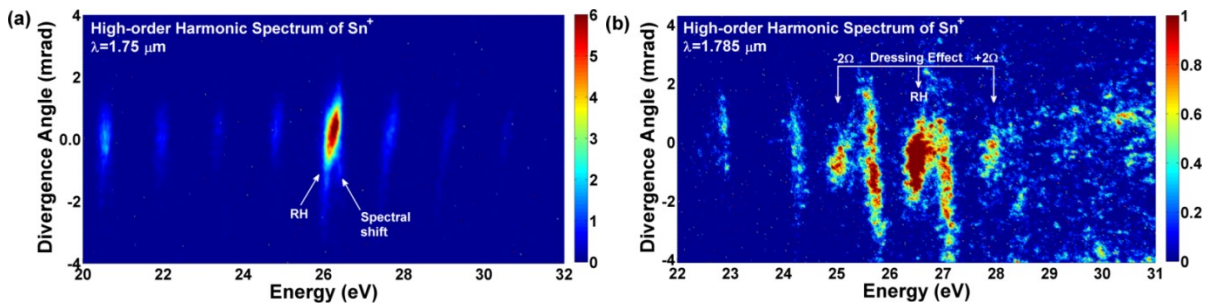


Figure 3.3: (a) Spectres d'harmoniques du Sn^+ pour un laser de longueur centrale $1.75 \mu\text{m}$, montrant le chevauchement de la HR avec l'harmonique non-résonante à 26.3 eV . (b) Spectres d'harmoniques du Sn^+ pour un laser de longueur centrale $1.785 \mu\text{m}$, montrant que la HR et le mode non-résonant peuvent être séparés en ajustant la longueur d'onde d'excitation. Deux harmoniques cohérentes apparaissent sur ce spectre à $\pm 2\Omega$ autour de la HR, générés par l'AIS. L'intensité du laser pour ces mesures est maintenue à $\sim 1.4 \times 10^{14} \text{ Wcm}^{-2}$.

Par cet ajustement hors résonance de la longueur d'onde du laser nous mettons en évidence un fait jusqu'ici ignoré concernant les harmoniques d'ordre élevé. Les spectres d'harmoniques montrent que lorsque la longueur d'onde du laser est légèrement modifiée, deux harmoniques additionnelles apparaissent à 25,0 eV et 27,9 eV. Ces harmoniques satellites sont situées exactement à $\pm 2\Omega$ autour de la HR, avec Ω l'énergie des photons produits par le laser. La divergence de ces deux satellites est identique à celle de la HR. Nous interprétons ces observations par la génération d'harmoniques par AIS. Dans le modèle original en quatre étapes proposé par Strelkov [9], un seul état (celui de l'AIS dans le cas de Sn^+) est impliqué dans une résonance multi-photonique avec le laser. Toutefois nos observations expérimentales montrent que dans la génération de HR, le continuum d'états électroniques peut diffuser vers trois états différents (dans la troisième étape du modèle à quatre étapes) ; l'AIS et les deux états situés à $\pm 2\Omega$ autour de lui. Lors de la quatrième étape, cet électron diffusé recombine vers l'état

fondamental en émettant trois HR. Ce mécanisme complet de génération de HR est dépeint Fig. 3.4.

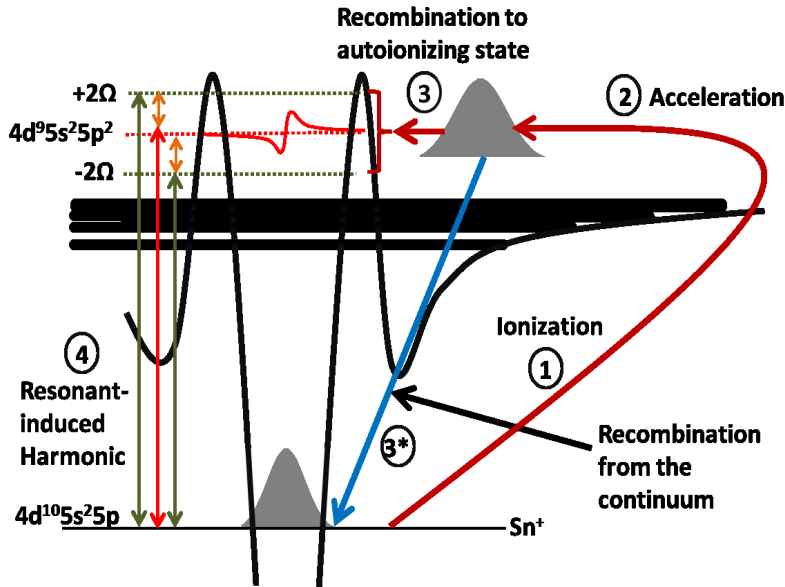


Figure 3.4: Diagramme énergétique de l'AIS du Sn^+ . Lorsqu'une impulsion laser intense ($\sim 10^{14} \text{ Wcm}^{-2}$) interagit avec Sn^+ , un électron est extrait de l'état fondamental (1). Cet électron est ensuite accéléré dans le continuum par le champ laser appliqué (2). L'électron dans le continuum peut suivre deux voies différentes. Recombiner directement vers son état initial (3*) et générer une harmonique non-résonante à l'énergie de la HR ou transiter jusqu'à l'AIS (3) et ensuite recomburer vers l'état fondamental et générer une HR (4). Selon ce scénario, il existe une possibilité de générer 3 HR cohérentes.

3.2 Génération d'harmonique d'ordre élevé dans le manganèse

Afin d'étudier la part provenant des couches internes dans la HHG, nous utilisons du manganèse comme milieu non linéaire. Le manganèse est connu pour permettre la génération de deux séries d'harmoniques d'ordre élevé [10]. Toutefois, la physique de cette double génération d'harmoniques est circonstancielle et souffre de peu de preuves expérimentales. Nous avons utilisés différents procédés expérimentaux pour étudier la physique sous-jacente. Dans un premier temps, un spectre d'harmoniques d'ordre élevées est mesuré sous laser à $0,8 \mu\text{m}$, voir Fig. 3.5.

Nous avons pu observer dans ces conditions que le panache de manganèse permet de générer des harmoniques jusqu'au 81eme ordre (~ 125 eV; 9.87 nm). Dans le processus standard de HHG, le spectre d'harmoniques élevées est constitué d'un plateau et un seuil [1]. Le plateau contenant une série d'harmoniques virtuellement plate et le seuil donne l'harmonique maximale qui peut être générée à partir du matériau usité. Toutefois, pour le cas du manganèse, le spectre présente deux séries d'harmoniques d'ordres élevées, la première allant jusqu'au 31eme ordre et la seconde commençant à 51 eV du 3eme ordre au 81eme ordre voire plus. Nous avons noté que cette seconde série n'est observable que sous forte intensité d'excitation laser. Par exemple, le spectre de la **Fig. 3.5** est mesuré pour un laser d'intensité $\sim 1.0 \times 10^{15}$ Wcm⁻² soit un ordre de grandeur plus intense que les conditions usuellement mises en œuvre pour la HHG par ablation laser ($\sim 10^{14}$ Wcm⁻²).

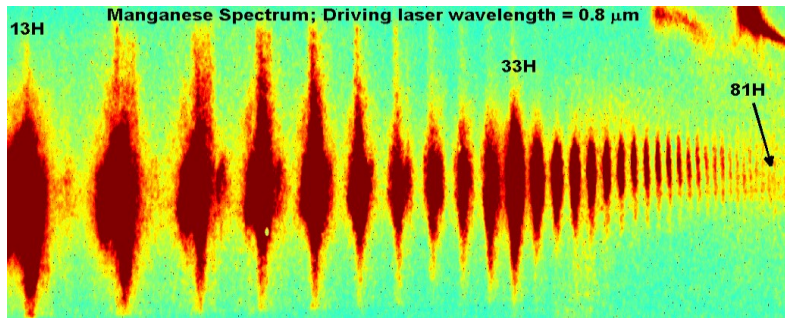


Figure 3.5: Spectres d'harmoniques d'ordres élevées produite dans le manganèse, générées par un laser à 0,8 μm. Ce spectre montre que des harmoniques jusqu'au 81eme ordre (~ 125 eV; 9.87 nm) sont générées, sous un laser d'intensité $\sim 1 \times 10^{15}$ Wcm⁻². Ce spectre présente deux séries d'harmoniques, où la seconde série commence au 33eme ordre.

Il peut y avoir deux raisons à l'origine de cette seconde série d'harmonique, la première étant le contenu du panache de manganèse ablaté qui peut contenir des éléments à potentiel d'ionisation élevée (comme Mn²⁺ ou Mn³⁺) qui génèrent ces harmoniques, cet effet pouvant être estimé en ajustant le seuil d'harmonique par le potentiel d'ionisation [10]. La seconde possibilité étant une contribution des électrons des couches internes à la HHG [11]. Nous estimerons plus loin dans ce manuscrit le poids de chacune de ces contributions.

3.2.1 Ajustement du seuil d'harmoniques par le potentiel d'ionisation

En HHG, le seuil est précisément estimé par le modèle en trois étapes [1] qui lui prédit des dépendances avec le potentiel d'ionisation et avec l'énergie pondéromotrice gagnée par un électron dans le continuum. Ganeev et collaborateurs ont mesuré les seuils d'harmoniques de plusieurs matériaux soumis à l'ablation laser et mis en évidence que le manganèse avait une réponse dominée par le potentiel d'ionisation du Mn^{2+} , voit **Fig. 3.6**.

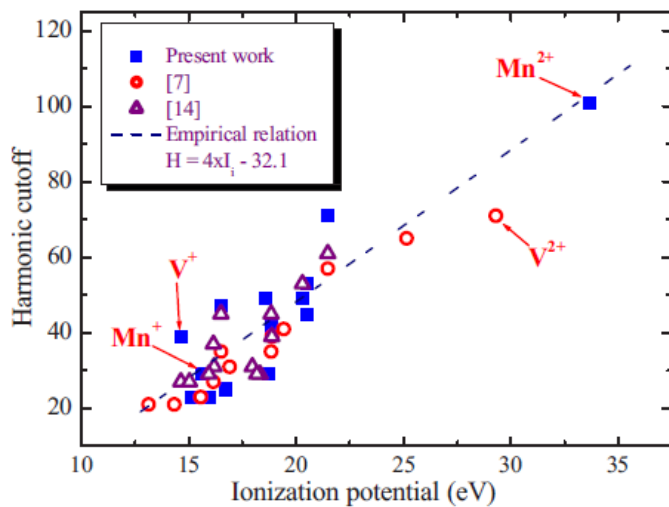


Figure 3.6: Evolution du seuil de génération d'harmoniques d'ordres élevées avec le potentiel d'ionisation, linéaire, elle montre un très bon accord sur le cas du Mn^{2+} [10].

3.2.2 Rôle des résonances des couches internes en HHG

L'implication des résonances des couches internes et le second phénomène pouvant être à l'origine de cette double série d'harmoniques, leur contribution en HHG fut d'abord observée par Shiner dans les harmoniques élevées du xénon [11]. Il observa que lorsque ces résonances sont perturbées, des harmoniques larges bandes de largeur 30 eV sont générées à 100 eV. Le manganèse présente une résonance des couches internes intense vers 51 eV [12], résultant principalement des transitions 3p-3d. Nous comparons les sections efficaces de photo-ionisation (SEPI) du manganèse pour estimer les perturbations que cette résonance peut provoquer sur la HHG.

La comparaison des spectres de SEPI et de HHG du manganèse révèle des tendances similaires, en particulier vers 50 eV, voir **Fig. 3.7**. A cette énergie, la SEPI est élevée du fait des transitions 2p-3d du manganèse, de même le spectre des harmoniques présente un maximum local mettant en évidence le rôle de ces transitions dans la génération de la seconde série d'harmoniques.

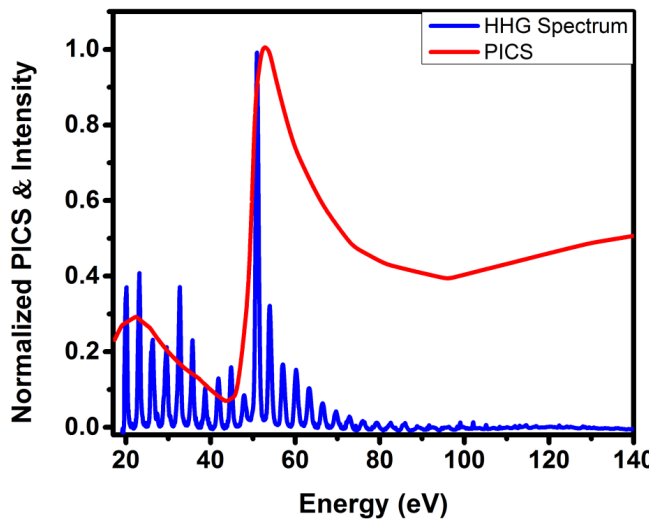


Figure 3.7: Spectres de section efficaces de photo-ionisation du manganèse (rouge) et de HHG (bleu).

Le spectre d'absorption optique du Mn^+ montre que les deux états 3d et 4s, respectivement aux énergies 51,6 eV et 50,16 eV, contribuent à l'accroissement de la SEPI vers 51 eV. Le spectre mesuré via excitation à 0,8 μm ne permet pas de déterminer directement laquelle de ces résonances est impliquée dans la HHG mais ce peut être résolu en stimulant les harmoniques par des impulsions dans l'infra-rouge moyen.

3.2.3 Génération d'harmoniques sous impulsions laser à haute longueur d'onde

Nous avons réalisé la HHG par impulsions laser à haute longueur d'onde (1,82 μm , $4.0 \times 10^{14} \text{ Wcm}^{-2}$), les spectres d'harmoniques issues du manganèse sont présentés **Fig. 3.8**. La **Fig. 3.8 (a)** montre la forte intensité de la 75eme harmonique à ~ 51 eV (souligné par la ligne pointillée) ainsi que la 73eme harmonique par comparaison à la 71eme et aux ordres inférieurs issus de la première série. La **Fig. 3.7** montrait que sous excitation à 0,8 μm la génération d'harmoniques était amplifiée à 51 eV uniquement, ici à 1,82 μm , l'amplification du 73eme ordre à eV nous

informe que ces perturbations à plus basse énergies sont dues à la transition 3p-4s. Cette perturbation à plus faible énergie apparaît systématiquement et prouve non seulement que les états de coeurs 3p participent à la HHG mais aussi que le Mn^+ y joue un rôle actif. Le tracé de la **Fig. 3.8 (b)** offre une visualisation plus précise des perturbations sur les harmoniques aux alentours de 51 eV.

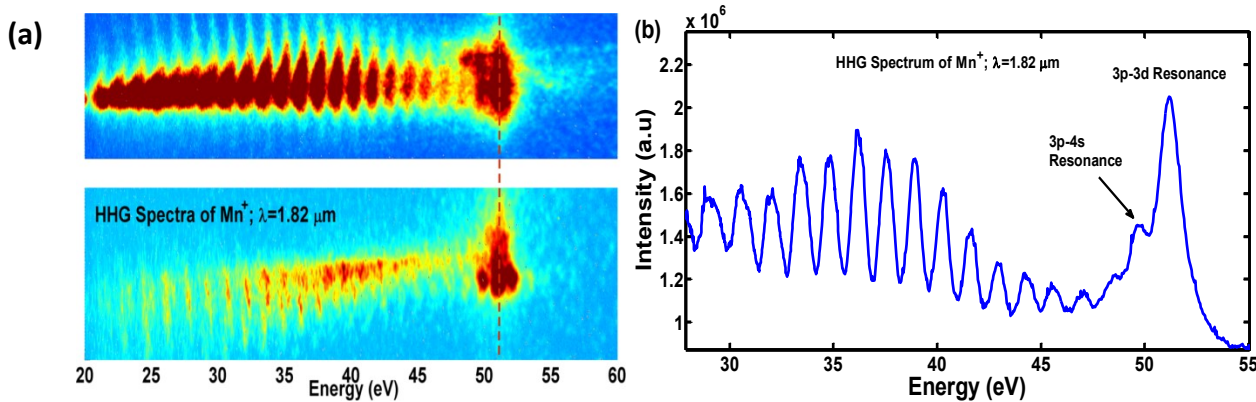


Figure 3.8: (a). Spectres d'harmoniques d'ordres élevées du manganèse sous laser à 1,82 μm. L'intensité des harmoniques augmente à 51 eV en raison de la résonance 3p-3d du matériau et l'intensité élevée des harmoniques voisines (~50 eV) sont dues à la résonance 3p-4s. **(b).** Spectre montrant les perturbations sur le signal des harmoniques causées par les résonances 3p-3d et 3p-4s.

3.3 Génération d'harmonique d'ordre élevé dans le graphite

Nous avons remarqué lors de mesures expérimentales que la génération d'harmoniques par des matériaux carbonés est étonnamment élevée et présente un fort décalage vers le rouge. Les processus physiques derrière ces observations sont inconnus. Les éléments actifs responsables de la HHG dans cas de l'ablation laser du graphite sont indéterminés du fait de la grande variété d'éléments carbonés ablatés. Nous avons donc, dans un premier temps entrepris d'établir les éléments contribuant à la HHG en effectuant de la spectroscopie d'émission plasma résolue en temps.

3.3.1 Spectroscopie par claquage laser résolue en temps

La spectroscopie par claquage laser résolue en temps (ou TR-LIBS pour « Time-resolved laser-induced breakdown spectroscopy ») est une technique permettant de mesurer les éléments

carbonés présents dans le panache de graphite issu de l'ablation laser. Le spectre d'émission plasma est collecté par un spectromètre TR-LIBS Newport, MS260i, les lignes d'émissions plasma mesurées 30ns après le début de l'ablation (t_{sa}) sont présentées **Fig. 3.9**. Le spectre est collecté dans le visible (410 nm à 580 nm) où se trouvent les principales émissions du carbone monoatomique et des molécules carbonées [13, 14], parmi lesquelles on trouve les raies de Swan typiques de la présence de carbone diatomique C₂ [15]. Les raies adjacentes observées sont quant à elles associées à la transition d³Π_g → a³Π_u qui appartient à la progression vibrationnelle Δv = 0, ±1 et +2 raies. Les SEPI des raies (2,0), (1,0), (0,0) et (0,1) sont observés à 436, 473, 516 et 563 nm respectivement. À partir de ce spectre il est évident que le panache plasma issu du graphite contient du C₂ en abondance.

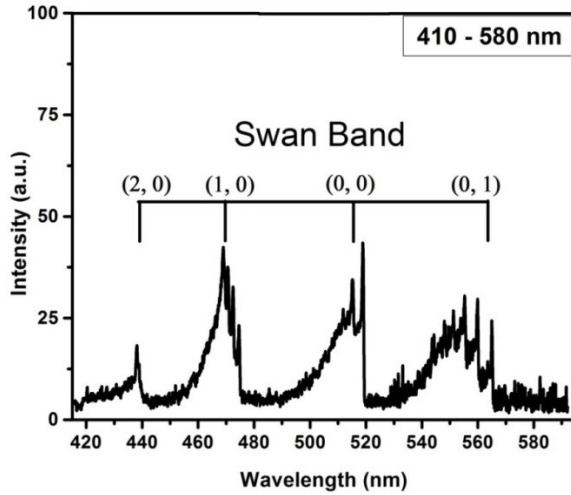


Figure 3.9: Spectre d'émission du plasma de graphite, dominé par les transitions vibratoires du carbone diatomique (C₂). Le signal est collecté après $t_{sa} = 30$ ns dans la gamme visible du spectre électromagnétique 410 nm à 580 nm.

Curieusement, ce spectre ne présente aucune signature provenant de transitions ioniques ou neutre du carbone monoatomique contrairement à ce qui est habituellement observé pour d'autres matériaux soumis à ablation laser nanoseconde ou femtoseconde [13, 15]. Nous avons remarqué que pour les paramètres utilisés pour le pré-pulse (PP) envoyé sur la cible de graphite (durée d'impulsion ~ 210 picosecondes, longueur d'onde centrale 0.8 μm à $\sim 10^{10}$ Wcm⁻²), le panache ablaté à de fortes raies d'émission moléculaires, C₂ en particulier. Ce qui contraste fortement avec précédentes mesures d'harmoniques par LAP, quand principalement des particules monoatomiques à faibles densités furent utilisées pour la HG [7]. À notre

connaissance, il s'agit ici de la première observation de contribution du carbone diatomique par la technique de LAP. Par conséquent, HHG à partir de graphite LAP est un premier milieu moléculaire qui peut être utilisé pour étudier la dynamique moléculaire de HHG à partir de matières solides.

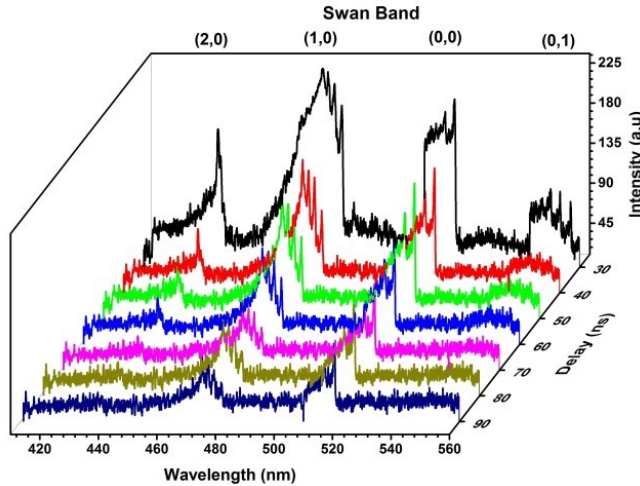


Figure 3.10: Variations des raies de Swan à $t_{sa} = 30$ ns à 90 ns, dans la gamme visible du spectre électromagnétique 410 nm à 560 nm à une intensité de PP fixée à 3.0×10^{10} Wcm $^{-2}$.

La variation temporelle de l'intensité d'émission des raies de Swan du plasma est obtenue pour différents t_{sa} . La région spectrale entre 410 nm et 560 nm est sélectionnée pour ces mesures. Après ablation à 3.0×10^{10} Wcm $^{-2}$, l'émission du plasma est collectée pour des t_{sa} de 30 ns à 90 ns, voir **Fig. 3.10**. Cette technique de spectroscopie a auparavant démontré son utilité dans la détermination de conditions optimales pour l'obtention d'une HHG intense à partir de matériaux solides [16]. De cette figure nous notons que l'émission de la raie de Swan, intense après 30 ns, décroît rapidement lorsque le plasma s'étend, pour pratiquement disparaître après 90 ns. Cette observation suggère que les molécules de C₂ sont d'abord abondantes à 30 ns avant de disparaître vers 90 ns. Afin de déterminer le délai pour lequel l'intensité de HHG est maximale, nous effectuons des mesures avec un retard entre le PP et le MP. Il est à noter qu'en plus de ce délai entre PP et MP, un autre paramètre d'importance est l'intensité du PP qui conditionne, via la densité du panache ablaté, le flux des harmoniques. Ainsi l'intensité de PP optimale pour du HHG sur graphite par LAP est $\sim 1.4 \times 10^{10}$ Wcm $^{-2}$. Une intensité supérieure provoque l'apparition de raie d'émission de carbone monoatomique qui s'accompagne d'une réduction drastique de

l'intensité des harmoniques. De manière similaire, un PP trop peu intense (voir discussion dans la suite) réduit le flux de photon des impulsions XUV. Afin de mieux cerner les contributions partagées entre l'intensité du PP et le délai le séparant du MP, nous utilisons deux PP à différentes intensités proche de la valeur optimale pour le LAP sur graphite, et nous faisons varier ensuite le délai entre PP et MP.

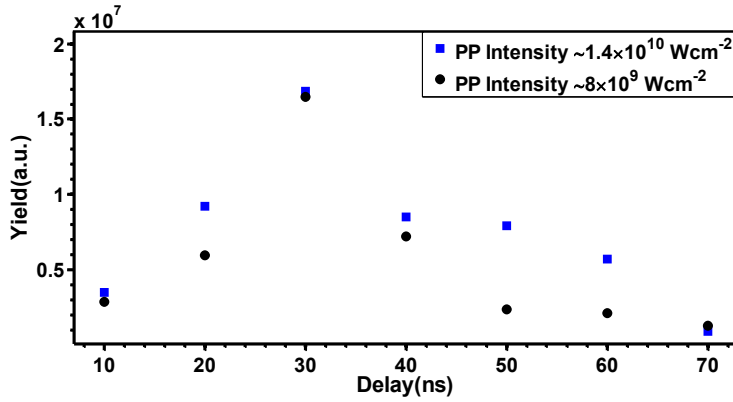


Figure 3.11: Variations du rendement de génération d'harmoniques d'ordres élevées en fonction du délai entre PP et MP pour deux intensité de PP différentes : $\sim 1.4 \times 10^{10} \text{ Wcm}^{-2}$ (carrés bleus) et $\sim 8 \times 10^9 \text{ Wcm}^{-2}$ (cercles noirs) pour un MP de $\sim 2.5 \times 10^{14} \text{ Wcm}^{-2}$.

La **Fig 3.11** présente la variation du rendement en harmonique en fonction du délai PP-MP allant de 10 ns à 70 ns pour un MP maintenu constant à $\sim 2.5 \times 10^{14} \text{ Wcm}^{-2}$. Nous pouvons observer que pour un PP de $1.4 \times 10^{10} \text{ Wcm}^{-2}$, un très faible signal apparaît sur le PMC à un délai aussi court que 2 ns puis en augmentant le délai on obtient un taux suffisant de conversion à partir de 10 ns. Toutefois, à des temps aussi court le plasma se trouve à une température élevé provoquant un important bruit en émission. Les résultats montrent que le meilleur rendement de conversion en harmoniques XUV est obtenu après un temps de 30 ns. Après ce temps, le rendement décroît continuellement jusqu'à pratiquement disparaître à 70 ns.

3.3.2 Comparaison entre les spectres d'harmoniques d'ordres élevées et de section efficace de photo-ionisation

Afin d'étudier la contribution du C₂ à la HHG du graphite, nous comparons la SEPI du C₂ avec le spectre d'harmoniques du graphite. En accord avec la théorie de re-diffusion quantitative (RDQ) pour les harmoniques d'ordres élevées, les spectres d'atomes ou de molécules uniques

doivent reproduire la SEPI de la particule [17]. Mathématiquement, les spectres de HHG pour un système étendu peuvent s'écrire :

$$S_h(\omega) \propto |W(\omega)|^2 \sigma^R(\omega) \quad (3.1)$$

Avec $W(\omega)$ le paquet d'onde macroscopique (POM), et $\sigma^R(\omega)$ la section efficace de photo-recombinaison qui est l'inverse conjuguée de la SEPI. Le POM $W(\omega)$ dépend du système et diffère du paquet d'onde de l'atome unique seulement par la condition d'accord de phase qu'il contient. Pour la génération d'harmoniques dans des milieux minces (comme le cas présent où le panache mesure 100 μm à 200 μm d'épaisseur), la tolérance en désaccord de phase est plus large et réduit l'influence de cet accord sur le paquet d'onde. Dans ce cas le spectre d'harmonique doit suivre fidèlement la SEPI du milieu, les deux spectres sont visibles **Fig 3.12**. Nous pouvons voir que la SEPI du carbone diatomique est plus grande que celle du carbone neutre. En comparant avec le spectre de HHG générée par le laser à 0,8 μm (courbe rouge) nous trouvons une dépendance en longueur d'onde de la SEPI du C_2 en meilleur accord avec le spectre d'harmonique que ne l'est celle du carbone monoatomique. Toutefois, le seuil d'harmoniques du panache de graphite sous excitation à 0,8 μm est limité aux alentours de 30 eV, pour comparer à la SEPI à plus hautes énergies nous générerons des harmoniques d'ordres élevées par un laser à 1,47 μm . Dans ce cas également, nous trouvons un bon accord entre les harmoniques et la SEPI du C_2 (courbe noire). En plus des raies de Swan observées **Fig. 3.9**, cette observation confirme que les harmoniques sont générées par le carbone diatomique plutôt que par le carbone monoatomique.

La **Fig. 3.12** nous a montré que des harmoniques d'ordres élevées peuvent être générées jusqu'à une énergie de 32 eV par les molécules carbonées soumise à un laser à 0,8 μm . Le potentiel d'ionisation du C_2 est 11,4 eV et l'intensité à saturation est estimée à $\sim 3.64 \times 10^{14} \text{ Wcm}^{-2}$. À partir de ces valeurs, nous tirons des spectres de la **Fig. 3.12** que les harmoniques sont générées à partir de molécules de carbone diatomiques neutres.

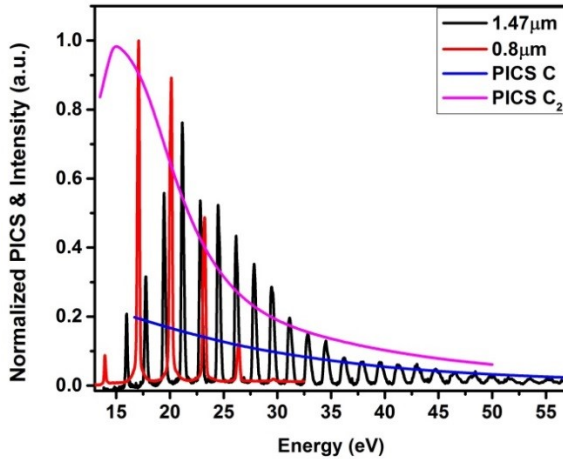


Figure 3.12: Spectres d'harmoniques d'ordres élevés générés par des lasers à 0.8 μm et 1.47 μm , et spectres de section efficace de photo-ionisation pour le carbon mono- et diatomique C et C₂.

3.3.3 Wavelength Scaling d'ordre élevé Harmonics

Les harmoniques d'ordres élevés obtenu par ablation laser du graphite contiennent plusieurs μJ d'énergies [18] lorsqu'obtenus à partir d'un laser à 0,8 μm . Toutefois, comme mentionné précédemment, le seuil apparaît à basse énergie ~ 32 eV. Nous tirons du modèle à trois étapes [1] que le seuil de HHG peut être étendu en augmentant la longueur d'onde du laser, telle est l'approche qui suit. La **Fig. 3.13** montre les spectres d'harmoniques d'ordres élevés générés par des molécules carbonées à trois longueurs d'ondes laser différentes : 0,8 μm , 1,47 μm et 1,71 μm . Pour comparer précisément l'intensité des harmoniques l'intensité du laser est maintenue constante pour ces trois longueurs d'ondes à $\sim 1.4 \times 10^{14} \text{ Wcm}^{-2}$. La **Fig. 3.13(a)** montre le spectre généré à 0,8 μm avec un seuil à ~ 32 eV. Ce seuil d'harmonique peut être amené à ~ 60 eV en augmentant la longueur d'onde à 1,47 μm , voir **Fig. 3.13(b)**. Et le seuil maximal est observé à 1,71 μm lorsqu'il atteint ~ 70 eV (**Fig. 3.13(c)**).

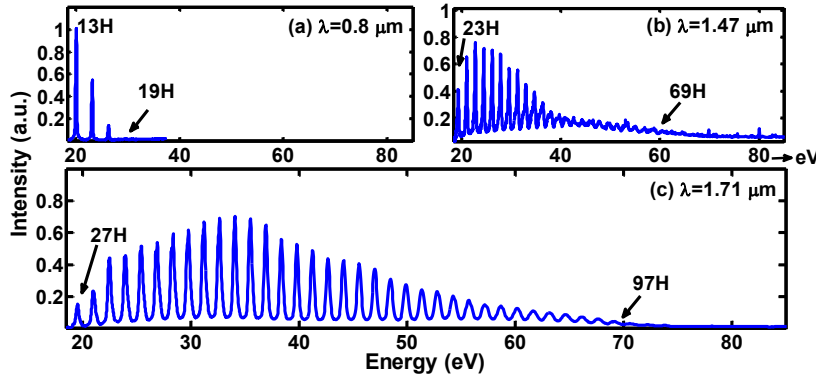


Figure 3.13: Spectres d'harmoniques d'ordres élevées générés à partir de molécules carbonées par des lasers à : (a) $0.8\text{ }\mu\text{m}$, (b) $1.47\text{ }\mu\text{m}$ et (c) $1.71\text{ }\mu\text{m}$, d'intensité $\sim 1.4 \times 10^{14}\text{ Wcm}^{-2}$.

À partir de la **Fig. 3.13**, nous remarquons également que les intensités des harmoniques demeurent comparables malgré les ajustements effectués sur le laser. A $0.8\text{ }\mu\text{m}$ notre groupe à auparavant démontré que des harmoniques d'ordres élevées à plusieurs μJ avec des rendements de 2×10^{-4} pour la 13eme和谐ique sont générés depuis le panache de graphite [18]. Les rapports d'intensité des pics à $0.8\text{ }\mu\text{m}$, $1.47\text{ }\mu\text{m}$ et $1.71\text{ }\mu\text{m}$ sont $1 : 0.76 : 0.70$. Cela indique une réduction de 30% du pic d'intensité lorsque la longueur d'onde du laser est changée de $0.8\text{ }\mu\text{m}$ à $1.71\text{ }\mu\text{m}$, avec une intensité du MP de $\sim 1.4 \times 10^{14}\text{ Wcm}^{-2}$ (donc proche de l'intensité de saturation $\sim 3.6 \times 10^{14}\text{ Wcm}^{-2}$). De ces résultats nous estimons qu'une efficacité de conversion $> 10^{-4}$ est obtenue pour les harmoniques du carbone de 25 eV à 40 eV.

3.3.4 Décalage vers le rouge ajustable

Nous avons observé des harmoniques d'ordres élevées des molécules de carbones diatomiques contiennent un décalage vers le rouge prononcé. Ce décalage est de nature continue et augmente linéairement avec l'intensité de l'impulsion laser. Dans les milieux moléculaires, le décalage peut être la conséquence de trois causes : (i) la propagation du laser [19], (ii) une pré-excitation du milieu dans la queue de l'impulsion laser [20], et (iii) la dissociation moléculaire [21]. La cause due à la propagation du laser fut premièrement proposée par Kim et collaborateurs, qui montrèrent qu'un laser se propageant dans un milieu de haute densité ($\sim 10^{18}\text{ cm}^{-3}$; épaisseur $\sim 3\text{ mm}$) subissait un tel décalage et voyait sa forme changer [22]. Cet effet n'est pas certain dans nos mesures de HHG puisque le panache de plasma est à faible densité ($\sim 10^{17}\text{ cm}^{-3}$).

cm^{-3}) et de faibles dimensions ($\sim 200 \mu\text{m}$). Plus tard, Ganeev [23] a montré qu'en HHG la forme due l'impulsion laser était conservée après passage dans le milieu.

Par conséquent, dans le cas du carbone diatomique nous explorons l'implication des états résonants et de la dissociation moléculaire comme cause de ce décalage vers le rouge.

3.3.4 (a) Rôle des états résonants

En 2011, Bian et collaborateurs [20] prédirent un décalage vers le rouge des harmoniques d'ordres élevées issues de molécules polaires. Il étudia le cas de molécules de HeH^{2+} pour calculer des spectres en résolvant l'équation de Schrödinger dépendante du temps (TDSE pour Time-Dependent Schrödinger Equation). Il montra dans ces spectres calculés que lorsque des états résonants à longs temps de vie sont impliqués en HHG un décalage vers le rouge a lieu.

Comme les états électroniques des atomes et molécules sont discrets, une manière de tester ce modèle est d'utiliser un laser ajustable en longueur d'onde pour voir si les états résonants contribuent à la HHG. Les spectres mesurés pour le C_2 à différentes longueurs d'ondes laser et pour différentes intensités sont donnés **Fig. 3.14**.

Nous y voyons que les harmoniques générées par des impulsions ($\sim 10^{14} \text{ Wcm}^{-2}$) allant de $0,8 \mu\text{m}$ à $1,84 \mu\text{m}$ présentent un fort décalage vers le rouge (**Fig. 3.14 (b-h)**). Ce décalage apparaît comme une fonction linéaire de l'intensité du laser et croît rapidement lorsque cette dernière passe du seuil de génération ($\sim 0.8 \times 10^{14} \text{ Wcm}^{-2}$) à l'intensité de saturation ($\sim 4.56 \times 10^{14} \text{ Wcm}^{-2}$) pour différentes longueurs d'onde d'excitation. À partir des spectres à chaque longueur d'onde laser, nous constatons que la valeur du décalage est indépendante de l'ordre de l'harmonique. Par exemple, pour les harmoniques générées par $0,8 \mu\text{m}$ (**Fig. 3.14 (b)**), un décalage de 0.46 eV est mesuré pour les harmoniques à $\sim 17 \text{ eV}$ et $\sim 20 \text{ eV}$, quand le l'intensité du laser est augmentée de $8.4 \times 10^{13} \text{ Wcm}^{-2}$ à $2.3 \times 10^{14} \text{ Wcm}^{-2}$. De manière similaire, aux autres longueurs d'ondes d'excitation **Fig. 3.14 (c-h)**, un décalage de 0.2 eV à 0.3 eV est observable lorsque le laser passe de $1.4 \mu\text{m}$ à $1.84 \mu\text{m}$. D'autre part, pour un laser à 400 nm , aucun décalage n'est observé sur les harmoniques, à contrario, lorsque le laser est à très forte intensité ($\sim 3.0 \times 10^{14} \text{ Wcm}^{-2}$), un décalage vers le bleu est mesuré, voir **Fig. 3.14(a)**.

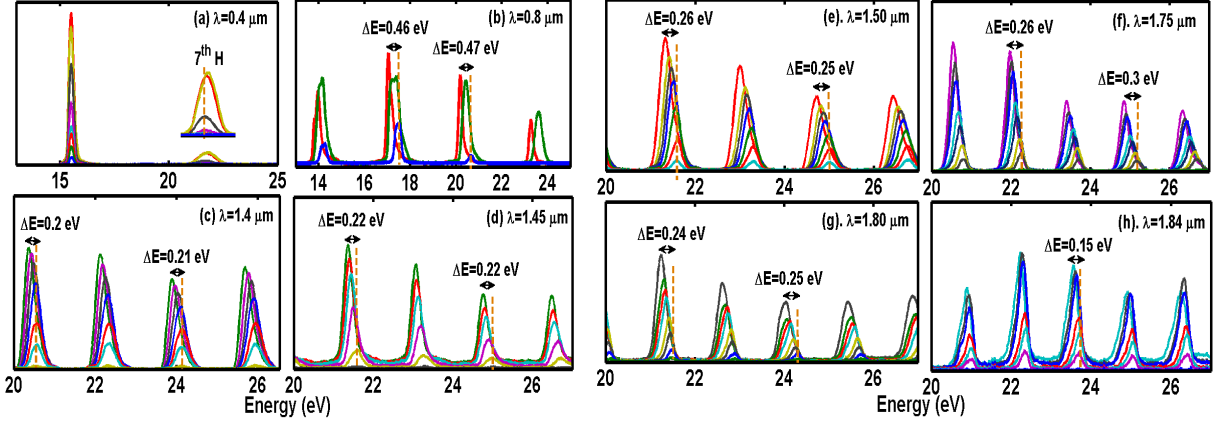


Figure 3.14: Spectres d'harmoniques d'ordres élevées générés à partir de C_2 sous différentes longueurs d'ondes laser : (a) $0.4 \mu\text{m}$, et d'intensité comprises de $7.5 \times 10^{13} \text{ Wcm}^{-2}$ à $3.0 \times 10^{14} \text{ Wcm}^{-2}$, (b) $0.8 \mu\text{m}$, de $8.4 \times 10^{13} \text{ Wcm}^{-2}$ à $2.3 \times 10^{14} \text{ Wcm}^{-2}$, (c) $1.4 \mu\text{m}$, de $1.1 \times 10^{14} \text{ Wcm}^{-2}$ à $2.3 \times 10^{14} \text{ Wcm}^{-2}$, (d) $1.45 \mu\text{m}$, de $2.19 \times 10^{14} \text{ Wcm}^{-2}$ à $4.56 \times 10^{14} \text{ Wcm}^{-2}$, (e) $1.5 \mu\text{m}$, de $1.59 \times 10^{14} \text{ Wcm}^{-2}$ à $3.27 \times 10^{14} \text{ Wcm}^{-2}$, (f) $1.75 \mu\text{m}$, de $1.49 \times 10^{14} \text{ Wcm}^{-2}$ à $3.35 \times 10^{14} \text{ Wcm}^{-2}$, (g) $1.8 \mu\text{m}$, de $1.29 \times 10^{14} \text{ Wcm}^{-2}$ à $2.28 \times 10^{14} \text{ Wcm}^{-2}$ et (h) $1.84 \mu\text{m}$, de $1.3 \times 10^{14} \text{ Wcm}^{-2}$ à $2.37 \times 10^{14} \text{ Wcm}^{-2}$.

A partir de ces observations, nous pouvons affirmer que les modes résonants ne sont pas impliqués dans ce décalage vers le rouge. Puisque ce dernier est observable pour toutes les longueurs d'ondes d'excitation utilisées en dehors de $0.4 \mu\text{m}$. Les harmoniques générées à $0.4 \mu\text{m}$ présentent un décalage vers le bleu qui peut être dû au processus normal de HHG sur la face ascendante de l'impulsion laser.

3.3.4 (b) Décalage vers le rouge dû à la dissociation moléculaire

La seconde source possible du décalage vers le rouge des harmoniques d'ordres élevées est la dissociation moléculaire. Récemment Bian et collaborateurs [21] prédirent que si les harmoniques sont générées sur la face descendante de l'impulsion laser elles doivent subir un fort décalage vers le rouge. Il utilisa pour cela une approximation non-Born-Oppenheimer pour modéliser les spectres d'harmoniques du H^{2+} et D^{2+} en expliquant le décalage vers le rouge. Selon ce modèle, lorsque l'impulsion laser interagit avec la molécule, un électron est ionisé depuis l'état fondamental. Ensuite la dissociation moléculaire commence lors de la phase ascendante de l'impulsion laser, à partir d'une certaine distance interatomique la SEPI de la molécule croît alors rapidement. L'électron ionisé est alors accéléré dans le continuum. Comme la dissociation moléculaire est un processus relativement long (quelques dizaines de

femtosecondes à quelques picosecondes), les harmoniques à fort rendement sont générées sur la face descendante de l'impulsion laser. Cette assertion sera testée ultérieurement en étudiant les harmoniques générées par des impulsions plus courtes que la période de dissociation des molécules de C₂, soit ~20 fs.

Sources

- [1] P. Corkum, Phys. Rev. Lett. **71**, 1994 (1993).
- [2] C. Winterfeldt, C. Spielmann, and G. Gerber, Rev. Mod. Phys. **80**, 117 (2008).
- [3] R. A. Ganeev, M. Suzuki, M. Baba, H. Kuroda, and T. Ozaki, Opt. Lett. **31**, 1699 (2006).
- [4] A. D. Shiner, B. E. Schmidt, C. Trallero-Herrero, H. J. Wörner, S. Patchkovskii, P. B. Corkum, J.-C. Kieffer, F. Légaré, and D. M. Villeneuve, Nat. Phys. **7**, 464 (2011).
- [5] X.-B. Bian and A. D. Bandrauk, Phys. Rev. A **83**, 041403 (2011).
- [6] M. Gaarde and K. Schafer, Phys. Rev. A **64**, 013820 (2001).
- [7] T. Ozaki, R. A. Ganeev, M. Suzuki, and H. Kuroda, High-order Harmonic Generation from Low-Density Plasma, in (In Tech, 2010).
- [8] M. Suzuki, M. Baba, R. A. Ganeev, H. Kuroda, and T. Ozaki, Opt. Lett. **31**, 3306 (2006).
- [9] V. Strelkov, Phys. Rev. Lett. **104**, 123901 (2010).
- [10] R. A. Ganeev, L. B. Elouga Bom, J. C. Kieffer, M. Suzuki, H. Kuroda, and T. Ozaki, Phys. Rev. A **76**, 023831 (2007).
- [11] A. D. Shiner, B. E. Schmidt, C. Trallero-Herrero, H. J. Wörner, S. Patchkovskii, P. B. Corkum, J. C. Kieffer, F. Légaré, and D. M. Villeneuve, Nat. Phys. **7**, 464 (2011).
- [12] J. Costello, E. Kennedy, B. Sonntag, and C. Clark, Phys. Rev. A **43**, 1441 (1991).
- [13] K. F. Al-Shboul, S. S. Harilal, and A. Hassanein, J. Appl. Phys. **113**, 163305 (2013).
- [14] Y. Yamagata, A. Sharma, J. Narayan, R. M. Mayo, J. W. Newman, and K. Ebihara, J. Appl. Phys. **88**, 6861 (2000).
- [15] Y. Yamagata, A. Sharma, J. Narayan, R. M. Mayo, J. W. Newman, and K. Ebihara, J. Appl. Phys. **86**, 4154 (1999).
- [16] R. A. Ganeev, L. B. Elouga Bom, and T. Ozaki, Phys. Plasmas **18**, 083101 (2011).
- [17] A. T. Le, R. R. Lucchese, S. Tonzani, T. Morishita, and C. D. Lin, Phys. Rev. A - At. Mol. Opt. Phys. **80**, 013401 (2009).
- [18] L. B. Elouga Bom, Y. Pertot, V. R. Bhardwaj, and T. Ozaki, Opt. Express **19**, 3077 (2011).
- [19] K. Kim, I. Alexeev, T. Antonsen, A. Gupta, V. Kumarappan, and H. Milchberg, Phys. Rev. A **71**, 011201 (2005).
- [20] X.-B. Bian and A. D. Bandrauk, Phys. Rev. A **83**, 041403 (2011).
- [21] X.-B. Bian and A. D. Bandrauk, Phys. Rev. Lett. **113**, 193901 (2014).

- [22] E. Constant, D. Garzella, P. Breger, E. Mével, C. Dorrer, C. Le Blanc, F. Salin, and P. Agostini, Phys. Rev. Lett. **82**, 1668 (1999).
- [23] R. A. Ganeev, M. Baba, M. Suzuki, and H. Kuroda, J. Appl. Phys. **99**, 103303 (2006).